ABSTRACT

Title of Document: A NEW SCALE-UP APPROACH THROUGH THE EVALUATION OF STRESS HISTORY WITHIN A TWIN-SCREW EXTRUDER

Graeme Masuhiro Fukuda, Masters of Science, 2014

Directed By: Associate Professor, Dr. David I. Bigio, Department of Mechanical Engineering

The development of any new product manufactured by extrusion requires initial testing at the laboratory level. Once the behaviors of the product and process are understood, the operation is scaled-up to an industrial grade procedure. Scale-up/down is used in a wide variety of markets such as food processing, food packaging, tubing, and pharmaceutical industries. Product quality is critical to the success of all these applications, but is often made difficult when compounding with additives, fillers, pigments, plasticizers, and other supplemental ingredients. Product quality is achieved when the constituents are well mixed. Stress is a critical parameter in accomplishing good mixing. Through the use of polymeric stress beads, a methodology has been developed to measure residence stress distributions in real time. The methodology has enabled the analysis of both model and industrial grade extruders. Evaluation of both processes has led to the creation of a new scale-up approach for dispersive mixing. The new scale-up rule based on percent drag flow

was shown to be a more accurate dispersive mixing scale-up approach for a range of operating conditions compared to the current industry standard.

A NEW SCALE-UP APPROACH THROUGH THE EVALUATION OF STRESS HISTORY WITHIN A TWIN-SCREW EXTRUDER

By

Graeme Masuhiro Fukuda

Thesis submitted to the Faculty of the Graduate School of the
University of Maryland, College Park, in partial fulfillment
of the requirements for the degree of
Masters of Science
2014

Advisory Committee:
Associate Professor David I. Bigio, Chair/Advisor
Professor Hugh A. Bruck
Associate Professor Linda C. Schmidt

Dedication

My thesis is dedicated to my grandfather, Kazuo Fukuda. Who has always inspired me to strive academically and work hard.

Acknowledgements

Dr. David I. Bigio, your leadership and mentoring was truly important in the completion of this work. I will always remember our conversations not only about the research but also on my own personal development.

Additionally, I would like to thank Dr. Linda Schmidt and Dr. Hugh Bruck for serving on my thesis committee.

There were a lot of results that were included in this study, which required a number of undergraduate researchers. I want to first thank Harry Brown, Roba Adnew, Jesse Kim, Nate Caspar, and Betel Sime, who were all there when I first began my graduate career. Following them, I would like to thank Alexander Moses, Daniel Chavez, Derrick Chiu, Ben Dryer, Jake Webb and Kyle Montemayor. To all of you, I could not have completed this work without your time and effort.

There were also a lot of graduates who had a big effect on me throughout this work. Bill Pappas, thank you for being a great mentor and beginning the residence stress distribution work. Anne Lederer, it was a pleasure working side by side with you. Lastly, Jason Nixon, your help with the MATLAB code was enormous, and your insight was always appreciated.

I would also like to thank my research collaborators at DuPont and Coperion, Dr. Paul Andersen and Mr. Mark Wetzel, who were excellent research leaders, and taught me an invaluable amount about the industry. Their help in the direction of this work, made the conclusions possible.

The operators at DuPont and Coperion made the work easy and enjoyable. Therefore, I want to give big thanks to Mr. Ray Delmer Pettitt Jr. at DuPont and Mr.

Craig Anthony at Coperion. I also want to thank the employees and interns at Coperion, especially Carly Occhifinto for helping out with all my questions and demands.

Finally, I owe a great deal of thanks to my friends and family for all their support throughout my graduate career at the University of Maryland. Thanks Mom and Dad.

Table of Contents

List of Tables

List of Figures

Chapter 1 Introduction

1.1 Polymer Extrusion

Polymer extrusion is a versatile processing technique that is one of the most popular ways of compounding plastics in the world today [1]. Extrusion can be either continuous or discontinuous, cold or hot, ram or screw, with the goal of creating a final product that has a fixed, cross-sectional-profile. The following thesis will focus on continuous hot melt extrusion through the use of two adjacent co-rotating, plasticating screws. Raw thermoplastic materials in the form of pellets, granules, and powders are first fed into a hopper [2]. The material is dispensed from the hopper into the feed port. The material travels through the barrels of the extruder that externally heat the material and encase either a single screw or multiple screws. The screws are purposed to pump, melt, and mix the fed material(s). The degree to which these processes are accomplished is dependent on the type of machine, its screw configuration, and the operating conditions. After the material is transformed into a melt flow it is conveyed into a section that mixes the material. Once the mixing operation is complete the material is pumped to the die, where the material exits the extruder with a certain form and shape dependent on the orifice (die) geometry. Exited extrudate is then subjected to post-processing techniques to form a variety of products, such as pellets, rods, tubes, films, sheets, or a custom shape.

1.1.1 Single Screw Extrusion

The earliest extrusion device was invented in the 19th century and used a single screw to process material. Single screw extrusion is defined by the use of a single plasticating screw within the barrels of the machine. Early applications of this technology included the pottery, rubber, and food processing industries [3]. The rotating screw and stationary barrel walls generate frictional forces that drive the material forward as well as heat the material [4]. The motion that the screw creates is known as drag-induced flow.

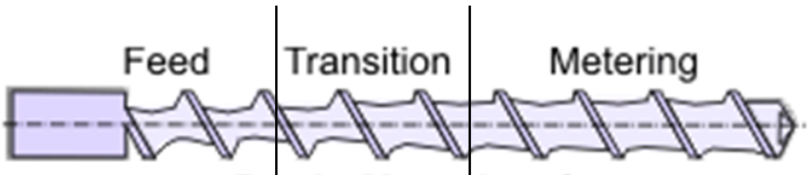

Figure 1.1: Single Screw Extruder Zones [4]

The standard configuration of the single screw extruder (SSE) decomposes the rigid body screw into three zones, which can be seen above in Figure 1.1. The zones are categorized based on the depth of the screw flights (lobes), for a given length of the screw. The initial section, the feed zone, has the deepest flights to receive the solid polymeric material. Next, the transitional zone or compression zone, in this section the depth gradually shallows as the squeezing of heated polymer produces a molten form. The last zone, the metering zone, exhibits the shallowest channel depth for greatest compression. The compression created by the metering and transition zone is critical to the efficiency of the SSE. When the molten material moves through the transitional and metering zones, compression forces, caused by the shallower depth, along with the operating conditions dictate the final properties of the extrudate when

it exits the die. However, research contained in this thesis utilizes twin-screw extruder (TSE) technology, therefore, the remainder of Chapter 1 will be focused on the parameters concerning twin-screw extrusion.

1.1.2 Twin-Screw Extrusion

Although single screw extrusion is an extremely common processing technique, twin-screw extrusion has been increasing in popularity due to its mixing capabilities, design flexibility and improved process control. One major distinction between a SSE and a TSE is the transport behavior. In a SSE, transport is strictly drag induced. In a TSE there is transport resulting from frictional properties of both the solid and viscous material. There are many types of TSEs. The two screws of a TSE can be intermeshing, non-intermeshing, or fully intermeshing. In non-intermeshing TSEs there is a gap between the two parallel screws that is at least equal to the outer diameter of the screw [5]. When the screws are intermeshing they have a separation that is less than the outer diameter of the screw. In a fully intermeshing design the two screws match up flush up against each other [5]. The next characteristic of a TSE is the rotation of the screws with respect to each other. In a co-rotating twin-screw extruder (CoTSE) the screws turn in the same angular direction. Alternatively, the screws in a counter rotating twin-screw extruder (CRTSE) spin in opposite angular directions. The differences in types can be seen below in Figure 1.2 [6].

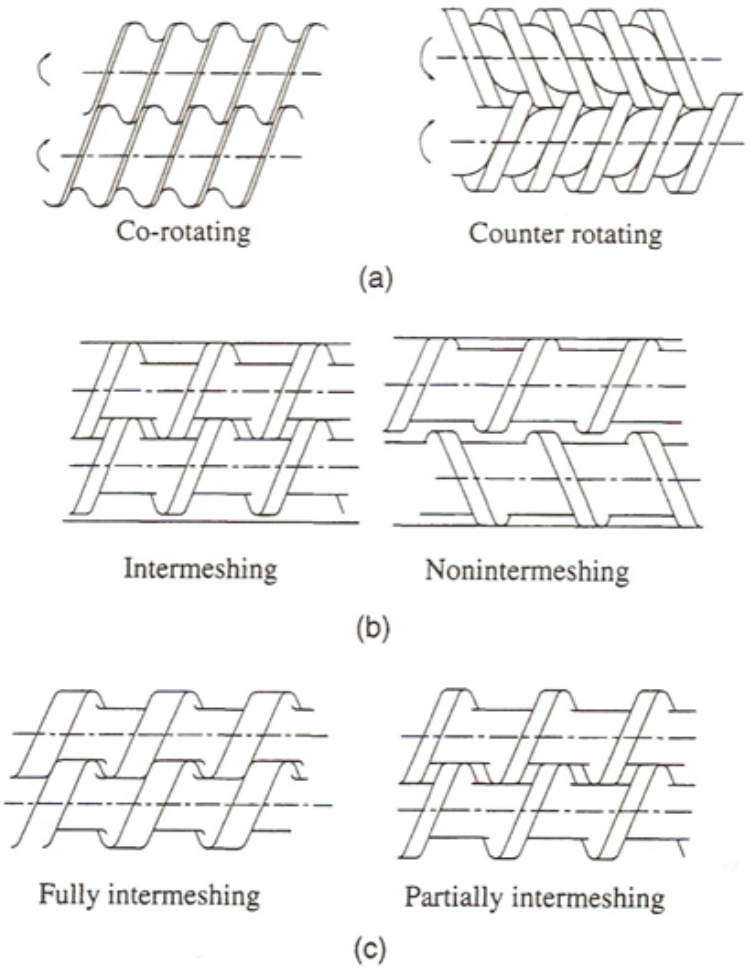

Figure 1.2: Types of TSEs [6]

In addition to the various types of TSEs there is a high degree of design flexibility regarding the screw configuration. The screws of a TSE, unlike the screw of the SSE, are composed of a multitude of building block elements of different shapes and sizes. The modular design of the screws, allow manufacturers to create an infinite amount of screw geometries.

1.1.2.1 Screw Elements

TSE modularity is made available by the various types of screw elements that can be put on the screw shaft. The following section describes the two most commonly

used element types: conveying elements and kneading block elements. Although there are others types of elements, this thesis only tested configurations based on these elements. For any screw element, the shape will vary according to the amount of flights. The flight of a screw is determined by its helical angle. Figure 1.3 below shows an axial view of the three screw flight classifications: single-flighted, double-flighted, and triple-flighted. The diagram below also establishes the nomenclature for each part of the screw's cross sectional profile.

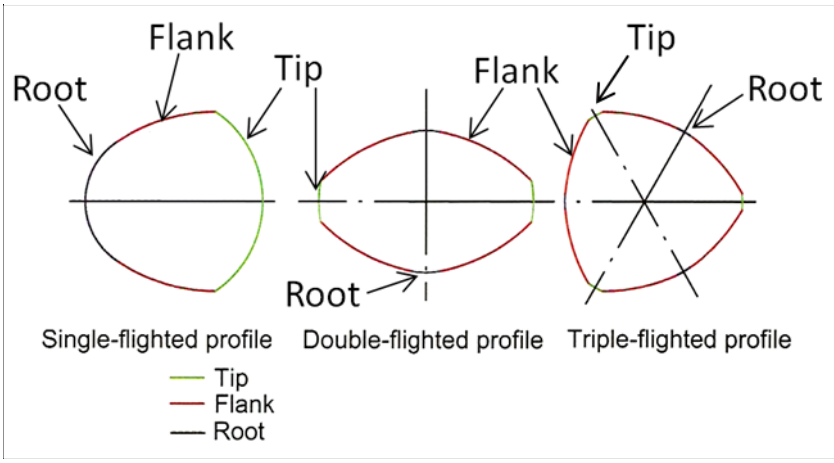

Figure 1.3: Various Screw Profiles [3]

In Figure 1.3, the single-flighted or -lobed screw element has one tip, one root, and one flank area. The multi-flighted elements then follow a rule of symmetry. The double-flighted element has two of each area. The triple-flighted element has three of each area. Further inspection of Figure 1.3 shows that if a screw has n threads, then it can be evenly broken up into 2n symmetrical parts. In addition, the arc of the tip or the arc along one tip to the next, for multi-lobed screws, has a diameter equal to the outer diameter of the screw. Thus, the number of lobes produces different processing characteristics. Single-lobed machines are effective at conveying solids and

improving feed intake. Single-lobed extruders are chosen for processes that have limited ranges of throughput or poor flow properties; for example, low bulk density powders [7]. Bi-lobal extruders have deeper channels that allow for greater free volume. However, bi-lobal extruders produce a lower shear rate in comparison to tri-lobal machines. When materials are shear or temperature sensitive or high shear forces are not required bi-lobal extruders are ideal. Tri-lobal screws have very shallow channels and subsequently small free volumes, which induce high shear rates. The high shear rates make tri-lobal machines ideal for high intensive mixing processes. For instance, processes that require breaking up additives with an inherent cohesive strength.

1.1.2.1.1 Conveying Elements

The most commonly used element is the conveying element. These elements pump material from zone to zone and out of the extruder. Conveying elements or screw bushings are necessary pieces in a positive displacement pump machine, such as an extruder. The conveying power of these elements is determined by number of flights per unit length and crest width. Wider crest widths generate a greater twist restraint. Twist restraint refers to the restriction of the material to rotate in the screw channel [8]. The greater the twist constraint the better the conveyance will be in the axial direction. Thus, wider-pitched conveying elements pump more material than narrow-pitched conveying elements. The wider pitch also means that, for the same throughput, the element will have a lower degree of fill compared to a narrow-pitched conveying element. Therefore, the pitch becomes another way for operators to alter the degree of fill besides changing the throughput. The wider pitch and lower fill also

reduces residence time [7]. Conveying elements will be grouped as either narrow-, wide-, or square-pitched throughout the thesis. The definition of a square-pitched conveying element is an element which has a pitch equal or closest to the outer screw diameter. The square-pitched element falls in between the pitches of the wide- and narrow-pitched conveying elements.

Conveying elements also have very little mixing capability compared to kneading block type elements. The design of a standard conveying element, seen below in Figure 1.4, is defined by an external helical ridge wrapped around a cylindrical shaft.

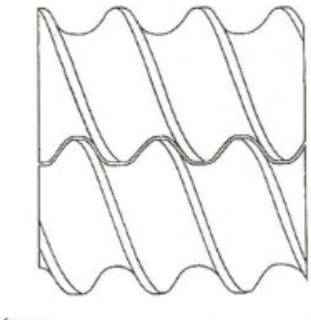

Figure 1.4: Conveying Element Diagram [3]

Figure 1.5 below shows additional geometrical characteristics of the conveying element that categorize the conveying elements physical behavior and pumping ability [7].

Element Type	Mixing	Shearing	Conveying
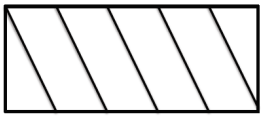 Right Handed Large Pitch	LOW	LOW	FAST
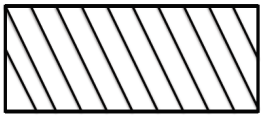 Right Handed Small Pitch	LOW	LOW	SLOW
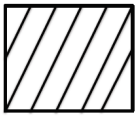 Left Handed	LOW (SEAL)	MEDIUM	BACK PRESSURE COMPONENT

Figure 1.5: Physical Behavior of Different Types of Conveying Elements [7]

Conveying elements are also distinguished by flight direction, also known as their handedness. Convention dictates that right-handed (forward) conveying elements push material downstream, towards the die zone exit. Left-handed (reverse) conveying elements do the opposite, moving the material upstream towards the feed zone. This produces fluid motion concurrent to the flow of material, which generates backpressure. Typical screw designs use reverse elements to fully fill sections of the extruder. The flow barriers created by reverse elements force the right-handed conveying elements to overcome moderate pressure resistance, which creates a localized pressure drop. In Figure 1.6, a pressure drop can be seen when transitioning from forward conveying elements to a reverse element (top) and from a kneading block element to a reverse element (bottom) [7]. Note that the kneading block elements are pressurized for a longer distance because their conveying ability is not as efficient as the conveying elements.

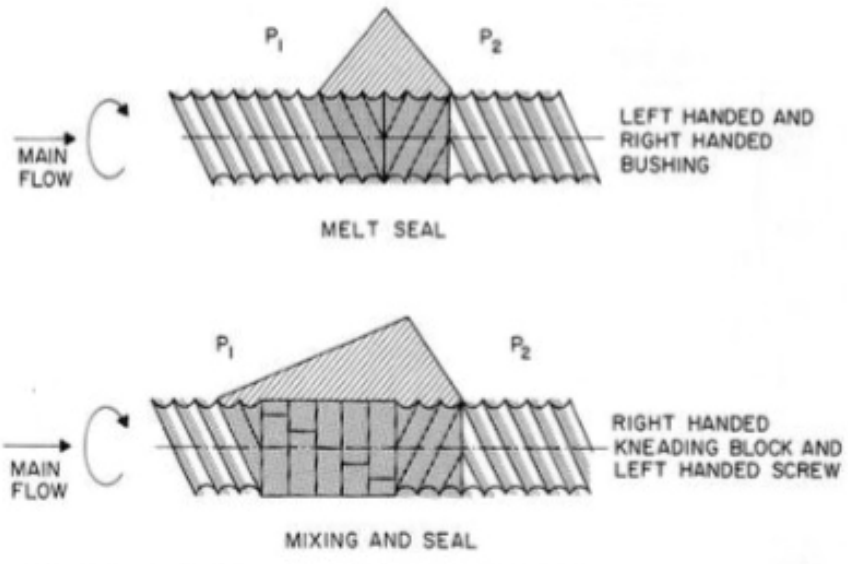

Figure 1.6: Reverse Element Pressure Drop [7]

Strong flow barriers or melt seals can provide a buffer between venting operations common in devolatilization [6]. Another standard application of reverse elements is to place them in front of kneading block elements to enhance mixing. For all applications discussed reverse elements always increase residence time and shear input. Industry nomenclature for conveying elements states that the elements are named by "pitch/axial length followed by 'RH' for right-handed and 'LH' for left-handed", this nomenclature will be used in the following thesis.

1.1.2.1.2 Kneading Block Elements

In both the CoTSEs and CRTEs, a portion of the screw is designed to be a mixing zone. The most common type of element that specializes in mixing is the kneading block element. Kneading block elements can be categorized in a similar fashion to conveying elements by the number of lobes, length, and pitch. However, because kneading block elements are constructed as stacked discs with a specified stagger angle, there is an additional geometrical aspect, the disc width. Typical kneading

block nomenclature is based on the disc or paddle width, which can be wide (broad), medium, or narrow (slender). Kneading blocks will also be named as "KB followed by stagger angle/ number of discs per element /axial length"

In addition, like the conveying elements the kneading block elements can be oriented in either the forward or reverse direction. Furthermore, kneading block elements can be neutral, where the discs are oriented perpendicular to the screw shaft. Figure 1.7 below depicts the design of neutral and forward bi-lobal kneading block elements [3]. It can be seen in Figure 1.7, if one looks into the page, that there are spaces between successive discs. These spaces, allow for polymer flow to move from channel to channel, and also cause flow losses due to leakage [9].

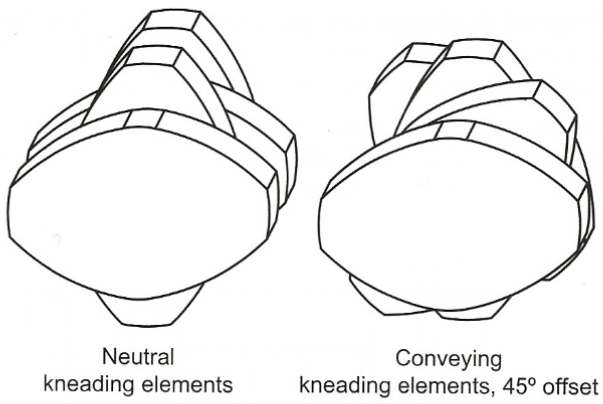

Figure 1.7: Neutral and Right-handed Kneading Block Element Diagrams [6]

Mixing performance heavily relies on the disc width. Wide kneading blocks more easily allow the material to flow over the tip and be squeezed against the barrel wall because of their wide paddles. The squeezing creates shear stress. Additionally, extensional stresses can occur between two adjacent kneading blocks. The

combination of the shear and elongational forces generate high stress regions in wide kneading block geometries.

Narrower kneading block elements have a higher quantity of paddles per unit length, in comparison to the wide kneading blocks. As the material moves through narrow kneading block elements, a small percentage of the material flows over the tip and squeezes against the barrel wall. Instead, the flow is split and diverted around the slender discs. Repeated splitting and recombining motions created by frequent narrow paddles produces a high amount of strain. Figure 1.8 below shows the fluid particle paths that characterize the wide and narrow kneading block elements [10]. The wide and narrow kneading blocks are the two extremes of the element type, but there is also an intermediary size, the medium kneading block element.

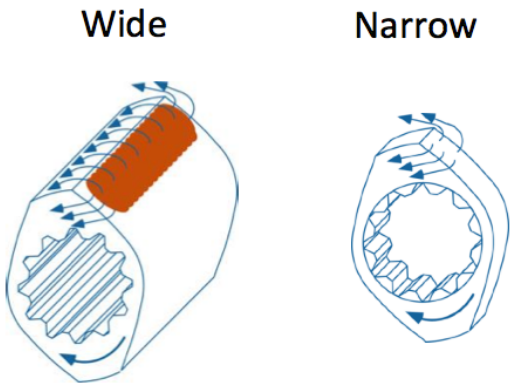

Figure 1.8: Wide and Narrow Kneading Element Flow Diagram [10]

1.1.2.2 Co-Rotating Twin-Screw Extruders

The CoTSE refers to a TSE in which the two screws are rotating in the same direction. CoTSEs are self-wiping (also termed self-cleaning) due to the motion between the parallel screw elements. As one screw element's tip passes by the

adjacent screw element's flank, the element cleans itself [3]. The self-cleaning motion can be seen below for bi-lobal screws in Figure 1.9, which shows the movement of the pools of material as it traces out a figure eight-like pattern.

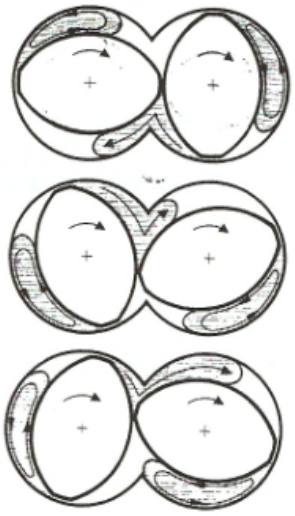

Figure 1.9: CoTSE Element Alignment and Motion [11]

The self-wiping motion allows for easier maintenance of the screw elements. As stated before, CoTSEs can be intermeshing, non-intermeshing, or fully intermeshing. They are used in many different applications such as mixing thermoplastics, devolatilization, reactive extrusion, and food processing.

Although the CoTSE's screws are completely modular, there are certain common configurations between all designs. Similar to the SSE, the CoTSE can be decomposed into zones based on purpose. Zones include the intake, plastification, mixing, melt conveying, devolatilization, and back pressure zone. Every screw geometry will contain some combination of these zones, not all geometries will contain all zones. The intake zone, as its name suggests, is the zone where the raw thermoplastic material enters the extruder. In this zone, a wider-pitched conveying

element is used to reduce torque on the extruder motor and receive solid material. As the material begins to be heated, the pitch of the conveying screws will typically decrease prior to the plastification zone. The next zone, the plastification zone, is intended to fully melt the plastic. The plastification zone includes narrow-pitched conveying elements and a combination of neutral or narrow kneading block elements, which are used to compress the material and control the melting [3]. A melt conveying zone is typically found after the plastification zone. The primary function of this zone is to pump material to the mixing zone and it is commonly comprised of square-pitched conveying elements. The melted polymer is conveyed to the mixing zone, which is a fully filled section because it is directly upstream from the backpressure zone. The mixing section is comprised of different kneading block elements, dependent on the stress or strain requirements. The mixing zone makes the CoTSE an effective compounder, and is unlike any zone found in a SSE. Figure 1.10 below shows the five main stress regions where the greatest mixing is imparted on the pool of material (lobal pool) [12].

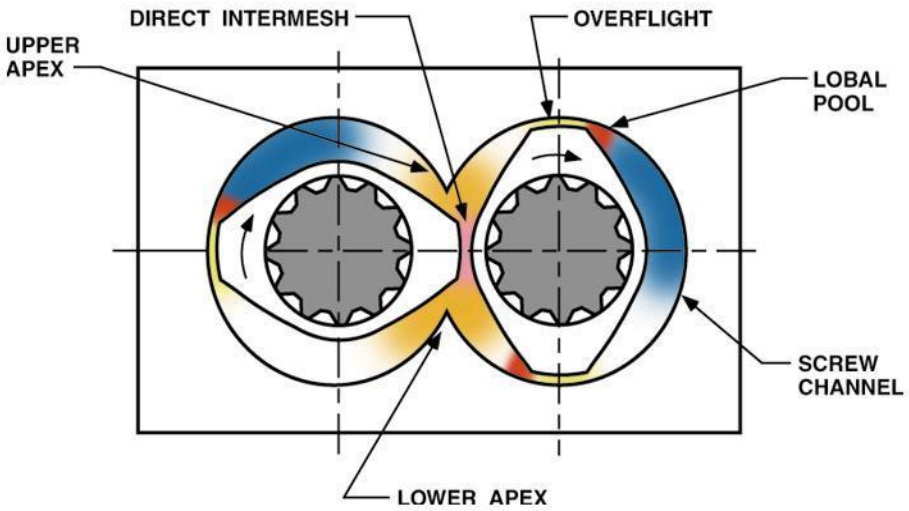

Figure 1.10: The Five Main Stress Regions [12]

The stress generated in these five regions, from both the shearing and elongational forces, helps produce a homogeneous mixture. The different types of mixing achieved in a CoTSE are discussed later in this chapter. The devolatilization zone, unused for the work presented in this thesis, serves to remove any water, residual monomers, or solvents. The devolatilization zone requires either neutral or reverse conveying elements at the beginning and end of the zone to create a complete seal. Strategically placed vents along the zone ensure efficient devolatilization. The backpressure zone is the last zone before consecutive conveying elements that pump the material through the exit die zone. The backpressure zone creates a build-up of pressure through neutral kneading blocks or reverse conveying elements, intended to fill the mixing section. However, with greater pressure build-up, a greater amount of input energy is required. An ideal design balances the backpressure required to fill the upstream elements while minimizing increases in energy input.

1.1.2.3 Counter-Rotating Twin-Screw Extruders

The CRTSE like the CoTSE is a positive displacement pump that pushes material using a drag induced flow [11][13] . However, unlike the CoTSE, the screws move in opposite directions with respect to each other creating a different flow field compared to the CoTSE, but the sections of the screw design are similar. Advantages of CRTSEs include a steady feed and high pressure stability. The CRTSE can be either non-intermeshing or intermeshing. Figure 1.11 show flow visualizations for a non-intermeshing CRTSE and an intermeshing CoTSE.

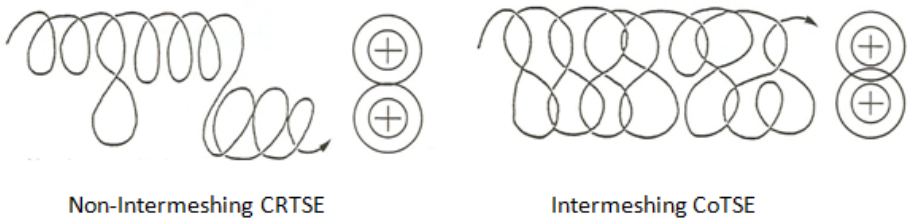

Figure 1.11: Flow Visualizations of Non-Intermeshing CRTSE and Intermeshing CoTSE [14]

Viscous flow in the intermeshing CoTSE exhibits far greater movement between the screws. However, flow in the non-intermeshing CRTSE rarely crosses between screws. Lower inter-screw movement in the CRTSE is one reason CRTSEs are not used for high intensive mixing processes. Furthermore, the high pressure constrains the allowable shear rate achievable in the CRTSE. An intermeshing CRTSE, where one screw flight aligns with the adjacent screw's channel, is depicted below in Figure 1.12. The flow of an intermeshing CRTSE is often characterized as a C-shaped chamber, which can be seen in Figure 1.12 for one screw.

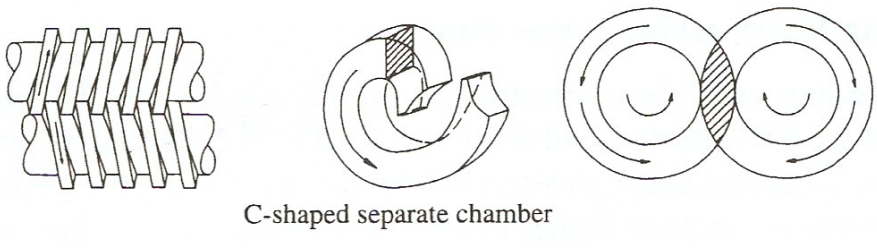

Figure 1.12: Alignment and Flow of an Intermeshing CRTSE [6]

Studies have shown the CoTSE to be a more effective mixer than the intermeshing CRTSE due to the figure eight-like flow pattern and higher axial velocity [15]. The most common intermeshing CRTSE application is profile extrusion, while non-intermeshing CRTSEs are used for devolatilization and reactive extrusion [4].

1.2 Mixing

To understand mixing, a mixture must be defined. A mixture is a state created by a network of two or more species. These species must remain distinct regardless of the degree of intermixing. To achieve a homogeneous mixture, a mixture with minimized non-uniformity, the components must be well blended. The operation of mixing can be carried out in three ways: (1) molecular diffusion, (2) eddy motion, and (3) convection. Both molecular diffusion and eddy motion are absent in extrusion due to the absence of chemical potential and turbulent motion, respectively. Thus, highly viscous polymers are mixed primarily by convection or bulk flow. Convective mixing is achieved by an increase in interfacial area shared between the major and minor phases of the emulsion, or the increase in the minor component's presence throughout the major component without area increase [6]. This kind of convective or laminar mixing is often also known as distributive mixing.

1.2.1 Distributive Mixing

Distributive mixing can be described as the folding and recombining motion experienced by the materials through the machine. The goal of distributive mixing is to have the minor phase evenly spread throughout the major phase. The efficiency of distributive mixing can be evaluated through local deformations or strain of a specified particle in the polymer matrix [16]. The strain can be imposed through either a stretching or shearing motion. The different types of stretching motions are displayed in Figure 1.13 below.

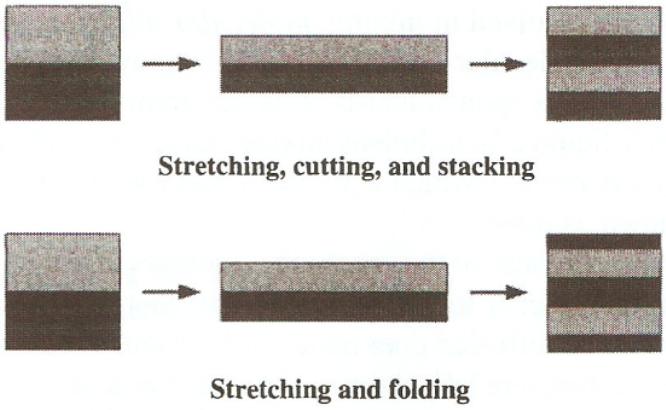

Figure 1.13: Two Types of Distributive Mixing [6]

Shearing motion shown in Figure 1.14, where a tube is filled with a dark grey fluid and the additive is the line of black spheres, also contributes to distributive mixing. The pressure drop produces shear deformation. Figure 1.14 also shows the black spheres deforming along the non-uniform velocity profile and squishing into ellipsoids, which produces an increasing in interfacial area. In all of these descriptions, mixing is a function of strain. Stress does not play a role in distributive mixing [6]. Narrow kneading blocks elements produce high degrees of strain, making them good distributive mixers.

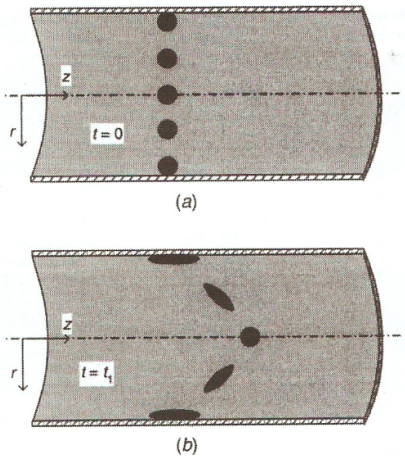

Figure 1.14: Distributive Mixing by Shear Deformation [6]

1.2.2 Dispersive Mixing

Alternatively, for compounding processes that involve additives or fillers with an inherent cohesive strength, distributive mixing is not enough. Take the example of the black spheres above in Figure 1.14. If those spheres are agglomerates with some cohesive strength, local stress histories would play the lead role in breaking them apart. The fracturing of agglomerates in a viscoelastic system is known as dispersive mixing and is a direct function of stress. The solid agglomerates in the mixture have a cohesive strength produced by Van der Waals forces. In order to achieve enhanced polymer matrix properties, the agglomerate size must be reduced. However, dispersive (or intensive) mixing is not only limited to solid-liquid mixtures. In both solid-liquid and liquid-liquid mixtures, the cohesion will depend on the Van der Waals forces and the particle size. Smaller sized agglomerates are more robust than larger ones with the same physical properties. Since wide kneading block element generate high degrees of stress, they are characterized as good dispersive mixers.

Processing multi-species of plastics and additives requires both dispersive and distributive mixing to obtain a homogeneous mixture. Figure 1.15 illustrates differences between the two mixing mechanisms and the outcome when both are realized [6].

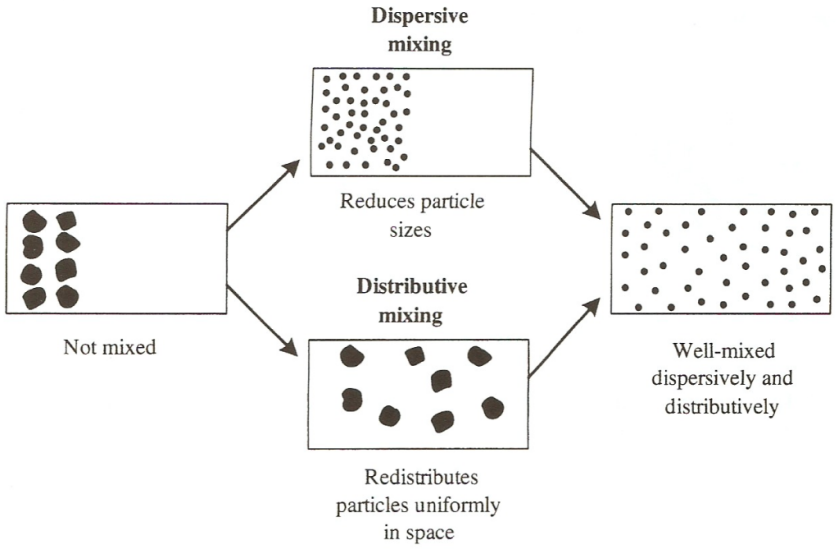

Figure 1.15: Measure of Mixing [6]

1.3 Residence Distributions in Twin-Screw Extrusion

Due to the complex flow involved in extrusion numerical analysis can be difficult. Thus, kinematic pictures are a common approach to describing the physics. In evaluating extrusion processes there are a number of different kinematic pictures that can help evaluate and predict product quality. One of the most essential kinematic pictures is the residence time distribution (RTD). In any type of continuous process, such as twin-screw extrusion, residence time is defined as a distribution, not by a discrete value. The distribution is due to the non-uniform velocity profile that exists in the screw channels. The RTD is influenced by a variety of parameters including extruder operating conditions and the screw element types. Figure 1.16 shows the effect of screw configuration and degree of fill on the shape and delay time of the RTD [3]. Delay time refers to the amount of time it takes for the RTD to begin. For in-line processes this is the time it takes for the tracer to trigger the sensing probe.

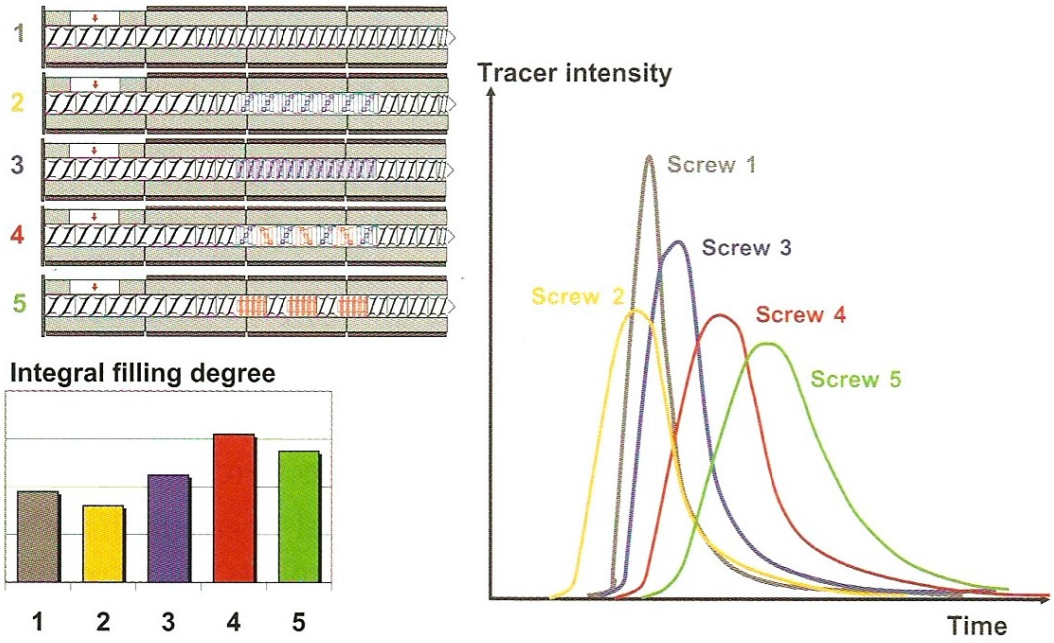

Figure 1.16: Variability in RTD [3]

The effects of the operating conditions, which include screw speed (N) and throughput (Q), have been studied extensively. Experimental results have found a constant screw speed with an increasing throughput will decrease the delay time, and the shape of the peak will be sharper. Alternatively, if the throughput is kept constant and the screw speed increases the shape of the curve changes very little but the same delay time decrease appears [17][18]. The RTD is critical to processes that utilize heat sensitive materials, as well as reactive extrusion because the time that material spends in the extruder directly correlates to material degradations and reactions.

However, there is no direct correlation between RTDs and mixing. Yet, RTDs can be transformed to represent other characteristics of an extruder. The Residence Revolution Distribution (RRD) is generated by scaling the time axis by screw speed. The RRD looks at the amount of revolutions the sample of fluid particles move through over a specified screw length. The RRD provides insight into transport

behavior. In a similar way, if the time axis is multiplied by the throughput, then a Residence Volume Distribution (RVD) is produced. The RVD space examines the measure of the particle distribution in the material in the axial direction [17][18]. Further experimental studies and effects will be discussed later in Chapter 2.

1.4 Motivation of Thesis

The field of advanced polymers is growing in popularity. To achieve enhanced material properties, polymers are compounded with solid additives such as carbon microfibers, nanotubes, glass fibers, and much more. To maximize the degree to which the additives improve the polymer matrix, dispersive mixing is necessary.

Additionally, success on a production grade extrusion line requires careful study of the process's behavior at the laboratory level. Laboratory testing allows for a minimized use of potentially expensive additives. Therefore, an accurate scale-up approach focused on dispersive mixing is critical.

A methodology that measures the mechanisms of dispersive mixing within a fully-intermeshing CoTSE has been developed. Through a Design of Experiment (DOE) approach using stress sensitive beads, a residence stress distribution (RSD) was measured in real-time and compared for various screw configurations on different sized extruders.

Using this RSD methodology, a newly proposed rule for dispersive mixing scale-up was compared to an industry standard scale-up approach. The new scale-up rule based on percent drag flow was shown to be the most accurate approach for dispersive mixing scale-up for a range of operating conditions. A percent drag flow scale-up approach will advance manufacturers' understanding on scale-up for stress-

sensitive mixing processes. The results of the experiments performed in this thesis have started the shift to a more dynamic and accurate scale-up approach through percent drag flow.

1.5 Outline of Thesis

In the following thesis, the procedure and results from this study are presented. Chapter 2 is an overview of the background literature related to mixing and scale-up in extrusion. Chapter 3 reviews the experimental procedure and includes the screw geometries, materials, and equipment necessary for this study. Chapter 4 contains the theoretical calculations related to the analysis of the results and the derivations of the scale-up rules. Chapter 5 presents the results from the RSD experiments, which includes the experiments involved in validating the RSD methodology and applying it to dispersive mixing scale-up. Finally, Chapter 6 summarizes the results of the study and the intellectual contributions. Chapter 6 also contains the future work that can be performed based on this study.

Chapter 2 Literature Review

In processing of plastics through extrusion it is common to introduce additives, fillers, and other modifiers to a polymer matrix. The degree of mixing achieved is critical to maximize the potential of the desired properties.

Before compounding processes are brought to an industrial production line, they are tested in a laboratory setting. A precise scale-up approach is necessary to ensure that the processes maintain consistent behavior at the production scale. The following background aims to summarize the past studies that have paved the way for the development of a real-time stress history methodology and application of this methodology as it concerns dispersive mixing scale-up.

2.1 Measure of Mixing

Past studies have shown there a many ways to characterize both distributive and dispersive mixing. In an extruder the flow is laminar, thus no measures of mixing regarding turbulence will be described in this work. In the 1950's Spencer and Wiley published one of the first studies on the mixing of very viscous fluids in laminar flow. To distinguish it from turbulent mixing they coined the term "streamline mixing". In order to study mixing one must first define "good mixing". Spencer and Wiley stated that two things must occur to achieve "homogeneity": (1) subdivision of the materials present, and (2) distribution of the subdivided materials [19]. Once these two criteria were defined mathematical derivations were performed to create quantitative meanings for them. The subdivision of materials was characterized by a minimum shear and a corresponding minimum shearing strain. These equations concluded that

for small increases in surface area a 45° orientation between the surfaces and the displacement vectors would be best, and for large increases the undeformed surface should be oriented perpendicularly [19]. The other mechanism to obtain proper subdivision was to stretch the material through tensile strains, which Spencer and Wiley found to be most effective when the undeformed surface was parallel to the tensile components of the displacement vectors [19]. The second criterion, the distributive portion, was best modeled through an idea of repetitive mixing. Repetitive mixing refers to some mixing unit operation which was performed, the mass reassembled, and then the unit operation carried out again. The cycle is repeated as necessary. Spencer and Wiley derived distributive mixing measures through repetitive mixing experiments [19]. These distributive measures were built off a concept from Brothman et al. who related interfacial area increase to better mixing [20].

The study of mixing continued to develop based on the principles defined by Spencer and Wiley. Lewis Erwin evaluated laminar mixing through three-dimensional analysis [21]. In this study, three types of flow were investigated: (1) pure shear, (2) simple shear, and (3) pure elongation. The deformation of fluid surfaces led to the conclusion that improved mixing was a function of the stretch ratio. The second finding compared the three investigated flows by their energy consumption. Erwin stated that in the process of mixing a Newtonian fluid, extensional flows were far more efficient than simple shear flows. It was also stated in earlier works that previous articles found that laminar extensional flows could even be superior to turbulent mixing for viscous polymers [21].

Another seminal mixing study was performed by Hassan Aref who introduced mixing through chaotic advection, which improved mixing by streamline hopping [22]. Additionally, Ottino et al. studied laminar mixing from a continuum mechanics perspective, which enabled greater detail of initial orientation of fluid species [23].

Erwin's work was continued by Bigio et al. in an experimental study of how screw geometries affect certain measures of mixing within a SSE. The screw configuration of constant cross section had a small mixing pin to reorient the fluid to increase the effectiveness of the shear strain. The theory behind reorientation states that surfaces tend to align themselves to the shearing plane of the unidirectional applied shear stress. The growth of interfacial area is a function of strain multiplied by the cosine of the orientation angle. Thus, if the fluid is oriented at 90° the growth goes to zero. Therefore, one of the primary goals of the mixing section was to reorient the fluid for favorable growth. Bigio's experiment implemented the use of white and black silicone injection ports and then evaluated the cured carcass samples at different positions along the screw. Figure 2.1 displays one of the carcass samples analyzed.

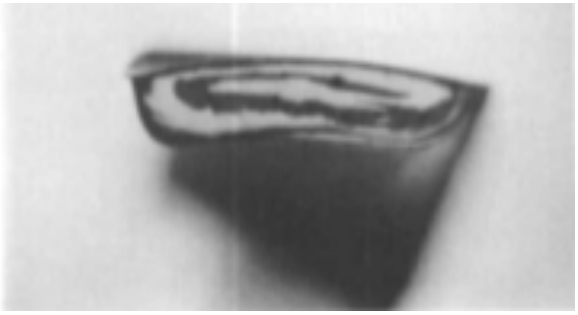

Figure 2.1: Carcass Sample of Mixing Section at Some Length [24]

The analysis was predicated on a measure of mixing described by the number of striations and its inverse relationship with striation thickness. A striation number along the vertical axis was determined for each cured sample. As the number of

striations increased the striation thickness decreased which provided insight regarding the amount of mixing. Bigio et al. found that the reorientation of the fluid by the mixing section promoted extensive mixing and even a single reorientation showed a doubling of the mixing rate. Additionally, a method was developed that examined screw geometries relating the total strain and the slope of the interfacial area line to a mixing measure [24].

P. V. Danckwerts defined another measure of mixing [25]. Danckwerts determined that two main quantities were needed in order to determine mix quality. The two quantities were the scale of segregation and the intensity of segregation. The scale of segregation measured how well the spread of clumps or certain concentrations were within a mixture. Through the use of statistical methods, Danckwerts focused on concentrations in certain sample volumes from the mixture. Then by calculation of the deviations and variances from the mean, a measure for the scale of segregation could be determined. The next quantity was the intensity of segregation. The value for intensity was given by the deviation from mean clump size. Values ranging from 0 to 1 indicated uniform concentration to a variation in concentration from point to point in the mixture, respectively. In practical applications, Danckwerts suggested a method based on evaluation of chemical reactions, especially in batch mixing processes [25].

Later studies performed by Bigio and Stry furthered the measures of mixing proposed by Danckwerts with respect to striation characteristics within a mixture [26]. The previous study was an amplitude-type approach with a mixture of either black or white species. Instead, Bigio and Stry argued the need for a frequency-based

approach to take into account diffusion and possible gray intensity. A frequency-based approach included two measures: the frequency at which the streak changed, whether white, gray, or black, and the variation of that frequency. Simple calculation of the striation widths and an extensive tabulation of that data provided the statistical information necessary to evaluate the extent of mixing. Three different types of mixers were studied in this work a static mixer, CRTSE, and CoTSE. In relation to the study in this thesis, only the CoTSE will be reviewed. Due to measurement limitations, large amounts of results were inconclusive. However, inspection of the interface distribution showed a gradual plateau effect of the variance of average striation width after a steadily increasing pattern. This result indicated that interfacial area growth slowed and that this geometry provided a lack of reorientation. In addition, the researchers concluded that there are consistently unmixed regions within the CoTSE [26].

Measures of mixing have also been extended to more specific continuous mixers. Lidor and Tadmor extended Danckwerts's concepts and used the RTD to develop strain distribution functions (SDF) to describe good mixing. Lidor and Tadmor tested different extruders defined by their channel depth, diameter, channel width, and extruder length using the SDF. They found that the mixing deteriorated when the flow was increased and that the mixing was greatly improved when the screw speed was increased for a constant flow rate [27]. Beyond characterizing different extruders, researchers have conducted tests evaluating the mixing of certain screw elements. Luo et al. used 3-D simulations of the flow field, speed field, shear rate field and pressure field. Through this model and an RTD they were able to determine the

different mixing abilities of various screw elements. The notable finding of the study, compared the kneading block element to the conveying element. The results, with regard to shear rate and shear rate distribution, showed that the kneading block element was a far better dispersive mixer and the conveying element primarily pumped material rather that mixing it [28].

Modeling of the extrusion process, although complex, has become an increasingly popular way to characterize the degree of mixing. Kalyon et al. performed multiple studies using numerical analyses and 3-D finite element methods to characterize mixing within an extruder [29][30][31][32].

2.1.1 Dispersion

The scale-up rule proposed later in this thesis applies to dispersive mixing. Therefore, a comprehensive knowledge on dispersion of solid additives is critical. Solid additives used in the plastics industry, which are colloidal in nature, tend to form aggregates that clump in larger collections known as agglomerates [16]. Thus, dispersion is vital in order to understand how those agglomerates break down. The decomposition of agglomerates occurs in stages. Parfitt developed a model that outlined the four major steps of dispersive mixing: (1) the additive is introduced to the polymer; (2) the wetting of the additive; (3) overcoming the cohesive force holding the agglomerates, and even aggregates, together; (4) stabilization of the process [33].

Many studies have then expanded the break-up of the agglomerates. Scurati et al. examined the kinetics of agglomerate erosion in simple shear flow. The analysis defined the particle bonds holding the agglomerate together, the Van der Waals

forces, and the hydrodynamic forces needed to overcome the Van der Waals forces. Bohin et al. showed that the relationship between these conflicting forces can be represented by the fragmentation number, defined as the ratio of hydrodynamic forces to cohesive forces, which would determine when breakage would occur [34]. Dispersion can be decomposed into two means. Erosion, which is the gradual shedding of minor particles over a long time period and rupture, the abrupt fission of agglomerates into a small number of large fragments [35] [36].

Many experiments have been completed studying the dispersion of different polymer systems. Bohin et al. performed shearing experiments in a rotating cone and plate device exploring the infiltration of polydimethlsiloxane into silica agglomerates [34]. Wang and Manas tested modeling techniques using particle tracking in 3-D isothermal elongational flow fields. This was further developed by Cong and Gupta [37][38]. Arrizón et al. studied the dispersion of titanium dioxide in high density polyethylene and found how surfactants modify dispersibility and product quality [39]. This study aided the understanding of the work in this thesis since titanium dioxide and high density polyethylene were both used.

Kao and Mason extensively studied the efficiency of the mechanisms that dominate dispersion [40]. The mechanisms compared were simple (or transverse) and pure (or extensional) shears. An experiment was set up with a four-roller apparatus that controlled the environment so that the species would not naturally disperse. The study used 1mm polymethylmethacrylate spheres immersed in 100 poise silicone oil. Figure 2.2 (a) shows the particles in a simple shear flow and Figure 2.2 (b) in extensional flow.

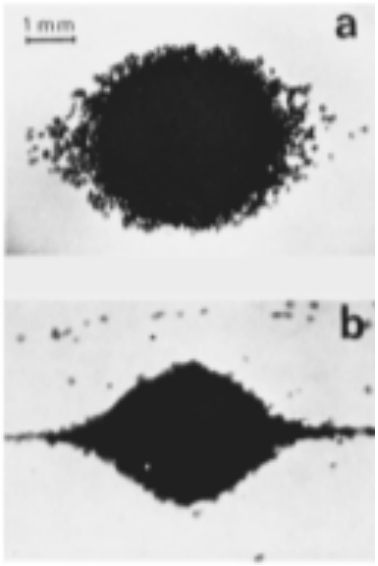

Figure 2.2: Pictures of Agglomerates in (a) Simple Shear and (b) Extensional Shear [40]

Analysis of the break-up led to Equation 2.1 below, which states that the number of spheres that break off the aggregate is proportional to the tensile stress generated by the sheared fluid on its surface.

$$({R_0}^3 - {R_t}^3) = kGt \qquad \textbf{2.1}$$

Where R_t is the aggregate radius, t is the shearing time, and G is the gradient that describes the shearing flows. Flows can be characterized by the constant k, which represents the dispersing efficiency. It was found that the simple shear dispersing efficiency was approximately one third of the extensional flow dispersing efficiency [40].

Dispersion is particularly important in the growing field of advanced polymers, specifically for polymer composites with the inclusion of carbon microfibers and nanotubes, which have shown to have significant impact in augmenting material properties [41][42][43].

2.2 Percent Drag Flow

In contrast to the geometrically grounded industry standard (volumetric approach), the newly proposed scale-up approach is based on percent drag flow (which will be denoted by %DF in figures and captions). The following section defines the concept of percent drag flow and the studies based upon it.

Every screw element possesses some maximum conveying ability per screw revolution, which is related to the pitch of the element [44]. Pitch is defined as the axial length between successive passes of a screw crest, or alternatively the axial distance required to travel a full revolution. In most sections of a TSE, the polymer being conveyed by the elements does not completely fill the element. For a partially filled system, such as a TSE, only a portion of the maximum pumping capability, and therefore drag flow, can be realized. Percent drag flow is the fraction of volumetric flow that is actualized by a particular screw element. The percent drag flow correlates to the flow path of fluid particles traveling through the extruder, which defines its utility to mixing applications [45]. Calculation of percent drag flow is displayed below in Equation 2.2. The variable $(Q/N)_{operating}$ symbolizes the specific throughput of the extruder in its current state, while $(Q/N)_{100\%}$ represents the maximum specific throughput achievable by a particular element in the screw design.

$$\%DF = \frac{\left(\frac{Q}{N}\right)_{operating}}{\left(\frac{Q}{N}\right)_{100\%}} \cdot 100\% \qquad \textbf{2.2}$$

Cheng et al. looked into kneading block performance related to percent drag flow because residence time and fill length are direct functions of percent drag flow.

Experiments were run on a 30-mm CoTSE filled with a viscous corn syrup as a Newtonian fluid and a corn syrup solution to model a viscoelastic fluid. Through the use of a fluorescent dye, image analysis and flow visualization methods, Cheng et al. determined the mixing performance of a kneading block element. A low screw speed of 15 RPM was used to produce the highest quality images. The percent drag flow parameter was varied from 18% to 45% to cover a wide range of shear histories. To quantitatively characterize kneading block performance parameters such as residence time, fill length, and dye intensity after the mixing section were measured [46].

Results produced insight on the relationship between percent drag flow and pertinent performance parameters. First, fill length was directly proportional to percent drag flow until about 30% drag flow. In Figure 2.3 below, it can be seen that at the 30% drag flow there is a "turning point" where the fill length begins to plateau [46].

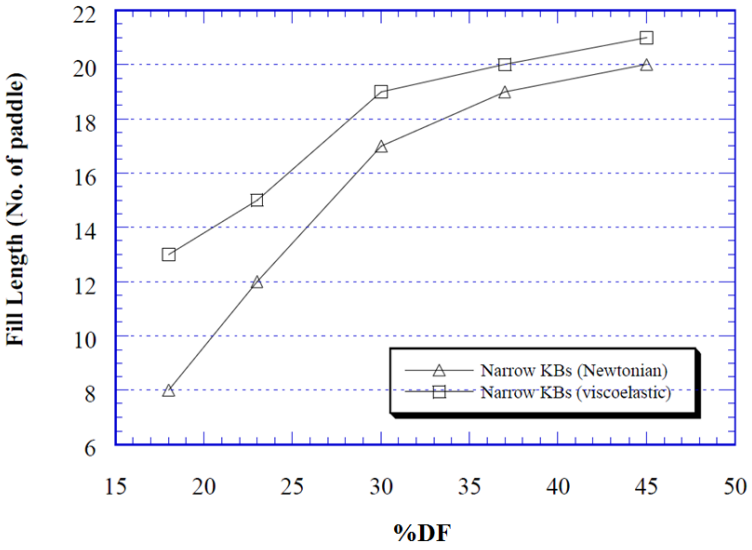

Figure 2.3: Fill Length vs. %DF [46]

Figure 2.3 also shows that the fill length was longer for the viscoelastic fluid in comparison to the Newtonian fluid system for all percent drag flows. For the

Newtonian fluid, there was also a shift at 30% drag flow for residence time. Two terms are necessary to define the residence time, t_{head} and t_{tail}. t_{head} refers to the time between the first moment the dye enters the kneading block elements and the first trace of dye leaving the kneading block elements. On the other hand, t_{tail} is defined as the time period between the first trace of dye and the final trace of dye leaving the kneading block elements. In Figure 2.4 and Figure 2.5 below, t_{head} and t_{tail} are plotted against percent drag flow.

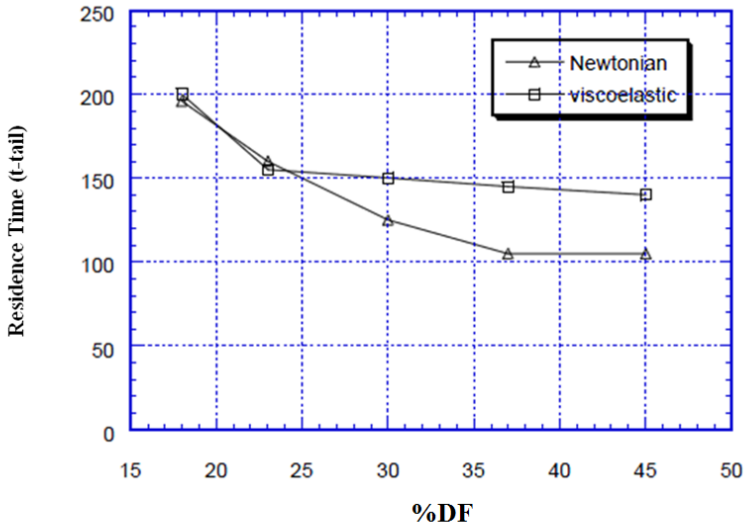

Figure 2.4: t_{tail} vs. %DF [46]

Again, at approximately 30% drag flow, a shift was observed in Figure 2.4. Observation of Figure 2.4 shows only after the 30% drag flow data point there is a greater t_{tail} for the viscoelastic system compared to the Newtonian polymer. In Figure 2.5 the t_{head} is greater at every point for the viscoelastic system.

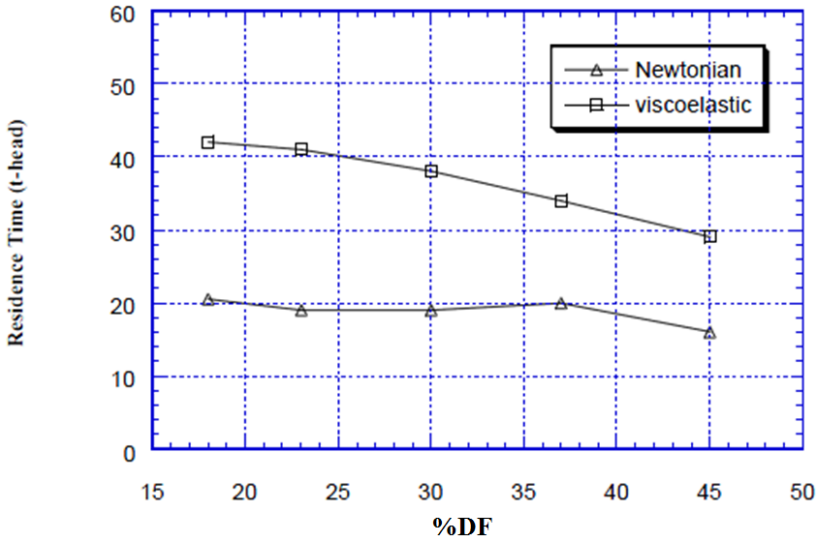

Figure 2.5: t_{head} vs. %DF [46]

Dye intensity results also shows peak intensity after a certain number of screw revolutions, which was then followed by a sharp decline into a steadily decreasing function, seen below in Figure 2.6.

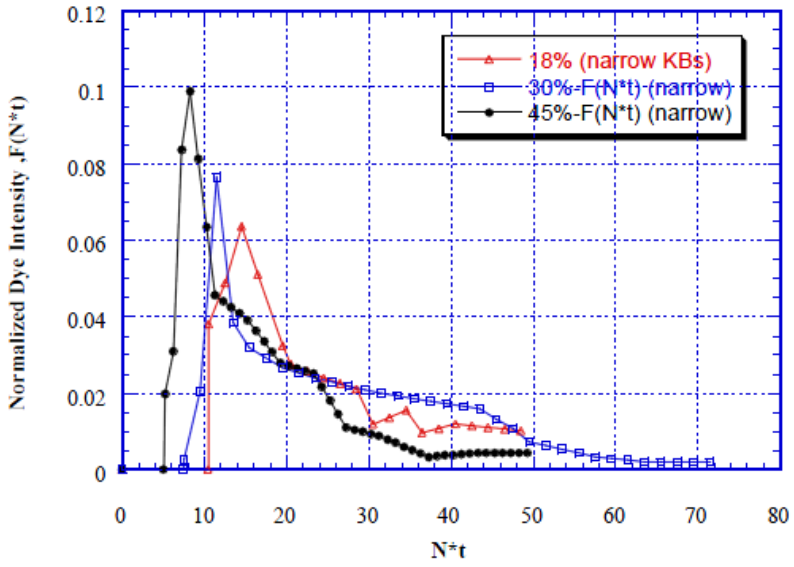

Figure 2.6: Normalized Dye Intensity vs. Screw Revolutions [46]

Cheng et al. found that percent drag flow is a critical parameter when characterizing the mixing performance of kneading block elements.

Other studies have been completed for other extruder sizes and screw configurations that used a similar percent drag flow relationship. Brouwer and Todd examined a 30-mm TSE and characterized different conveying, mixing, and turbine elements by drag flow [47]. Channel depths of screw elements were explored through simulations to show how changes in drag flow affect the shear stress [48]. In addition, Kiani et al. used numerical models to find the optimized conveying capability for various screw geometries with altered mixing sections [49].

2.3 Residence Time Distribution

The RTD describes the amount of time it takes a fluid particle, along a streamline, to travel through the extruder. The distribution of the various paths and respective travel times is due to the non-uniform velocity field that exists across the screw channel [50][51]. The measurement of the RTD can be off-line, in-line, or numerically modeled. For example, a common off-line measurement technique involves the injection of a tracer material into the extruder and digital image processing analysis of the tracer concentration along the extrudate [52]. Off-line methods are often time consuming but have the advantage of not requiring probes and data acquisition systems.

In-line methods determine the RTDs in real time through the use of sensor and a data acquisition system. One example of in-line method was through an infrared temperature probe to detect heat drop, due to the change in surface emissivity from the injection of carbon black into the polymer [53]. Another example of an in-line method for RTD determination is the use of an ultrasonic transducer. Sun et al. compounded low density polyethylene with a $CaCo_3$ powder, where the ultrasonic

attenuation caused by the $CaCo_3$ made it a viable tracer to the ultrasonic transducer [54]. Similar in-line studies were performed by Chen et al. with a technique that measured light transmittance through a photomultiplier [55].

There have also been many numerical models developed to describe experimental RTDs. Puaux et al. experimentally determined RTDs using an iron powder tracer and measured magnetic susceptibility through an in-line signal system. Puaux fitted the data curves using different one, two, and three parameter models to find the most statistically relevant scheme. The results found that the three-parameter backflow cell and two-parameter delayed axial dispersion models to be the most efficient [56].

Important mixing relationships have been determined from both experimental RTDs and numerical models of RTDs. From a modeling perspective, David B. Todd correlated the cumulative probability distribution of a RTD to the Peclet number and related it to surface generation and axial mixing through different pitched elements. In this study Todd explored a devolatilization process where, maximized surface generation and minimized axial mixing was ideal. These results can be extrapolated to general polymerization processes as well. By lowering the Peclet number and using screw elements with intermediate helical angles, high degrees of axial mixing can be achieved [57]. Todd further experimented with materials of varying viscosities to demonstrate the applications of RTDs as a basis for scale-up based on Jeffrey's number.

Another mathematical model employed by Bigg et al. and Pinto et al. related RTDs to a weighted average total strain for different power law fluids. In liquid-liquid systems the quality of distributive mixing is a function of the amount of strain

the material experiences [51][58]. Spencer and Wiley defined this concept by correlating laminar flow mixing with increasing the surface area between the fluids across the entire volume [19]. Bigg plotted the weighted average strain against a dimensionless total flow rate term that displayed a logarithmic decay of strain values with an increase in flow rate. Although these were numerical tests, they provide insight into methods of correlating operating variables with measures of mixing.

Shearer and Tzoganakis used another method relating distributive mixing to the RTD through the measurement of conversions between two reactive polymer tracers. The number of conversions was directly proportional to the degree of distributive mixing as the two polymers would react more strongly along areas of stretching [59].

The second experiment performed by Shearer and Tzoganakis determined the residence times of various types of screw elements. Investigation of different kneading block elements, distinguishable by their pitch, showed a decreasing trend in residence time from reverse, neutral, to forward kneading block elements. Note that the difference in times between the various kneading block elements decreased as flow rate was increased. It was also established that total residence time is an additive sum of all the local residence times. In comparison of conveying elements versus kneading block elements, different sections of the screw were explored. For the purely conveying section there was a strong correlation between residence time and number of conversions. This result aligned with the result that the number of conversions grew when the flow rate was increased, and showed that conveying elements were most sensitive to fill. Since conveying elements are partially filled as the fill tends toward full, resultant shear rates will increase and a negative pressure

flow component will augment distributive mixing. Since the kneading block elements are fully filled, the distributive mixing was a function of average local residence time and screw speed, which relate to the number of revolutions experienced by the material. For a kneading block element section, a greater number of revolutions correlated to a higher probability that a material would move through apex stress regions [60].

Along with tying the RTD to different mixing geometries, Kao and Allison produced a comprehensive RTD study relating the distribution to throughput and screw speed. They concluded that throughput was the most significant factor to the residence time, and that there was a decrease in the mean residence time with increasing screw speed. Additionally, mean residence time was found to be independent of barrel temperature [61]. Kim and White also studied screw configuration and operating condition relationships with RTDs. They found the increase of mean residence time with left-handed or kneading block elements, and how the screw speed not only decreased mean residence time but also the variance of the RTD [62].

Many studies aim at producing predictive models for RTD due to the information that can be extracted from the RTD. Kiani et al. studied a CoTSE 40-mm using in-line RTD measurements and finite element techniques to develop optimization tools for various screw geometries [63]. Furthermore, Chen et al. studied the RTD in extruders using statistical theory and the relationships between the subsystems by the convolution integral [64].

In processes such as reactive extrusion, the time the material spends in the extruder is critical to the reactive kinetics. However, in processes that are not time dependent and more mixing dependent it is valuable to understand other residence distributions or kinematic pictures.

2.4 Residence Volume and Residence Revolution Distributions

Gao et al. experimentally measured RTD curves using a tracer and reflective optical probe and converted those distributions into different domains. By taking the time parameter from the RTD and transforming it to as *n/N*, where *n* = screw revolutions and *N* = screw speed, the RTD can be transformed into a RRD. Similarly, the time parameter can be represented as V/Q, where *V* = volume and *Q* = volumetric flow rate (throughput), altering the RTD into a RVD. The equations for RRD and RVD respectively are shown below in Equation 2.3 and Equation 2.4.

$$h(n) = \frac{c\left(\frac{n}{N}\right)}{\int_0^\infty \left|c\left(\frac{n}{N}\right)\right| dn} \quad \textbf{2.3}$$

$$g(v) = \frac{c\left(\frac{v}{Q}\right)}{\int_0^\infty \left|c\left(\frac{v}{Q}\right)\right| dv} \quad \textbf{2.4}$$

The functions *h(n)* and *g(v)* represent the RRD and the RVD, respectively. The screw speed is *N* measured in RPM. *Q* is the throughput measured in liter/min. Then *n* and *v* are the number of revolutions and extrudate volumes after the tracer has been introduced.

Understanding extrudate volume and number of revolutions can be critical to the degree of mixing achieved. Additionally, the degree of mixing in these domains can be related to operating conditions. Finally, a key parameter was found through comparison of the three domains. In the RTD plot in Figure 2.7, conditions 1, 7, and 11 are all different with respect to delay time and shape. Yet, in the RVD and RRD domain, Figure 2.8 and Figure 2.9 respectively, curves 1, 7, and 11 are identical, superimposed on top of each other. The common factor between each curve is *Q/N*, or specific throughput. Identical *Q/N* curves show that, when specific throughput is constant, the fluid particle flow paths are the same. Results showed that RTDs give limited insight into mixing but the specific throughput (also known as degree of fill) has a direct correlation, since flow path can be connected to mixing [17] [18][65].

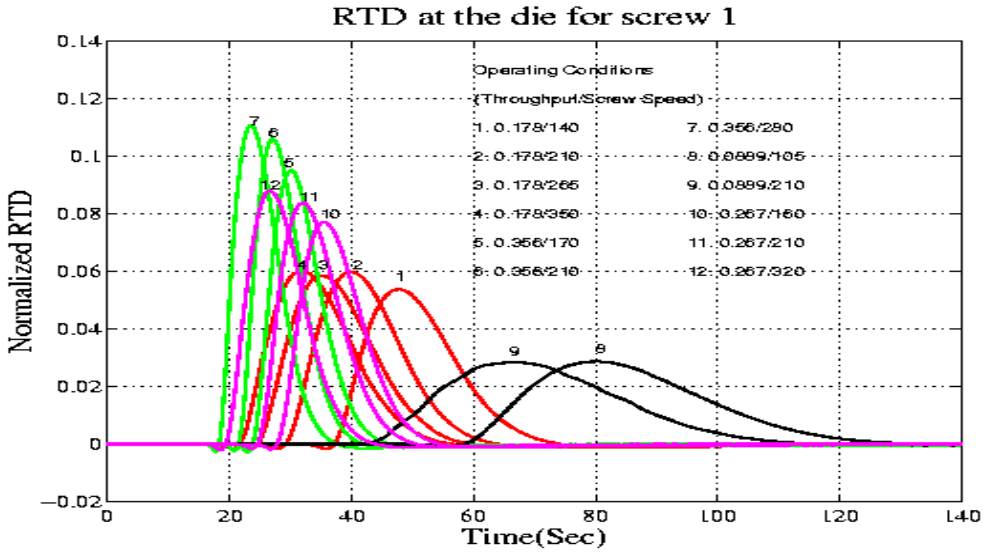

Figure 2.7: Experimental RTD Curves [17]

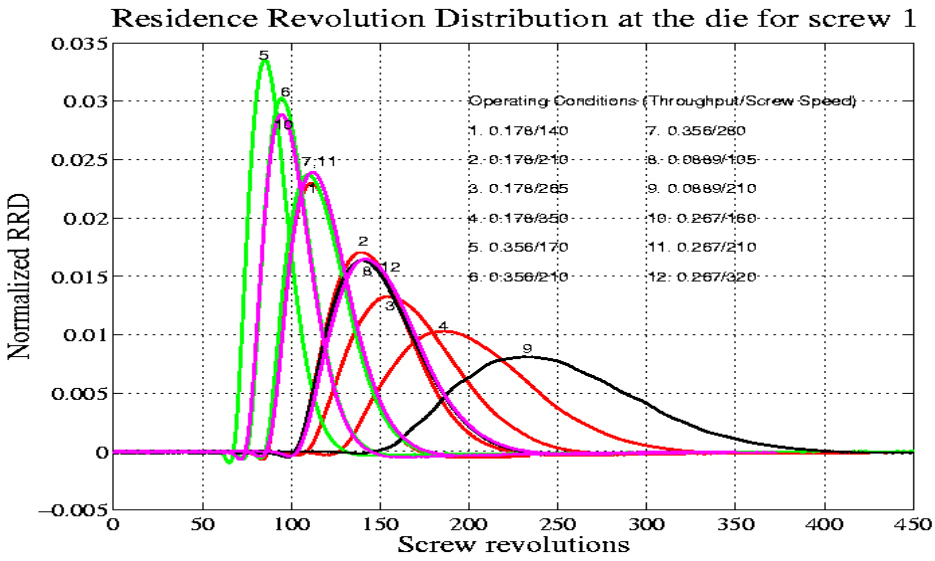

Figure 2.8: Residence Revolution Distribution Domain [17]

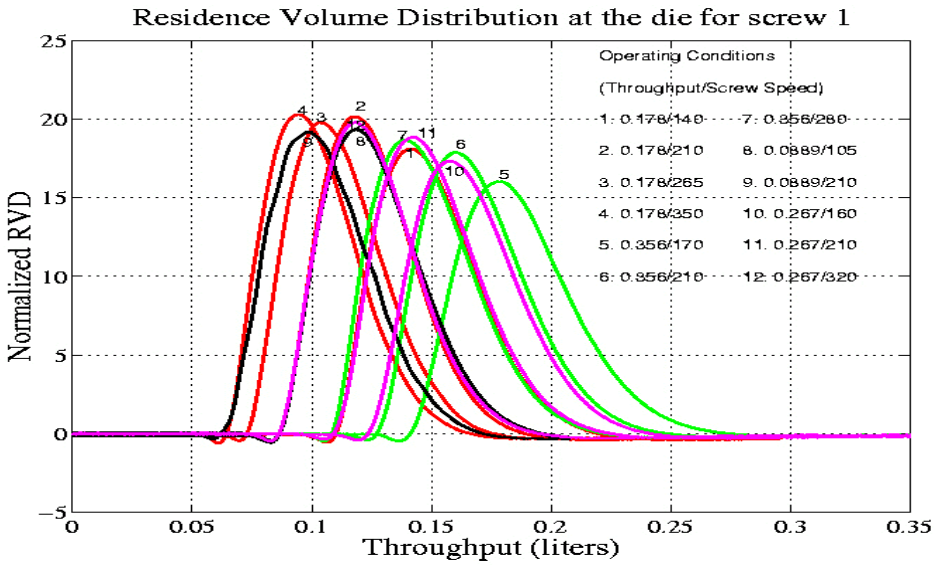

Figure 2.9: Residence Volume Distribution Domain [17]

2.5 Stress History

Previous studies on the stress history within a TSE have been very limited. Curry et al. provided the most comprehensive research prior to the methodology presented in this thesis. Curry et al. stated that the understanding of the stress history examines dispersion of agglomerates and minor phases within a compounding process [9][66].

Curry's experiment used hollow glass spheres as a stress sensitive tracer in a viscous fluid system. The hollow glass spheres were effective because they had a smooth shape, low interfacial tension, well-defined diameter and wall thickness, and ruptured at moderate loads. Furthermore, the spheres, manufactured by 3M, had a variable rupture stress, dependent on compressive strength. The viscous fluid studied was polybutene, which was ideal because it was a Newtonian fluid, lacked a volatile component, and could encompass the glass spheres. Stress imparted on the spheres could be altered through a change in the polybutene viscosity along with the process's operating conditions. Two different grades of polybutene and three different glass sphere strengths were used in this study. Table 2.1 displays the different grades of the polybutene and Table 2.2 shows the different glass sphere grades [9][66].

Table 2.1: Polybutene Information [9]

Fluid Grade	Viscosity [Pa-Sec 10 Sec^{-1}] at 25°	Density [g/cc] at 25°
H300	709	0.902
H-1500	87	0.902

Table 2.2: Glass Sphere Information [9]

Sphere Grade	Compressive Strength at 10% Failure [Mpa]	Sphere Density [g/cc]
A16	3.51	0.16
A20	7.03	0.20

The TSE used in this experiment was a ZSK-40 CoTSE with a screw diameter of 40 mm. Two different screw designs were tested. Screw 1's geometry was dominated by left-handed elements. Screw 2's geometry was comprised of mainly kneading block elements. The runs performed on the ZSK-40 were all held at a constant flow rate

with an incrementally increasing screw speed. The exact operating conditions are detailed in Table 2.3.

Table 2.3: Experimental Operating Conditions [9]

Mass Flow Rate [lb/hr]	Screw Speed [RPM]
50	80
50	150
50	350

Results of the experiment correlated well with established phenomena observed in the polymer processing industry. With a greater screw speed (shear rate) a greater percentage of glass spheres broke, and a more viscous grade of polybutene always broke a greater percentage of spheres. As expected, spheres with lower thresholds of compressive strength broke more easily. Comparison of the screw configurations showed that Screw 1 (dominated by left-handed elements) was more aggressive in rupturing the glass spheres than Screw 2 (dominated by kneading block elements). Figure 2.10 shows the data collected for all varied parameters [9][66].

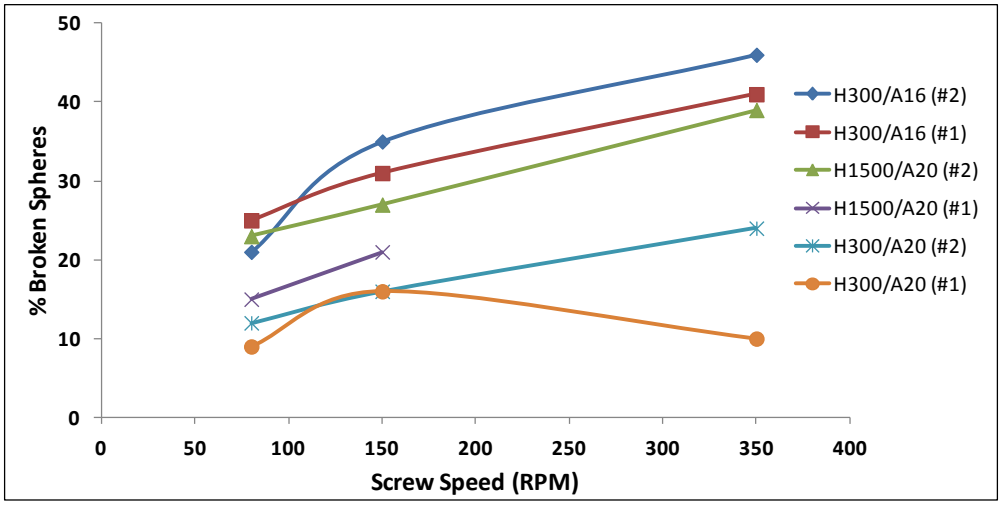

Figure 2.10: Results of Glass Sphere Experiment [9]

These results assumed that the failure mode of the spheres was shear driven. If this is the case then it would be expected that beads break in clearance areas along the screws, or where the distance between the screws and barrel walls is smallest. The left-handed element geometry produced five and a half more passes through clearance areas, which is why Screw 1 broke a greater percentage of spheres than Screw 2.

Through the use of hollow glass spheres, Curry et al. performed an initial study that led to future experiments investigating the stress history of compounding operations. The study was able to compare polymer systems, screw configurations, and different sphere strengths.

This technique was effective, but the calculation of percent rupture of the glass spheres was difficult. In Figure 2.10 there is one curve, H300/A20, which does not fit with the rest of the results. The spheres saw a greater percent break-up at a lower shear rate, which is unrealistic. This could be a result due to human error. In this study, percent rupture was calculated by removing the screws and manually counting the number of ruptured spheres along the cured polymer carcass. This method of break-up determination was inaccurate and time intensive.

At the University of Maryland-College Park a new real-time measurement RSD methodology has been developed. Instead of hollow glass spheres, polymeric stress beads were used. The benefit to this methodology was the dye tracer encapsulated by the hollow spheres was used to measure the RTD. Thus, the tracer represented 100% break-up of the stress beads, which allowed for easy calculation of percent rupture based on the areas underneath the RTD and RSD curves. Various studies have been

completed studying different grades of stress beads, screw geometries, and ranges of operating conditions [67][68][10].

2.6 Scale-Up Background

The principle idea of scale up is based on the concept of similarity. The similarity axiom states that all physical and technical facts are kept constant by dimensionless terms known as π (pi) terms [11]. A more comprehensive examination of the derivations and mathematics involved in the scale-up approach proposed in this thesis will be outlined in Chapter 4. The following literature shows the range of methodologies applied to scale-up in the extrusion industry.

J.F. Carley and J.M. McKelvey wrote one of the earliest and most cited scale-up papers in 1953 titled *Extruder Scale-Up Theory and Experiments*. They addressed the scale-up issue for SSEs and how it can be applied to adiabatic extruders. An adiabatic extruder is defined as having no external heat flow. Thus, the heat generation only comes from the shearing of the solid thermoplastic. Pertinent information from this study was the derivation of scale-up rules for extruders. All scale-up rules start with the similarity theorem. The similarity theorem states that processes need to be isothermal and geometrically similar. Although heat transfer is realistically never constant throughout the entire length of the screw, certain sections can be controlled and scaled. Carley and McKelvey began the derivation with the net flow equation for a SSE, shown below in Equation 2.5. Normally, the flow equation would end with the term, $\Delta P/dL$, but since only local scale-ups are being considered that term was replaced with $dP/d\lambda$, the pressure gradient at a specified point [69].

$$Q = \alpha - \frac{\beta + \gamma}{\mu} \cdot \frac{dP}{d\lambda} \qquad \textbf{2.5}$$

Where α represents the drag flow and the term containing $dP/d\lambda$ is the pressure flow. The summation of the drag flow and pressure flow equals the net throughput. Consider scaling-up two geometrically similar extruders that pump the same material, one large and one small, where the larger extruder is *x* times greater in all dimensions. Convention states that *x* is called the scale-up factor, which was derived as the ratio of the two outer screw diameters in the Carley and McKelvey study. Therefore any point on the smaller extruder that is at a distance λ will correspond to a point on the larger extruder at a distance $x\lambda$ [69]. Shear rates are kept constant between the two machines. Shear rates require no scaling factor resulting from the concept of two geometrically similar extruders. When the ratio of the two outer screw diameters, *D*, is proportional to the ratio of the channel height, *H*, then mathematically the shear rates scale 1:1. Proof of constant shear rate through geometric similarity is shown in full detail in Chapter 4. Derivations also assume that the polymer melt is incompressible implying that the total forward flow will be the same at all points. With all of the assumptions stated, scale-up factors raised to a calculated power are determined for all the parameters involved in Equation 2.5. The scaled parameters are then used in conjunction with the constant viscosity between processes and the relationship between the pressure gradient and flow rate to determine practical scale-up rules. Derived scale-up rules found the pressure differentials to be the same, but the net throughput and power consumption will scale by the ratio of the two outer

screw diameters (x in Carley and McKelvey's Study) cubed [69]. A full derivation of the throughput scale-up is provided in Chapter 4.

Scaling-up through dimensionless parameters and the similarity theorem can be described as a fluid mechanics approach. However, scale-up has been addressed through alternative perspectives. A. Gaspar-Cunha and J.A. Covas treated scale-up as a multi-objective optimization problem where the goal was to minimize certain negative attributes for specified performance parameters [70]. The process involved five steps: (1) For a specified operating condition and screw geometry; determine the heat transfer and flow in the model extruder; (2) Establish critical performance parameters; (3) Assign input values for parameters in the model scale process; (4) Execute optimization algorithm; (5) Make a final decision based on published results. Paretor Frontiers were generated for three experimental runs. These frontiers showed the trade-off behavior that existed between the various performance parameters. The parameters investigated were the ratio between average melt to barrel temperature, viscous dissipation, and specific mechanical energy. Gaspar-Cunha and Covas found that framing scale-up as a multi-objective optimization problem was a valid decision making process. Analysis through the Pareto Frontiers provided a customized scale-up based on the user's preferences.

Characterization of the heat transfer is key to understanding extrusion and can be used to scale-up model processes as well [4]. In SSEs, the rotation of the screw causes viscous heating through a shearing motion. The transfer of energy from the turning screw and any external heating source coming from the barrels generates an increase in enthalpy of the polymer [71]. Further downstream in the extrusion

process, after the polymer exits the die zone, the material is cooled thereby reducing the enthalpy. The energy balance in a SSE comprises four components: (1) mechanical work; (2) barrel heating/cooling; (3) enthalpy change in the polymer; (4) and heat losses [71]. As the screw speed increases less barrel heat is necessary to balance the energy. As the limit of the screw speed tends towards infinity the barrel heat needed goes to zero, and the process becomes adiabatic. Scale-up with respect to heat transfer is a function of the interfacial contact area between the polymer and barrel walls. Surface area scales by the ratio of the extruder diameters squared, but volume scales by the power of three. Thus as the process approaches an adiabatic condition the scaling factor increases proportionally closer to a diameter ratio cubed.

J.A. Colbert determined scaling factors for various process parameters through the use of three dimensionless parameters: the Graetz number, the Griffith number, and volumetric efficiency. The Graetz number describes the convection from one end to the other end of a screw channel. The Griffith number represents the temperature differential across the screw channel due to viscous flow. The volumetric efficiency term is defined as the net throughput divided by the peripheral screw speed, which is the screw speed multiplied with the outer screw circumference, multiplied by the channel width and height [71]. When the three dimensionless parameters are kept constant and substituted into the power law equation for viscosity (Equation 2.6) a number of scale-up factors can be determined for a range of process parameters. Table 2.4 shows the scale-up rules for certain variables with respect to the ratio of the two screw diameters, for both Newtonian and Non-Newtonian fluids.

$$Viscosity = Constant \cdot (Shear\ Rate)^{n-1} \quad \textbf{2.6}$$

Table 2.4: Scale-Up Factors [71]

Parameter	Newtonian	Non-Newtonian
Channel Depth	$D^{1/2}$	$D^{(n+1/n+3)}$
Screw Length	D^{0}	D^{0}
Channel Width	D^{0}	D^{0}
Screw Speed	D^{-1}	$D^{(-2n-2/3n+1)}$
Throughput	$D^{3/2}$	$D^{(5n+1/3n+1)}$
Power	$D^{3/2}$	$D^{(5n+1/3n+1)}$
Specific Throughput	$D^{5/2}$	$D^{(7n+1/3n+1)}$

Although the study was based on a SSE it still provided insight into scale-up determined through heat transfer and the energy balance equation.

Another methodology in predicting the behavior in larger extruders was performed through the use of simulation models. Zhu et al. showed that 1-D modeling becomes more inaccurate as the screw diameter increases. Zhu's 3-D numerical simulation was shown to be more capable in characterizing the polymerization progression within a CoTSE for a reactive extrusion process. Reactive extrusion involves materials that are bonded chemically. Thus, it is critical to understand the conversion efficiency along the axial length because the procedure involves a chemical reaction. Through the simulation, it was determined that there was a greater conversion for a larger screw diameter and increased screw speed [72]. It was also shown that although the 1-D simulation was comparable for smaller screw diameters, once the process was scaled-up and screw speed increased the 3-D simulation became more reliable in predicting polymerization [72]. Although the flow within a CoTSE is complex, Zhu demonstrated that using numerical simulations could be a predictive methodology for predicting heat transfer behavior for industrial sized processes.

Therefore, beyond experimental approaches, modeling techniques can be used to address the scale-up issue.

Chapter 3 Experimental Set-Up

The following sections outline the equipment, materials, and procedures that were used in this study. The experiments were completed at three separate sites: The University of Maryland Advanced Manufacturing Laboratory, DuPont Experimental Station, and the Coperion Corporation Headquarters. For convenience each extruder will be named according to its outer screw diameter length.

3.1 Equipment

Three different sized extruders were used to complete all the experiments performed for this study. The 28-mm at the University of Maryland was used to show reliability of the RSD methodology. The 18-mm at the DuPont Experimental Station was used as the "model" sized extruder and the scaled-up 26-mm was the "industrial" sized extruder at Coperion. The 18-mm was also used to show the versatility of the DOE approach, prior to the scale-up experiments.

3.1.1 Twin-Screw Extruders

3.1.1.1 28-mm Twin-Screw Extruder Set-Up

The extruder used at the Advanced Manufacturing Lab at the University of Maryland is a Coperion ZDSK-28 co-rotating, fully intermeshing CoTSE. The outer screw diameter measured 28 mm, and it was a tri-lobal CoTSE. The length to diameter ratio (*L/D*) was 32.

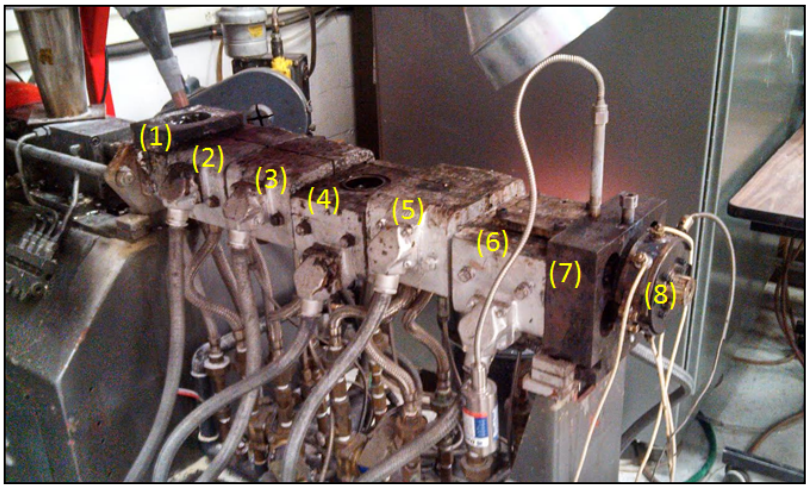

Figure 3.1: 28-mm Coperion ZDSK CoTSE

The extruder was comprised of eight sections. Polymer entered at the feed port (1). The next five sections are the barrel zones (2-6), which are used to heat the polymer to the melting point so that the material and any extra fillers easily flow through the channels of the screws. Barrel zone 4 (5) has a vent port, kept open to inject the stress beads or dye shots. The temperature profile of the machine, from barrel zones 1-5, was kept constant at 200°C. The second to last section is the optical probe housing and is known as the block (7). The block also connects the eighth section to the extruder. The eighth section was the die zone (8). The die zone was the exit for the compounded polymer. Die geometry can vary depending on the insert selected. The die geometry used for this study was a slit die, which had a thin rectangular cross section with a diameter of 25 mm and a thickness of 1 mm, seen below in

Figure 3.2. The die zone, for all experiments, was kept at a constant temperature of 190°C.

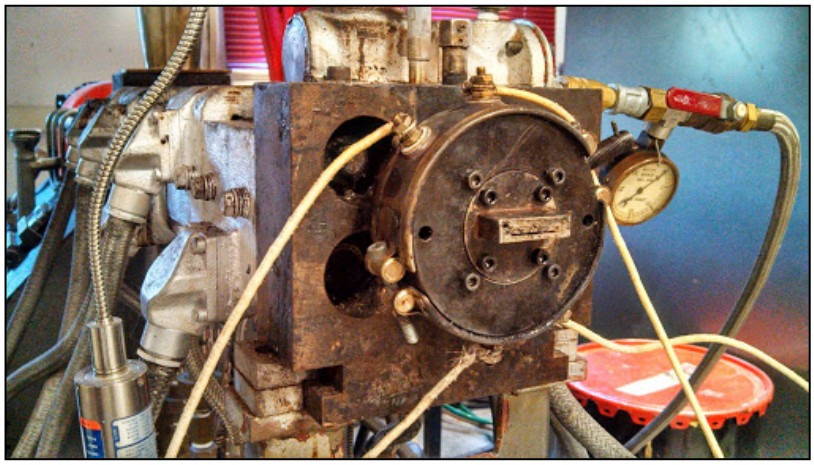

Figure 3.2: Front View of Slit Die

The extruder was operated by a FACTS MI – 101 control system with a digital touch-screen control panel, seen in Figure 3.3. The control panel was used to set the temperatures for the barrel and the die zone, along with controlling the speed of the screws. The screws have a maximum speed of 300 RPM. The manual controls, found directly below the touch-screen, included a dial that operated the screw speed, on/off buttons, and an emergency stop.

Figure 3.3: FACTS MI – 101 Control System

The hopper controls the feed rate. The base polymer used in this study was in pellet form, which dictated the type of hopper and feeder screw needed. Figure 3.4 shows a laboratory scale K-TRON loss-in-weight feeder, which utilized a set of twin-screws to feed the pellets. The feeder was positioned above the extruder and connected to the feed port through a funnel-tube system as shown in Figure 3.4.

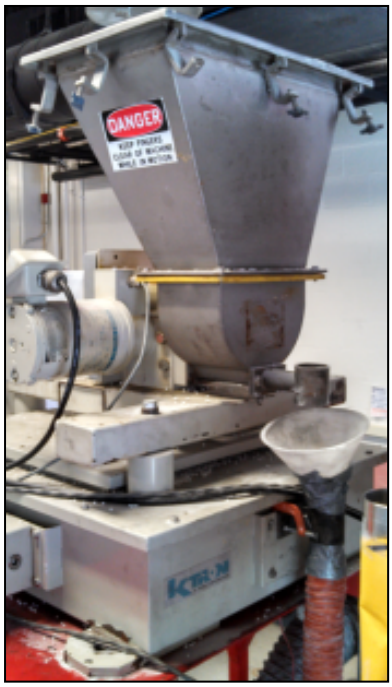

Figure 3.4: K-TRON Loss-in-weight Feeder

The feeder was controlled by a KCM control system, the system enabled the operator to set desired mass flow rates. The maximum feed rate of the two K-TRON feeders was approximately 10 lb/hr. Figure 3.5 is a picture of the KCM control system.

Figure 3.5: KCM Control System for both the Pellet and Powder K-TRON Feeders

No samples were collected because the research focused on the stress behavior inside the extruder. Thus, no downstream post-processing machines were used.

3.1.1.2 18-mm Twin-Screw Extruder Set-Up

In order to test scale-up a laboratory sized extruder was needed. The 18-mm CoTSE at the Experimental Research Station at DuPont located in Wilmington, DE served as the model sized extruder. The extruder used was a Coperion ZSK-18 Megalab fully intermeshing, CoTSE. The extruder had a diameter of 18 mm and an *L/D* ratio of 40. Unlike the 28-mm machine this extruder had only two flights. The 18-mm extruder had a consistent temperature profile of 200°C for all nine-barrel sections, like the 28-mm. Similar to the 28-mm an open port located directly before the mixing section was used for injections. The optical probe was inserted immediately after the mixing section, which varied from the 28-mm set-up, where the probe was located further downstream directly before the die zone.

3.1.1.3 26-mm Twin-Screw Extruder Set-Up

The extruder that was used as the larger extruder in the scale-up study was at Coperion Inc. headquarters in Ramsey, NJ. The extruder used was a Coperion ZSK-26 MC fully intermeshing CoTSE. The screws had a diameter of 26 mm and had an *L/D* ratio of 37. Like the DuPont machine the 26-mm was bi-lobal, making the two machines geometrically similar. The temperature profile was also kept the same as the 18-mm, at 200°C for all nine-barrel sections.

3.1.2 Screw Geometries

The RSD methodology enabled the stress history characterization of various screw configurations. This thesis shows how the RSD methodology can be applied to different sized extruders. Numerous screw geometries were utilized for the three different sized extruders used in this research.

There are three main zones in a TSE design that were studied for this research; melting, conveying, mixing, and backpressure. For all studies, two different types of mixing sections were implemented. One used a set of wide kneading blocks backed by a reverse element and the other used a set of narrow kneading blocks backed by a reverse element. Furthermore, the reverse element remained constant for all mixing sections. All screw geometries used one complete left-handed element, pitch dependent on the extruder.

The melting zone, which was used to change the solid plastic pellets into a melt flow, was also kept constant for each extruder. The conveying zone takes the melt flow and transports it to the mixing section. Although the mixing is mild in this section it was found to play a role in the amount of stress the material experiences.

The pitch of the conveying element was altered between the 18-mm and 26-mm CoTSEs to study the effects. However, the 28-mm only studied changes in the mixing section, since the experiments performed on the 28-mm were purposed to show the consistency of the stress bead methodology.

Screw geometries will be named systematically for easier reading. Each screw geometry will be titled Screw 'Extruder Screw Diameter (mm)/Kneading Block (KB) (disc size)/Conveying Element Pitch (mm)'.

The screw geometries are grouped by the experiment they were used for. The first section outlines the bead strength research, which was only performed on the 28-mm. The next step in validating the RSD methodology was to study the robustness of the DOE approach. All experiments that pertained to this research were completed on the 18-mm.

The next group of experiments was the scale-up study. Two extruders were used. The 18-mm represented the model or laboratory sized extruder and the 26-mm the scaled-up industrial sized machine. The 28-mm was not studied because it was a tri-lobal CoTSE and dissimilar to the 18-mm and 26-mm CoTSEs, which were bi-lobal.

The final set of screw designs were unlike all of the rest because they were used for a supplemental set of experiments, determining the 100% drag flow of pertinent screw elements.

Numerous amounts of screw geometries were investigated on the 18-mm and 26-mm extruders; therefore, specific details of the screw elements that make up those configurations are referenced in Appendix A. Since there were only two screw configurations on the 28-mm, a table is provided in the section below.

3.1.2.1 The Effect of Bead Strength Screw Configurations

At the Advanced Manufacturing Laboratory at the University of Maryland experiments were performed on a tri-lobal fully intermeshing CoTSE. Two screw designs were implemented in an effort to advance the rigor of the stress bead methodology. The experiment involved testing multiple strengths or grades of stress beads. The two screw configurations were used, distinguishable by their mixing section. Raw thermoplastic pellets entered the 28-mm at point A; while the dye and stress beads were injected at point B, both labeled on Figure 3.6. These entry points did not change with screw geometry alterations.

Figure 3.6 displays the first screw geometry, Screw 28/Wide/24, which had the more aggressive mixing section, comprised of only wide kneading block elements. A full-pitched reverse element was used to provide the backpressure and fully fill the mixing section. Since only two screw geometries were used on the 28-mm CoTSE all the elements are annotated directly on Figure 3.6 and Figure 3.7 below. The labels indicate the axial pitch/axial length of the element as well as the handedness. Additionally, in parentheses the number of elements that comprise the bracketed length is defined.

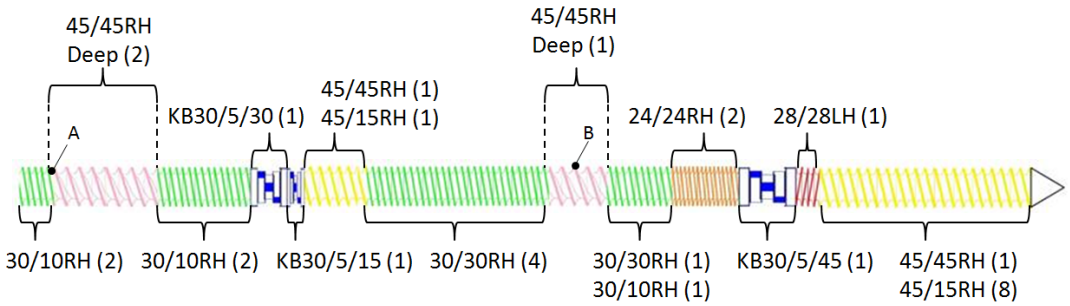

Figure 3.6: Screw 28/Wide/24

The next geometry, the milder mixer, used only narrow kneading block elements. Screw 28/Narrow/24 depicted in Figure 3.7, can be seen below. Outside of the mixing section the rest of the screw was chosen to mirror Screw 28/Wide/24.

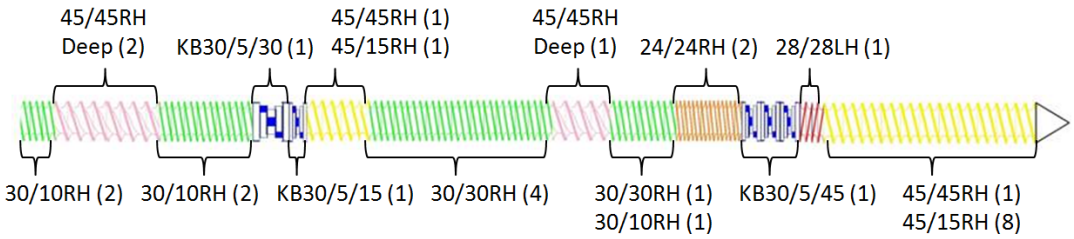

Figure 3.7: Screw 28/Narrow/24

3.1.2.2 Robust Design of Experiment Approach Screw Geometries

In addition to the bead strength study the DOE approach was also modified to examine its robustness. The experiments executed to complete this study were done on the 18-mm CoTSE. Two screw geometries were used for this study. Like the bead strength study, only the mixing section was altered. Furthermore, like the bead strength experiments, the two mixing sections used were composed of a set of wide kneading blocks and narrow kneading blocks. Figure 3.8 and Figure 3.9 show the two screw designs used for the robust DOE study. Figure 3.8 shows Screw 18/Narrow/16 and Figure 3.9 displays Screw 18/Wide/16, the designs vary in mixing section but are identical elsewhere. Figure 3.8 also shows the entry point of the raw plastic pellets at point A, and the point where the ink or stress bead shots were introduced at point B.

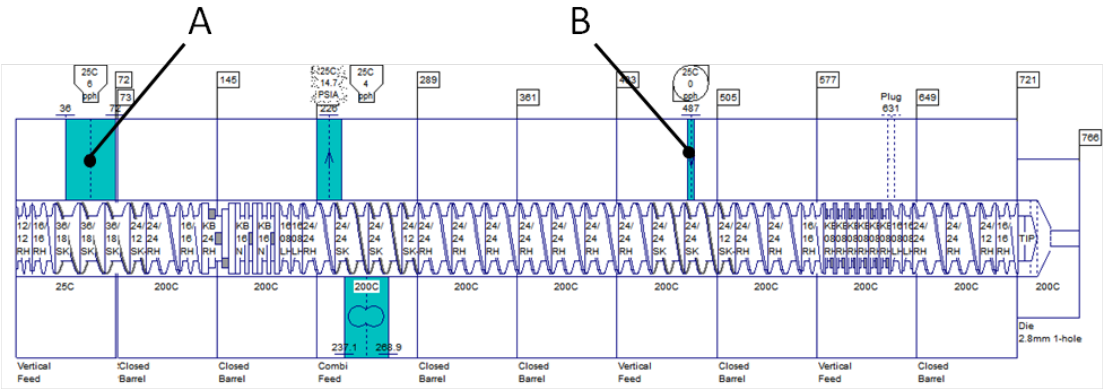

Figure 3.8: Screw 18/Narrow/16

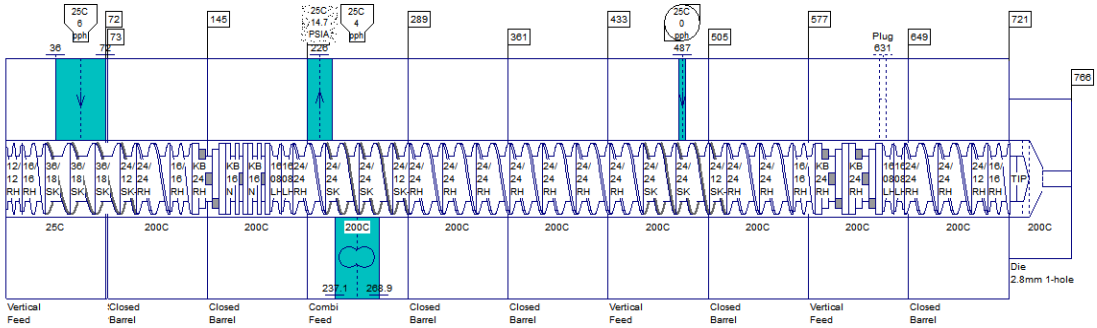

Figure 3.9: Screw 18/Wide/16

3.1.2.3 Scale-Up Phase 1 Screw Geometries

After the methodology was proved to be a reliable method for characterizing the stress history within a TSE, the technique was applied to the scale-up problem. Each phase of the scale-up experiment included screw configurations on the 18-mm and 26-mm extruders. For Phase 1, the screw geometries on the 18-mm were copied from the robust DOE approach experiments, shown above in Figure 3.8 and Figure 3.9. Those two designs were then scaled-up to the 26-mm extruder, shown in Figure 3.10 and Figure 3.11. Figure 3.10 has markings for the hopper feed and where the dye and stress beads were injected. The red arrow indicates where the feed port was, and the purple arrow shows the open vent port used for the injections.

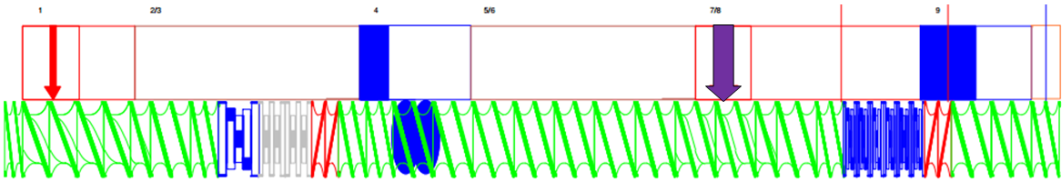

Figure 3.10: Screw 26/Narrow/24

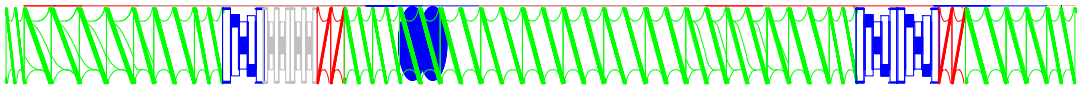

Figure 3.11: Screw 26/Wide/24

It should be noted that although these geometries have a specific pitch fronting (directly upstream) the mixing section, the conveying section was not being studied in Phase 1.

3.1.2.4 Experimental Drag Flow Geometries

Prior to the scale-up Phase 2 experimental runs an intermediary experiment was performed to determine the 100% drag flow of certain elements experimentally. Five different element types were studied. Three elements were characterized on the 18-mm extruder, and two different elements on the 26-mm extruder. The motor of the extruder limited the number of elements tested per extruder. Results and prior experimental drag flow work are recorded in Chapter 5. The labeling for the following screws will be slightly different due to their unique nature. Each screw will be named 'Screw X/Y' where the X will refer to the extruder size the experiment was performed on, and Y will be the element being studied.

The screw designs for the experimental drag flow tests are quite different than the general purpose compounding screws seen earlier. The element in question must completely span between two pressure probes and have no reverse elements.

On the 18-mm, three different elements were investigated: the KB45/5/08 mixing element in Figure 3.12, the 16/16RH conveying element in Figure 3.13, and the 12/12RH conveying element seen in Figure 3.14.

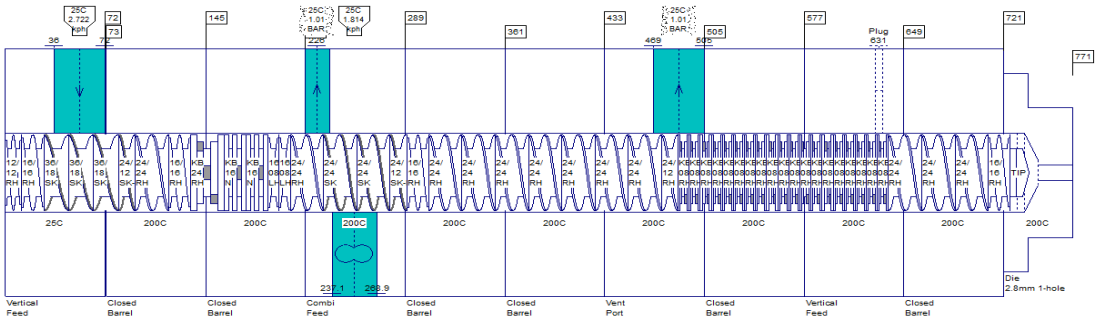

Figure 3.12: Screw 18/(KB45/5/08)

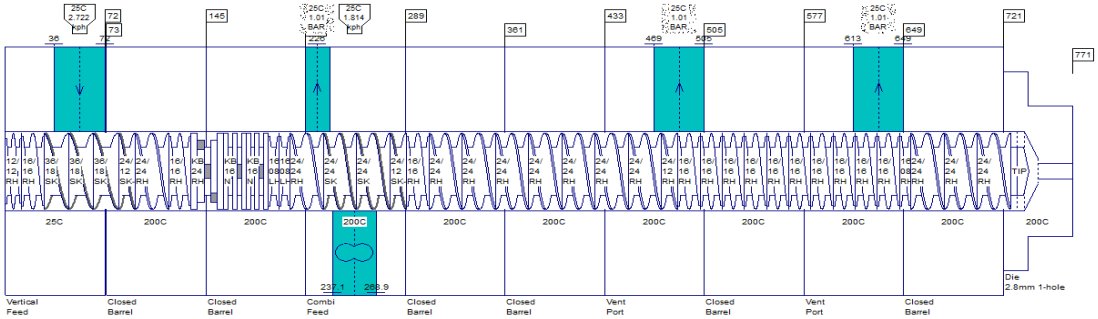

Figure 3.13: Screw 18/(16/16RH)

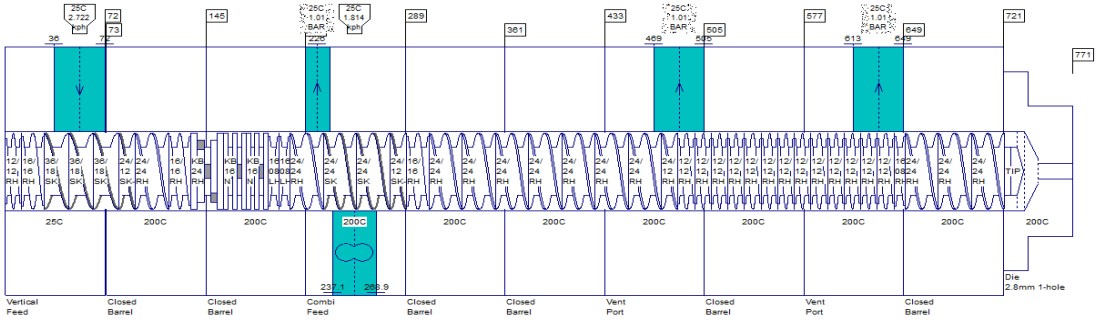

Figure 3.14: Screw 18/(12/12RH)

On the industrial sized extruder, the 26-mm, two experimental drag flow tests were performed. The mixing element examined was the KB45/5/12 seen in Figure 3.15 and the conveying element analyzed was the 16/16RH shown in Figure 3.16.

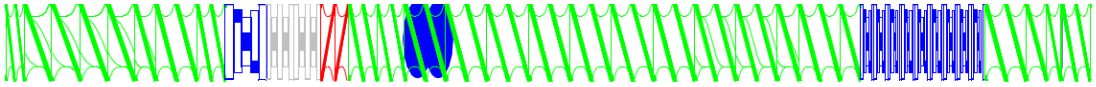

Figure 3.15: Screw 26/(KB45/5/12)

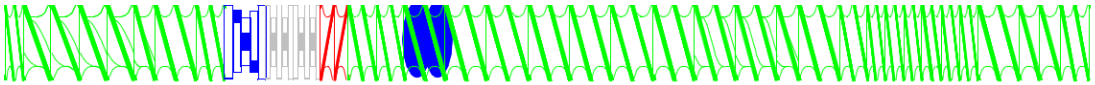

Figure 3.16: Screw 26/(16/16RH)

3.1.2.5 Scale-Up Phase 2 Screw Geometries

Once the experimental drag flow results were analyzed, more accurate percent drag flow scaling factors could be calculated. The new scaling factors were then used for scale-up Phase 2. Along with the scaling factors, there were other parameters that were altered for Phase 2. The bead grade was changed from 158 kPa to 221 kPa, due to inventory constraints. To achieve a reasonable range of percent rupture only the more aggressive wide kneading block mixing section was studied for Phase 2. The percent drag flow scale-up rule was also expanded to examine both the drag flow in the mixing section as well as the upstream conveying element. For all Phase 2 screws the mixing section was kept constant, but two different pitched conveying elements fronted the wide kneading blocks.

The first set of screws, seen below in Figure 3.17 and Figure 3.18, used a square-pitched conveying element to front the aggressive wide kneading block mixing section. The pitch widens directly under the open injection port to mitigate excessive backflow. Note that although the labeling for Screw 18/Wide/16 and Screw 26/Wide/24 are repeated names from Figure 3.9 and Figure 3.11, in Figure 3.17 and Figure 3.18 the 16/16RH and 24/24RH conveying elements extend further than the screw geometries in Figure 3.9 and Figure 3.11, respectively. The additional square-pitched conveying elements helped to isolate the effect of the conveying elements.

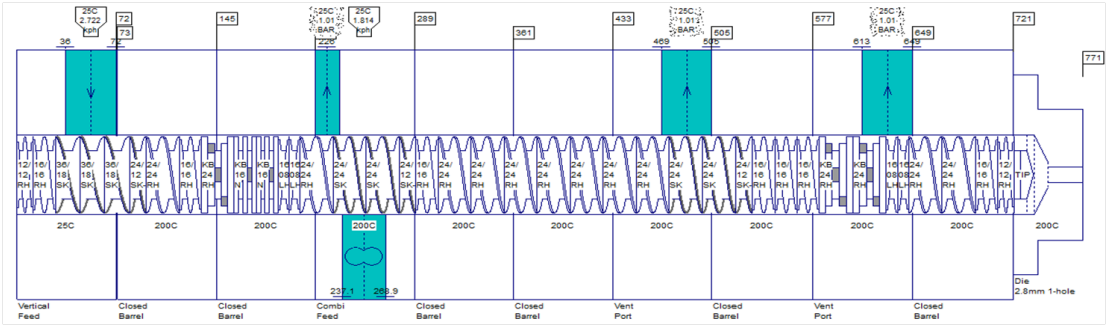

Figure 3.17: Screw 18/Wide/16 (2)

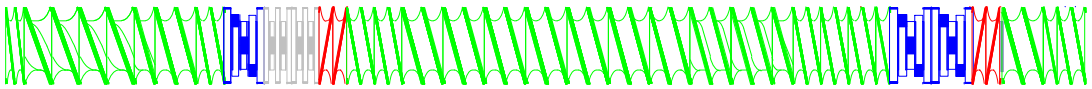

Figure 3.18: Screw 26/Wide/24 (2)

The next set of screws, Screw 18/Wide/12 and Screw 26/Wide/16, are shown below in Figure 3.19 and Figure 3.20. The two screw geometries kept the mixing section constant but used narrow-pitched conveying elements directly upstream.

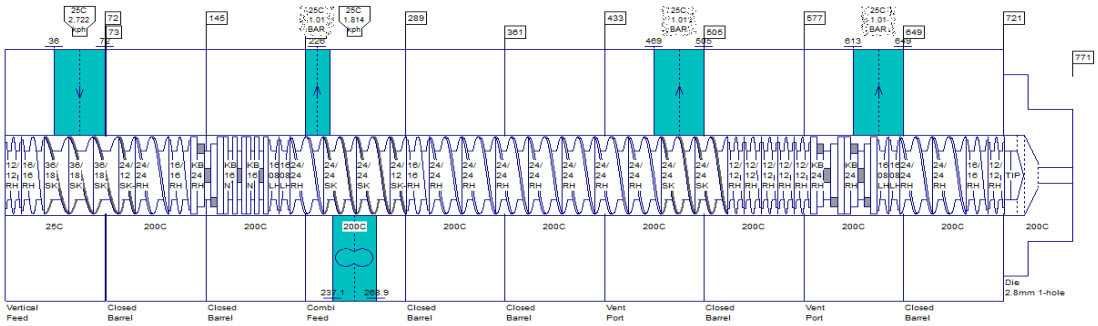

Figure 3.19: Screw 18/Wide/12

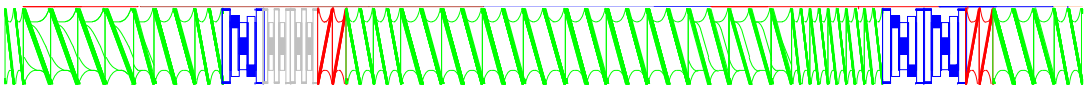

Figure 3.20: Screw 26/Wide/16

3.1.3 Data Acquisition System

In order to collect the RSD and RTD data a National Instruments' LabVIEW 10 program was configured with the following data acquisition system set-up, shown below in Figure 3.21 with all pertinent information labeled.

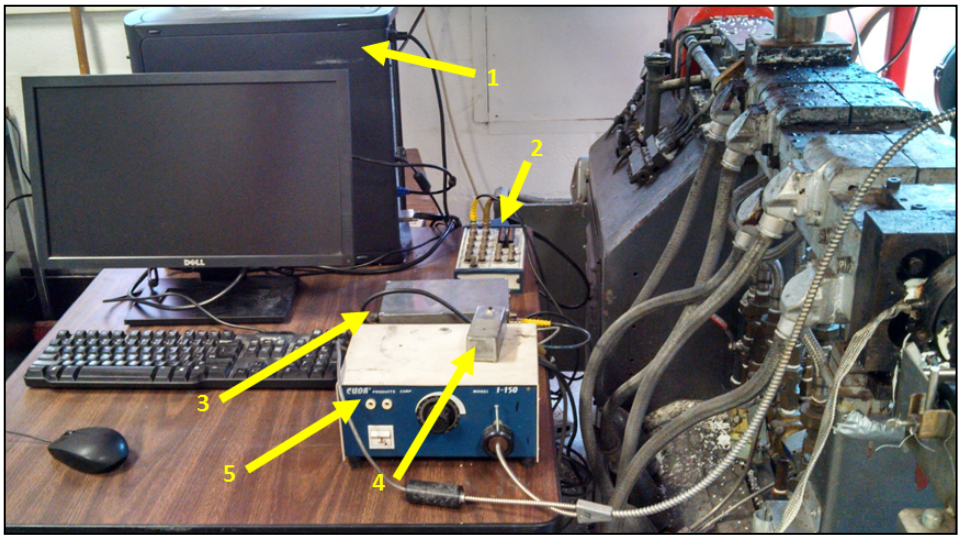

Figure 3.21: Data Acquisition System Set-Up

The data acquisition was comprised of a CPU (1), connector block (2), signal amplifier (3), spike generator (4), and a light source (5) for the reflective optical probe. The extruder can be seen to the left of the data acquisition set-up in Figure 3.21.

The data seen in the "Reflectance" plot in Figure 3.22 below was the unfiltered data. The noise was accounted for through a low pass Butterworth filter with a sampling frequency of 120 Hz. The filtered data can be seen in the "Filtered signal" grid in Figure 3.22, by inspection the data displayed far less noise. Additionally, it was found that a cutoff frequency value of 2 produced the cleanest signal.

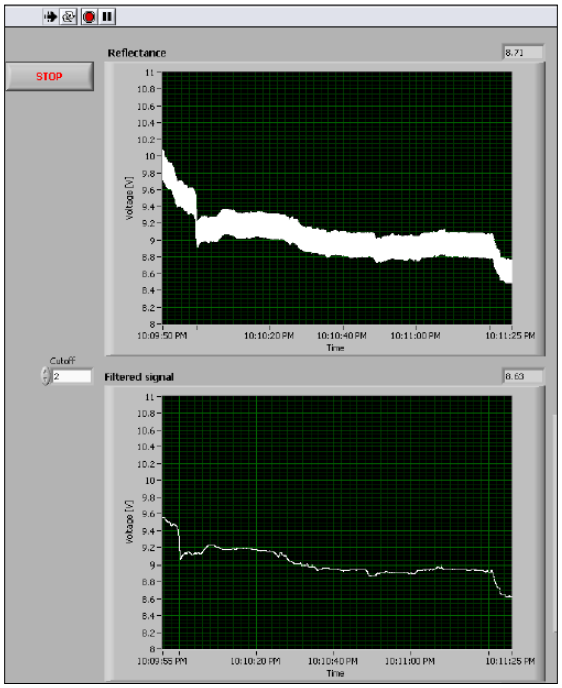

Figure 3.22: Reflectance and Filtered Signal

The data collection began with the Cuda I-150 reflective optical probe that is placed in the block between barrel five and the die zone of the extruder for the 28-mm extruder. However, for the 18-mm and 26-mm extruders, the probe was placed directly after the reverse elements. The probe consisted of a bifurcated optical fiber bundle enclosed in a stainless steel shell contained in a larger stainless steel shell with a sapphire window. The probe was inserted into a barrel through a standard Dynisco pressure transducer port. The probe used a split fiber optic bundle, where white light was transferred from one bundle to the extrusion melt. The light was then scattered by the stained melt and entered back through the other fiber bundle. The light recorded was converted to a voltage signal using a photo diode with a maximum output voltage of 1 V DC. To increase this maximum and add better sensitivity to the system a signal amplifier was used. The signals from the amplifier were then sent to a National Instruments' BNC-2110 connector block that was connected to the CPU. For data

condensing purposes a spike generator was implemented. One of the operators of the experiment would press a button that would spike the data in LabVIEW and erase all previously recorded data, the spike generator was also connected to the connector block. The connector block took all the inputs and converted the signals so the data can be viewed through the LabVIEW interface. When the experiment was completed the data was saved as a spreadsheet, which was used later for further down the line modeling.

3.2 Materials

3.2.1 High Density Polyethylene

The base polymer used for the experiments was High Density Polyethylene (HDPE) grade Alathon H6018. The polymer comes in a translucent pellet from Equistar Chemicals in Houston, Texas. HDPE H6018 is a homopolymer with a medium molecular weight. As the name suggests HDPE H6018 has a high density of 0.960 g/cc. The polymer also has a melt temperature of 104°C and a melt index of 18.0 g/10 min [73]. Figure 3.23 below shows the clear pellets.

Figure 3.23: HDPE Raw Pellets

3.2.2 Calibrated Microencapsulated Sensor Beads

CAlibrated MicroEncapsulated Sensor (CAMES) beads are the means by which the RSD was characterized. MACH I Inc. in King of Prussia, Pennsylvania provided

the beads. A stress distribution can be achieved because the same dye used as the tracer for the RTD was encased in the polymer shell of the CAMES beads. However, the dye will only be released if the beads are loaded to or above their critical stress. The CAMES bead shell polymer is a highly cross-linked polymer known as urea-melamine formaldehyde condensate. CAMES beads came in both red and blue, which then determined the dye they encased. The blue beads encapsulated an AUTOMATE Blue 8A dye and the red beads contained a Red B Disazo dye. The critical stress of a particular CAMES bead is a function of its particle size and wall thickness. A larger bead was easier to break whereas a smaller bead was more robust, and the strength of the bead linearly increased as the thickness of the shell increased. Various grades of CAMES beads were used for this research. Details can be seen below in Table 3.1. CAMES beads will be referred to by their critical stress throughout the rest of this thesis.

Table 3.1: CAMES Beads Table

Critical Stress [kPa]	Bead Diameter [μm]	Wall Thickness [μm]	Color
92	X > 75	1.0	Blue
119	53 < X < 63	0.4	Red
158	45 < X < 75	1.0	Blue
194	X < 45	0.6	Blue
221	32 < X < 45	1.0	Blue

Figure 3.24 (A) and (B) below depicts optical micrographs of the strongest bead, the 221 kPa beads at two different magnifications.

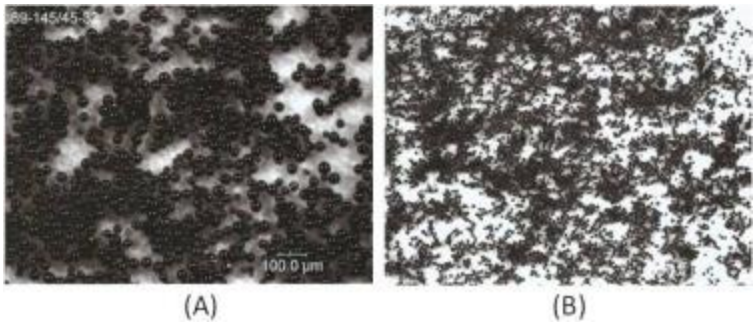

Figure 3.24: Optical Microscopy of the 221 kPa Beads (A) 100µm Scale (B) 1000µm

In Figure 3.25, Scanning Electron Microscopy (SEM) was used to take pictures of two of the 221 kPa beads at a fine enough resolution that the wall thickness could be verified [74].

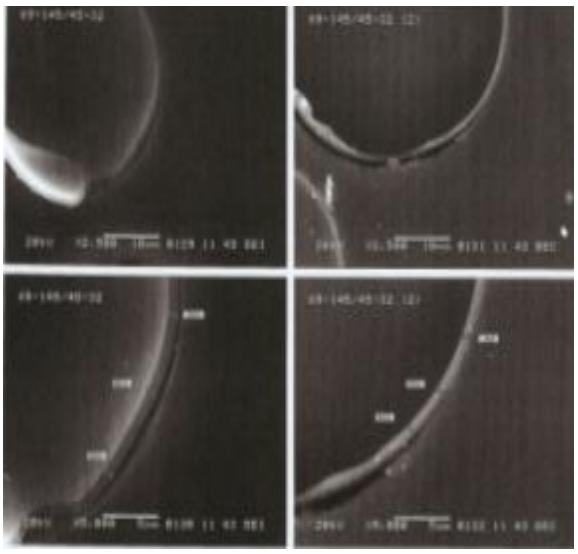

Figure 3.25: SEM Pictures of 221 kPa Beads

3.2.3 Dye

The dye encapsulated within the CAMES beads enable the real time measurement of the RSD. To measure the RTD, only the encapsulated dye is used, which produces a time varying distribution resulting from the non-uniform velocity profile that exists in the screw channels. The RTD is representative of 100% stress bead break-up as long as the volumes were kept constant for both types of shots. Therefore, percent

rupture can be determined by the area underneath the curve generated by the stress bead injection divided by the area underneath the curve created by the dye shot.

The two dyes, AUTOMATE Blue 8A and Red B Disazo, were purchased from Rohm & Haas Co. in Philadelphia, PA. The dye was not directly poured or injected into the open vent port in its liquid state to measure the RTD. To keep the volume of the pure dye tracer and encapsulated dye constant, the pure dye is made into a solid disc. The solid disc was then partitioned into small uniform pieces and weighed. These small solid units are then shot into the HDPE exposed at the open vent port. These injections will be known as dye shots, ink shots, or reference shots throughout the thesis.

Preparation of the ink shots began with 55 mL of Xylene in a beaker. The beaker of Xylene is placed on a hot plate. 6.57 grams of Super High Impact Polystyrene (Super HIPS) is added to the beaker. This is mixed using a magnetic stirrer to catalyze the dissolving of the Super HIPS pellets. Once the pellets are completely dissolved, the solution is poured into a Petri dish and 0.731 mL of dye, either AUTOMATE Blue 8A or Red B Disazo depending on the stress bead color, is injected and mixed until a uniform color is achieved. The solution is then dried underneath a fume hood until the Xylene is fully evaporated, leaving a Super HIPS – Dye solid. This solid is then partitioned. A picture of the partitioned solidified ink shot can be seen in Figure 3.26.

Figure 3.26: Solidified Ink Shot

3.2.4 Titanium Dioxide

To produce an RTD or RSD curve, the polymer must be stained for the light probe to read the color change. To ensure consistent data, or rather a consistent voltage drop from the color change, there needed to be an initial steady state color/voltage. Unfortunately, HDPE is transparent in its melted fluid state. The transparency caused issues for the light probe because it registered the reflectance off the metallic screws. To mitigate this complication Titanium Dioxide (TiO_2) was introduced concurrently into the HDPE system. Ti-Pure grade R-101, supplied by DuPont Titanium Technologies in Wilmington, DE, when melted is an opaque white and was the perfect additive to generate a reference voltage [75]. The opaque white nature minimized the noise caused by the screw's reflectance and provided a large contrast to the red and blue dyes.

Incorporation of the TiO_2 was handled through a two-step procedure. First HDPE and TiO_2 were processed in an extruder at a 95:5 weight ratio of HDPE to TiO_2, to create a mixture of 5% TiO_2 concentrate. The 5% concentrate was then pre-blended with enough neat HDPE to make a half weight percent TiO_2 in HDPE dry pre-blend. Finally, the blend was fed into the hopper awaiting the specified volumetric flow rate. It should be noted that this low weight percent of TiO_2 did not affect the bulk

viscosity of the polymer system. Figure 3.27 below shows a picture of the white TiO_2 pellets.

Figure 3.27: TiO_2 Pellets

3.3 Central Composite Design Grid

Percent break-up was related to the operating conditions of the extrusion process to maximize the utility of the RSD data. Gao et al. found RTDs scale by screw speed (*N*) and specific throughput (*Q/N*). For a rigorous analysis the volumetric flow rate (*Q*) and higher order terms such as *N***N* and (*Q/N*)*(*Q/N*) were also considered.

A DOE approach is commonly employed when investigating multifactor opportunity spaces. Trial and error searches for significant factors are both ineffective and time consuming. The custom design tool in JMP®10.0.0 from SAS® was used to examine the experiment's inputs and variables. The software then determined the best model to evaluate and predict trends for that specified data. The custom tool found that a Central Composite Design (CCD) grid was the best model for analyzing the percent rupture data with respect to operating conditions, screw geometries, and scaling factors. In addition, the CCD grid provided a descriptive illustration of the relationship between percent break-up and operating conditions. An unfilled CCD grid is shown below in Figure 3.28. The x-axis represents displays the range of screw speeds, in rotations per minute (RPM), and the y-axis shows the range of specific throughputs, in milliliters per revolution (mL/rev). The axes in Figure 3.28 show the

resolution (also termed nodes or coordinate values) of the grid. The grid presented below has a β level equal to two, because the coordinates, in both the x- and y-axes extend from -2 to 2. The β nomenclature will be used later to describe modified CCD grids.

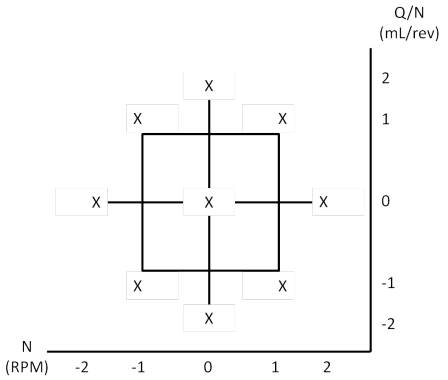

Figure 3.28: Blank CCD Grid with Coordinate Axes

The following sub sections will define all the CCD grids formulated for the body of work completed for this thesis, which are defined using only the operating conditions. The nine coordinate values of each CCD grid will be filled in with mass flow rates, $\dot{M}$, in pounds per hour (lb/hr), instead of the percent break-up data. The percent break-up results can be found in Chapter 5. The CCD grids are grouped with respect to the experiment they were purposed for to best correlate with results in Chapter 5.

There were three stages of experimental research performed for this thesis. Stages one and two focused on validating RSD methodology and establishing the reliability of the technique. The third stage applied the RSD methodology to scale-up, and compared two distinct scale-up rules for dispersive mixing. The scale-up research was decomposed into two phases, named Phase 1 and Phase 2.

3.4 The Effect of Bead Strength

The following study expanded work done by Pappas in his thesis *Characterization and Comparison of Stress History in Various Sized Twin-Screw Extruders Using Residence Stress Distributions* [76]. Pappas established the RSD methodology through experiments run on various 28-mm screw geometries using the 92 kPa and 119 kPa CAMES beads. Two of those screw geometries, Screw 28/Narrow/24 and Screw 28/Wide/24, were mimicked and expanded by running a third bead strength, the 158 kPa grade. The CCD grid was also copied for result congruency. Figure 3.29 below displays the only CCD grid used for the 28-mm CoTSE and the effect of bead strength study.

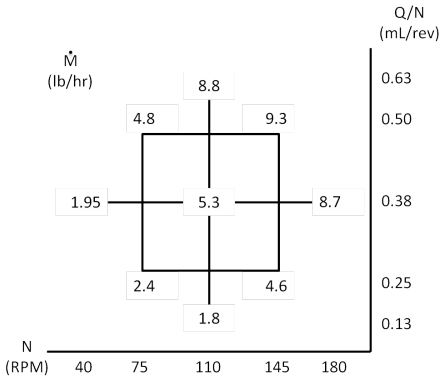

Figure 3.29: 28-mm CCD Grid

3.5 Robust Design of Experiment Approach

Experiments performed on the 28-mm showed how extruders could be characterized with various grades of stress beads. The next stage shows the robustness of the DOE approach used for the RSD methodology through modified CCD grids. Two alterations were used to prove the DOE approach would yield meaningful results for larger domains of operating conditions.

The first grid was selected as a starting point because it duplicated an experiment performed by Pappas. Thus, the operating space was known to be valid. However, this experiment was unique because it used a stronger bead strength, the 158kPa. Figure 3.30 shows the mass flow rates of the grid that was used as the foundation for the modifications; this grid will be called the original CCD grid. The outline of the original CCD grid is grey to show contrast with the adjusted grids, which will be represented in black.

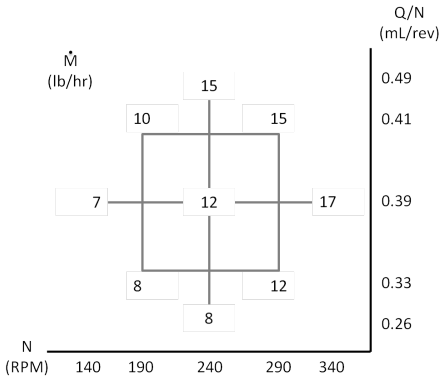

Figure 3.30: 18-mm Original CCD Grid

To show the extent of the DOE approach, a new CCD grid was created for higher screw speeds, shown below in Figure 3.31. The alteration was a simple translation of the CCD grid across the x-axis. The resolution of the x-axis decreased due to extruder motor torque limitations. This brought insight about the quantitative connection between grids in lower and higher shear regimes. This modified CCD grid will be called the increased screw speed CCD grid.

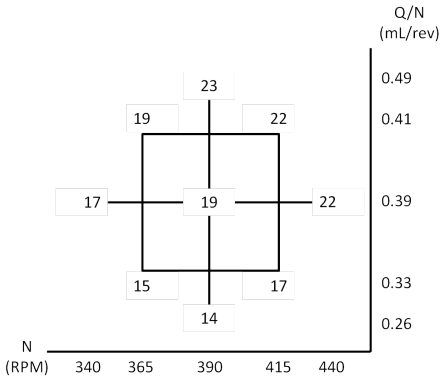

Figure 3.31: 18-mm Increased Screw Speed CCD Grid

The other modification was an expansion along the main cross of the grid or the two lines that bisect the origin of the CCD grid. The expansion along the cross opens up a greater range of degree of fills or specific throughputs. The expanded cross CCD grid is shown below in Figure 3.32.

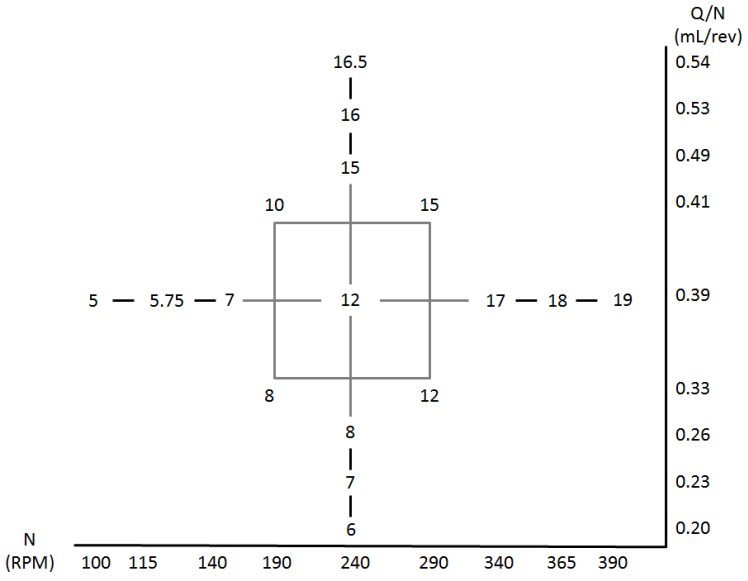

Figure 3.32: 18-mm Expanded Cross CCD Grid

3.6 Dispersive Mixing Scale-Up Study

Validation of the RSD methodology as a robust industrial technique broadened the horizon of its applications. This led to the investigation of a new approach to

scale-up for twin-screw compounding processes with respect to the dispersive mixing behavior, as well as examining an industry standard scale-up rule. Deriving the most consistent scale-up rule required a number of experimental runs. CCD grids used for those experimental runs have been grouped into two phases. However, there were no CCD grids associated to the experimental drag flow test.

3.6.1 Scale-Up Study Phase 1

Phase 1 focused on screw geometries and operating conditions that have already produced sound RSD results. To best reflect industry standards, a CCD grid with high screw speeds was selected. Thus, the CCD grid from Figure 3.31, was used again for the initial scale-up grid on the 18-mm model sized extruder. By using a repeated CCD grid, resources, money, and time were saved because the percent break-up data could be re-used given constant bead strength across the grids (158 kPa). The CCD grid is shown again, and relabeled for this experiment, in Figure 3.33.

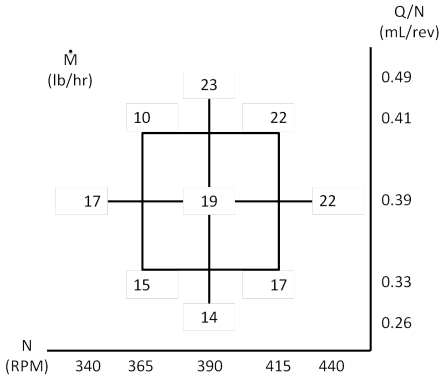

Figure 3.33: Phase 1 18-mm Base CCD Grid

Two scale-up approaches were then used to move the grid into the operating space of the larger 26-mm extruder. The volumetric scale-up rule is considered the industry standard and scales the volumetric flow rate by the cube of the ratio of outer screw

diameters. On the other hand, the newly proposed percent drag flow scale-up rule scales the flow rate by holding the percent drag flow of a specified element constant. For Phase 1, the percent drag flow of the mixing element was kept constant. Every screw bushing has an analogous kneading block element. Because the volumetric scale-up approach is based on single screw extrusion and square-pitched elements, narrow kneading block elements were selected because they are analogous to the square-pitched conveying elements on the experimented CoTSEs. The CCD grids in the 26-mm operating space have the same x-axis (screw speed) as Figure 3.33, again because shear rate scales one-to-one when the *L/D* is constant.

The two scale-up rules produced unique CCD grids. Each CCD grid was investigated using the 26-mm screw geometries for Phase 1, defined earlier. Figure 3.34 shows the CCD grid for the volumetric scale-up. The scaling factor for the volumetric approach was 2.8, which remains constant throughout the study.

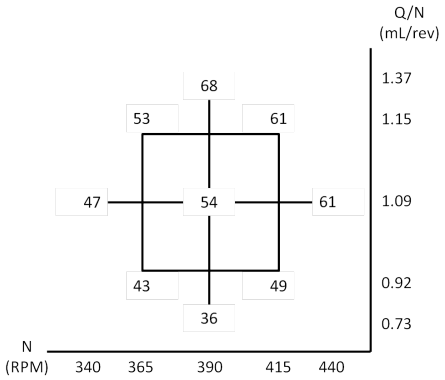

Figure 3.34: Phase 1 26-mm Volumetric Scale-Up CCD Grid

The percent drag flow scale-up rule has slightly lower specific throughput values because the scaling factor was 2.3. Figure 3.35 shows the percent drag flow scale-up CCD grid.

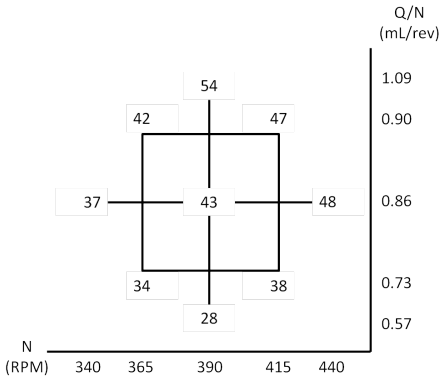

Figure 3.35: Phase 1 26-mm % Drag Flow Scale-Up Grid

3.6.2 Scale-Up Study Phase 2

Phase 2 improved on the scaling factors from Phase 1, using the information from the experimental drag flow tests. The break-up range was also lowered, because the percent break-up data is most sensitive in a range between 30-70%. The bead strength used was 221 kPa, which was the strongest bead grade used throughout the research. Due to the strength of the bead, the narrow kneading block configuration was replaced with a wide kneading block configuration, to more easily rupture the robust beads, seen in Section 3.1.2.5. In addition to screw geometry and bead strength changes, the operating conditions were also altered, due to extruder torque limits. Both the screw speed and throughput were lowered.

Figure 3.36 shows the base 18-mm grid's operating condition. It can be seen that the mass flow rates are the lowest in comparison to all of the previous 18-mm grids.

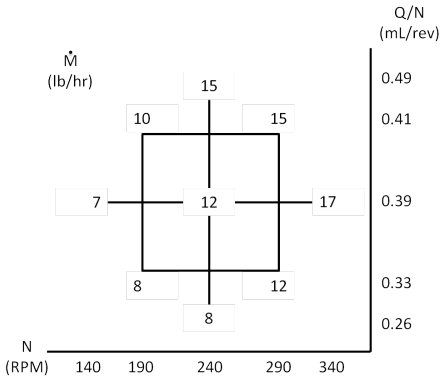

Figure 3.36: Phase 2 18-mm Base CCD Grid

As in Phase 1, the volumetric scale-up approach was of interest to see how the new percent drag flow scale-up rule performed against the industry standard. The volumetric scale-up grid for Phase 2 is shown below in Figure 3.37.

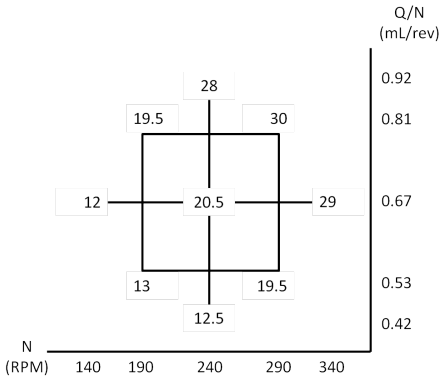

Figure 3.37: Phase 2 26-mm Volumetric Scale-Up CCD Grid

Although the volumetric scaling factor remained the same from Phase 1, all percent drag flow scaling factors were modified because of the experimental drag flow results. Further details on the changes are detailed in Chapter 4. The wide kneading block configuration produced a scaling factor of 3.0. This was greater than the scaling factor of 2.3 previously seen in Phase 1, and even slightly larger than the volumetric scaling factor. It should be noted that if a narrow kneading block mixing section was used the scaling factor would change from 2.3 to 2.6, from Phase 1 to Phase 2,

respectively. The CCD grid for the percent drag flow scale-up rule that kept the percent drag flow of the wide kneading block mixing section can be seen below Figure 3.38. The grid will be called the Mixing %DF CCD grid for convenience, since it is based on the percent drag flow of the mixing section.

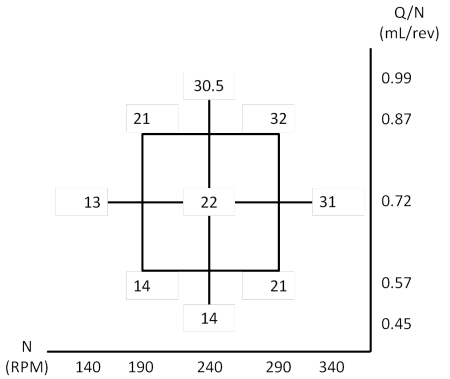

Figure 3.38: Phase 2 26-mm Mixing %DF Scale-Up CCD Grid

The last two CCD grids were based on the percent drag flow of the two different pitched conveying elements fronting the mixing section. Two pitches were investigated in Phase 2, which produced two distinct percent drag flow scaling factors. Figure 3.39 presents the percent drag flow scaled CCD grid for the narrow-pitched conveying elements, followed by Figure 3.40, which displays the percent drag flow scaled CCD grid for the square-pitched conveying element.

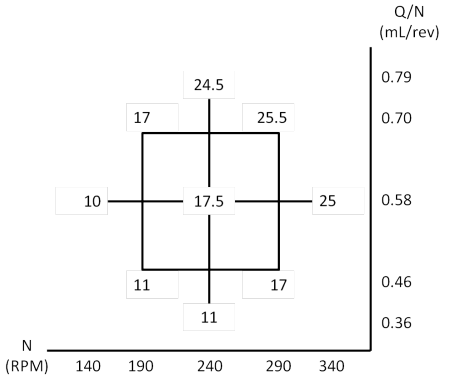

Figure 3.39: Phase 2 26-mm Narrow Conveying %DF Scale-Up CCD Grid

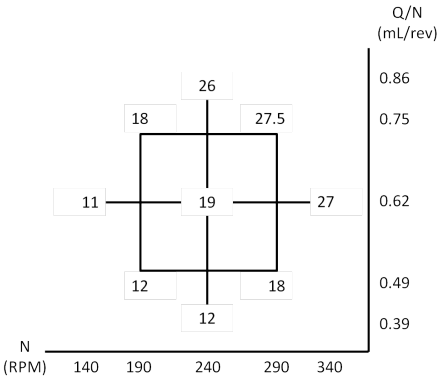

Figure 3.40: Phase 2 26-mm Square-Pitched Conveying %DF Scale-up CCD Grid

The grids are named according to the conveying element examined. Figure 3.39 shows the Narrow Conveying %DF grid, and Figure 3.40 shows the Square-Pitched Conveying %DF grid.

3.7 Residence Stress Distribution Methodology

The following section acts as an instruction manual for the procedure used to collect, measure, analyze, and publish the percent break-up data of the CAMES beads for a completed CCD grid. It should be noted that the following procedure is specifically targeted at performing 28-mm experiments, but the 18-mm and 26-mm experiments also follow this procedure.

3.4.1 Experimental Runs

The first step in this procedure is the collection of the RTD and RSD data, which required injection of the beads and dye into the extruder during operation. Once the FACTS MI – 101 control panel was switched on, a menu screen appeared, displayed below in Figure 3.41.

Figure 3.41: FACTS MI-101 Control Panel Menu

The menu allows the user to set certain operating parameters. First, the five barrels and die zone are turned on. The temperature profile across the barrels was set at a constant 200°C and the die zone set to 190°C. While the extruder reaches the desired temperature profile, prerequisite steps are performed. The blower motor and lubrication pump start are turned on. Furthermore, the interlocks in the cold start menu must be disabled and the emergency stop button must be activated. Completion of these tasks is followed by a color change in the flashing indicator light on the top of the control panel from red to green, signifying that the machine is ready to operate.

When the indicator light turned green the operating conditions could then be set. The screw speed was specified directly on the control panel, and the mass flow rate was set using a K-TRON loss-in-weight feeder. The screws are always turned on first to prevent the piling up of plastic pellets in the feed port, which can potentially over-torque the machine. As the polymer flows into the co-rotating screws, the operator monitors the amperage on the control panel. Amperage above a value of fifteen amps will result in the over-torquing of the extruder motor. Minimal amperage fluctuation indicated that the machine has reached steady state. Exiting extrudate was also observed. Any brown discoloration could be a sign of burnt residual polymer from

previous experimental runs. Once the polymer was observed to flow out steadily with an opaque white hue, experimental runs could begin.

Recording of the experimental runs required setting-up the data acquisition equipment and program. The light source and signal amplifier were switched on, with the light source dial set to the highest sensitivity level. Next, the LabVIEW program was opened on the computer and a cutoff frequency of two was entered. Then a location for the file was selected and the run began.

Once the data collection began operators would wait approximately fifteen seconds for a baseline voltage to be established. After the baseline was established a beaker containing 0.63 grams of the solidified dye was dropped into the open vent port. When the solidified ink was dropped into the vent port, a second lab operator stationed at the computer pressed a button on the spike generator. The spike generator then sent a spike to clear all previously recorded data. Visual confirmation of a successful ink shot could be seen not only on the computer but also as the extrudate physically changed from white to a deep blue. Typically, two ink shots were injected to ensure consistent results. The process was repeated for a CAMES bead shot of 0.51 grams. Stress bead drops are typically repeated three times. The runs were considered complete when the LabVIEW data returned to the baseline voltage and the polymer exiting the extruder was white again.

Figure 3.42 shows the raw reflectance data of a RTD run, a similar shape was found for RSD data as well. The shape of the RTD can be physically explained by the behavior of the flow in the screw channels. The solidified dye melted and stained the

HDPE, this initial staining can be seen by the sharp drop that occurred after the steady baseline.

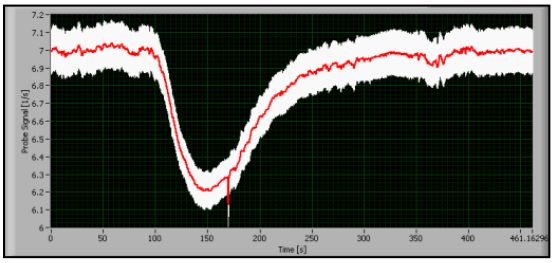

Figure 3.42: Raw Reflectance of RTD

The steep slope of the initial drop was due to the parabolic velocity profile within the screw channel. The stained polymer that exited first traveled through the center of the screw channel, where downstream axial velocity was greatest. Then the return to the baseline, or the tail of the RTD, ascends gradually because of back flow in the kneading block elements, a bi-extensional squishing of the polymer, and the backpressure generated by the reverse elements that backed (directly downstream) the mixing section.

To complete a CCD grid the procedure for the dye and stress bead shots were executed for all nine operating conditions.

3.4.2 Analysis Procedure

3.4.2.1 Percent Break-Up Determination

After a full CCD grid was completed, files in LabVIEW were converted into excel files and analyzed in MATLAB. Data was analyzed by the use of an in house MATLAB code. The complete code for the analysis can be found in Appendix B. The file has six stages for processing raw data. First, the data was passed through a low pass Butterworth filter and flipped about its baseline for a positive area. Processing

required six inputs. The first input was filename, which defined the operating condition and screw geometry depending on the excel file selected. The second was the start cell, which was only necessary because the excel files have a certain number of rows starting at the top of the sheet taken up by character labels automatically generated by LabVIEW. The start cell input allowed the code to skip to the numerical data cells. The next four inputs were dependent on the quality of the data. The third and fourth inputs were two time values that helped better model the RTD and RSD curves. Most RTD and RSD curves have a very smooth drop, due to the steepness and drop rate, but the resurgence back to the baseline (the tail) produced more noise. In order to prevent the noise from affecting the percent rupture of stress beads, the third and fourth inputs cleaned up the unwanted noise. From the two specified time values the function interpolated a slope and extrapolated the remaining data logarithmically, which best fit the curves. For instance, in Figure 3.43 below the red line represents the raw data and the blue line the modeled data.

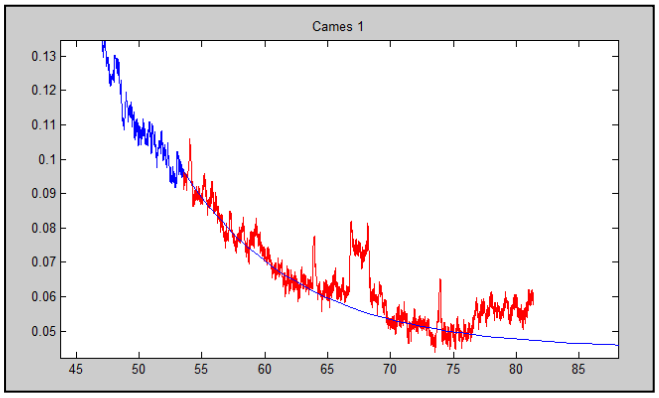

Figure 3.43: Raw (Red) and Modeled (Blue) Subplot Curve

The fifth input was the called the tail length. In the event that the extrapolated modeled data doesn't extend far enough to reach the baseline the tail length can be increased. Finally, the sixth parameter was the baseline cutoff value. Figure 3.44

depicts a subplot with all of the experimental runs for a certain operating condition. The subplot contains the raw data (red) superimposed with the blue data (modeled). Using the data cursor in MATLAB figure tools, any data point could be picked out and defined.

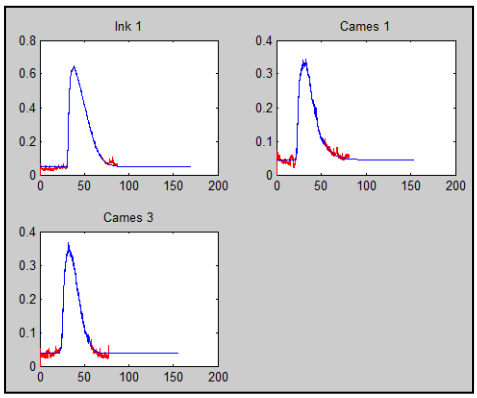

Figure 3.44: Subplot Curves for One Operating Condition

Careful inspection of the subplot shows an exact value for the baseline. To eliminate the noise along the baseline the cutoff parameter took the specified value and drew a straight line across the graph. Elimination of the baseline noise provided a more precise area underneath the curve. Once the analysis was completed the final figure was generated through a separate mfile in MATLAB for each operating condition, found in Appendix B. Figure 3.45 shows an example of a fully analyzed operating condition. With the RTD and RSD curves removed of noise, the percent break-up was calculated. To determine the percent rupture, the area underneath each RSD curve was divided by the area underneath the RTD curve, seen in Equation 3.1.

$$\%Breakup = \frac{A_{RSD}}{A_{RTD}} \cdot 100\% \qquad \textbf{3.1}$$

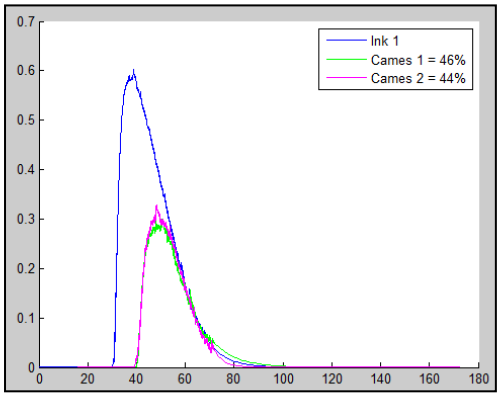

Figure 3.45: Published RTD and RSD Curves

In Figure 3.45 the blue curve was representative of the dye shot, the RTD. The magenta and green curves symbolized the CAMES bead shots, the RSDs. Once the analyzed image was finalized, the average percent break-up of the CAMES bead runs were inserted into its respective position on the CCD grid.

3.4.2.2 Statistical Analysis Procedure

Completion of a set of experimental runs produces an entire CCD grid with all nine coordinate values of stress bead percent break-up values. A finalized CCD grid does not yet provide practical insight into the mixing behavior between compounding processes. However, the DOE approach allowed for an added level of statistical analysis using JMP®10.0.0 from SAS®. The percent break-up values were entered in to a data table like the one seen below in Figure 3.46.

CCD_26mm_Narrow_36_MB_Mixing

CCD_26mm_Narro…
Design Central Composite
Model

	Pattern	N	(Q/N)	Breakup [%]	Conveying Element Pitch	Kneading Block Type	Bead Strength
1	++	1	1	69	16mm	Wide	158kPa
2	00	0	0	62	16mm	Wide	158kPa
3	−+	-1	1	56	16mm	Wide	158kPa
4	−−	-1	-1	53	16mm	Wide	158kPa
5	+−	1	-1	64	16mm	Wide	158kPa
6	0A	0	2	68	16mm	Wide	158kPa
7	0a	0	-2	51	16mm	Wide	158kPa
8	a0	-2	0	55	16mm	Wide	158kPa
9	A0	2	0	70	16mm	Wide	158kPa

Figure 3.46: JMP®10.0.0 Data Table

With the information from any of the RSD experiments entered, three types of statistical analyses were executed.

A Fit Model took the percent break-up data as a role variable and examined the effects of operating conditions, screw geometry, and bead strength depending on the user's selection. The Fit Model then created a statistical report, shown below in Figure 3.47. The sample report studied only the effects of the performance parameters.

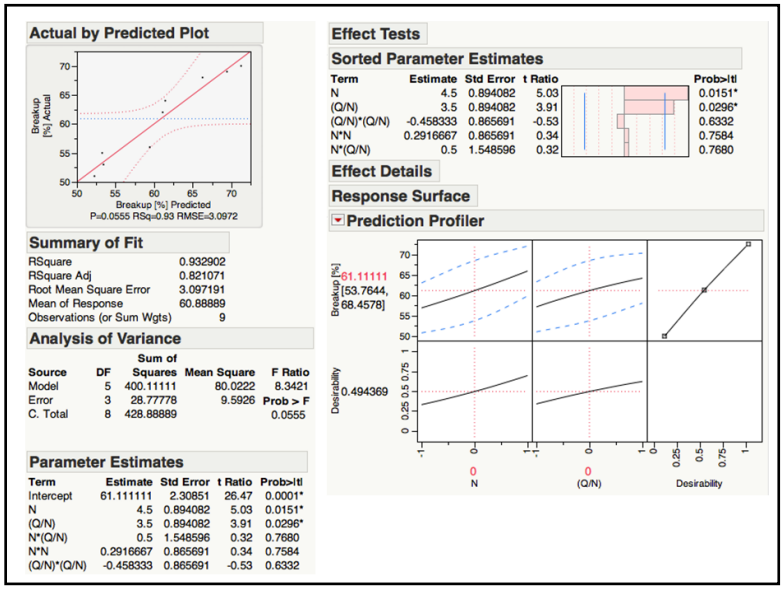

Figure 3.47: Fit Model Report

The Fit Model's report determined the correlation coefficient, an Analysis of Variance, and the Sorted Parameter Estimates. The Sorted Parameter Estimates showed which parameters were statistically significant on a 95% confidence interval. This information will be shown in Chapter 5. As seen in the sample report, for every CCD grid the only two significant parameters regarding operating conditions were screw speed and specific throughput. Once the significant parameters were specified the predictive equation for percent break-up was constructed using the intercept and

the estimate column underneath the Parameter Estimate section in the Fit Model report. The general form of the predictive equation is shown below in Equation 3.2.

$$\%Breakup = C + A \cdot N + B \cdot Q/N \quad \textbf{3.2}$$

C symbolizes the intercept or average. A is the magnitude of the coefficient for screw speed and B is the magnitude of the coefficient for specific throughput. These magnitudes indicate the sensitivity percent break-up had to the specified significant parameters. It should also be noted that the *N* and *Q/N* are not the values the machine was operating at, rather the variables stand for the coordinates on the CCD grid. The center of the grid is at (0,0), for the rest of the coordinates refer back to Figure 3.28. When extra variables such as screw geometry and bead strength were added additional significant parameters appeared. Furthermore, results concerning the reliability of the RSD methodology used the fit model to extract interaction and surface profiles.

For the scale-up study the Fit Model was not sufficient in comparing various scaling factors. Therefore, further statistical analyses were conducted. Fit Y by X analyzes the percent break-up data by scaling factor. The Fit Y by X tool generates an Oneway Analysis shown in Figure 3.48 for a visual difference between the scaling factor results.

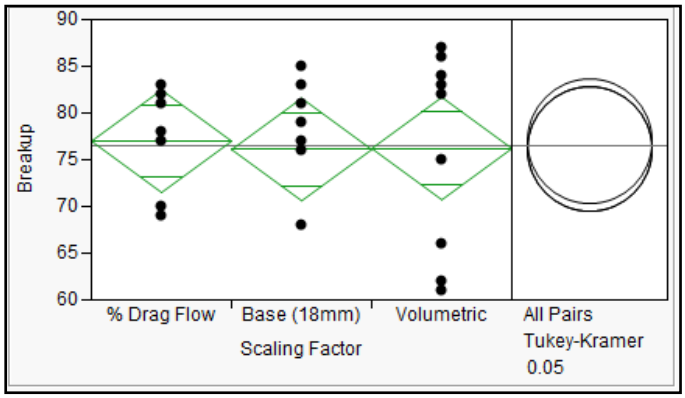

Figure 3.48: Oneway Analysis of Breakup by Scaling Factor

Figure 3.48 provides an excellent visual aid in comparing how percent break-up values, the nine black dots of each scaling factor, were spread with respect to the mean. The green diamonds show the means and quartiles of each scaling factor grid, and then the Tukey-Kramer illustration designated each scaling factor grid with a circle, and the program allowed the user to select a certain circle to compare its mean with the other grids. When the means are statistically different the circles would highlight in different colors. However, since this required selecting the circles, the comparison of means was presented in another manner, through the Connecting Letters Report. Figure 3.49 displays an example Connecting Letters Report. The concept of the Connecting Letters Report was very simple. If two CCD grids have different letters next to their titles, then their means were significantly different. In Figure 3.49, since all CCD grids have an 'A' next to their name the means are not significantly different.

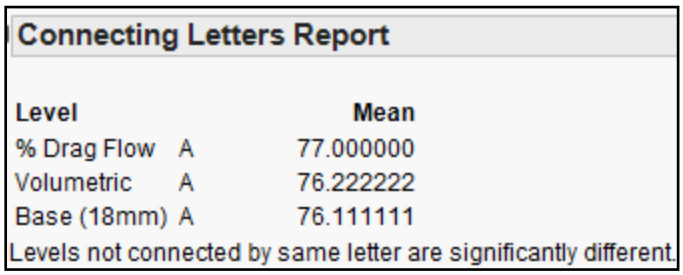

Connecting Letters Report

Level		Mean
% Drag Flow	A	77.000000
Volumetric	A	76.222222
Base (18mm)	A	76.111111

Levels not connected by same letter are significantly different.

Figure 3.49: Connecting Letters Report

Distribution supplements the Fit Y by X analysis in the determination of the most consistent dispersive mixing scale-up approach. Unlike Fit Y by X, Distribution examined each scale-up approach independently and delivered the statistical information seen in the Oneway Analysis visual as numerical values. Figure 3.50 displays the calculated means, quartiles, standard deviation, and more.

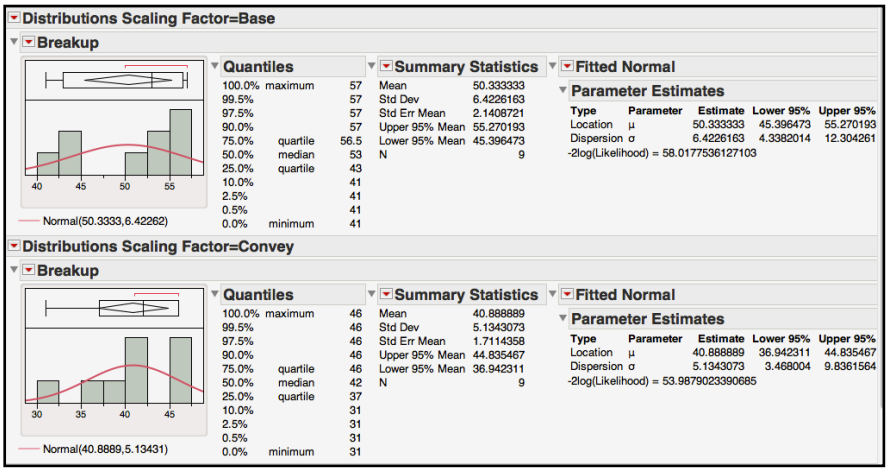

Figure 3.50: Distribution Report

The histograms seen on the left hand side were fit continuously to a normal distribution. A normal distribution was shown because it frequently scored the best in accordance to Aikaike's Information Criterion with correction (AICc). Aikaike's Information Criterion (AIC) determines best fit through an estimate of information lost. The larger the AIC value the more information lost. Yet, for small sample sizes,

such as the nine percent break-up values, the AICc is used. The normal distribution fit then gave approximate values for the mean and spread for each scale-up rule.

With these three types of statistical analyses the data was defined more clearly and presented in a more meaningful manner. Through the predictive equations, the characterization of the RSD can be conducted for any extruder or screw geometry by directly relating the stress history to operating conditions. For the scale-up research, statistical analysis produced a comprehensive story as to which scaling factor kept the stress history (dispersive mixing) the most consistent between the two different sized CoTSE compounding processes.

Chapter 4 Theoretical Calculations

4.1 Industry Scale-Up Calculations

In Section 2.7 the various scale-up rules and perspectives were discussed. However, exploring all scale-up approaches goes far beyond the scope of this thesis. Therefore, only one was selected to act as a datum to compare the newly proposed percent drag flow scale-up rule. The industry standard scale-up rule selected was the volumetric scale-up approach. The volumetric scale-up rule was selected for three reasons: (1) was derived by Carley and McKelvey who found it to scale specific energy consumption, which has been correlated to mixing (2) it scales throughput, which affects residence time, another parameter often tied to mixing effectiveness (3) the approach is purely based on the ratio of screw diameters a constant dimension, which sparked curiosity about how well a constant geometrical scaling factor would perform over the range of operating conditions a CCD grid presents [69][4].

The focus of this study was to investigate the level of dispersive mixing maintained between the model and scaled processes using scale-up rules. This was quantified by the percent break-up of stress-sensitive beads. Section 1.2.1 describes the physics of the correlation between stress and dispersion. Prior RSD research has shown percent break-up to be a function of only screw speed and specific throughput [76]. The following section derives scaling factors for screw speed and specific throughput for the volumetric scale-up approach. It should be noted that the following theoretical calculations are based on single screw extrusion assumptions.

4.1.1 Screw Speed Scale-Up

Mixing performance is related to shear stress, which is a function of screw speed. Therefore, shear rate scales with screw speed, since they are directly proportional. Equation 4.1 below shows the equation for shear rate.

$$\dot{\gamma} = \frac{v_b}{H \cdot 60} \tag{4.1}$$

Where:

$\dot{\gamma}$ = shear rate (1/s)

v_b = barrel wall velocity (m/s)

H = channel height (mm)

The barrel wall velocity can be explained through Figure 4.1 below. The image can be visualized as looking down the channel of a screw element that has been cut on its surface along the screw shaft axis, and then rolled out flat.

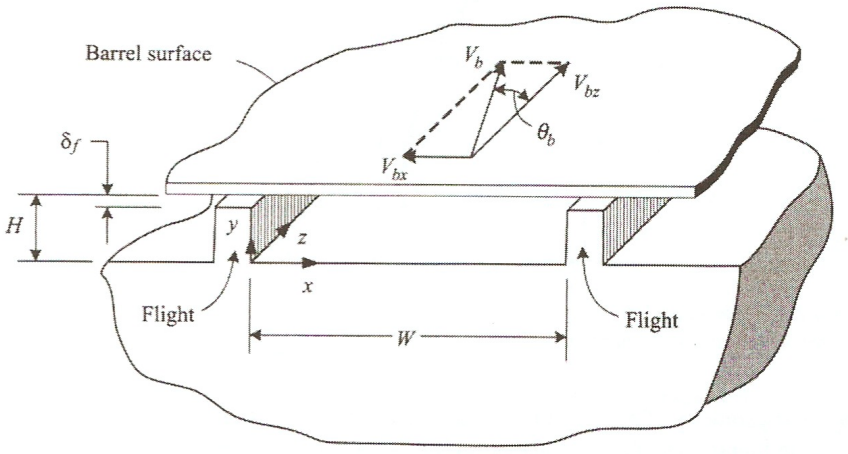

Figure 4.1: Unwound Screw Element with Rectangular Channel [6]

The unwound element against the barrel wall is as an example of an infinite parallel plate problem. The bottom plate is the unwound element, which is kept stationary.

The top plate is the barrel wall, which moves at a constant velocity defined as v_b. The barrel wall velocity is obtained using Equation 4.2 shown below.

$$v_b = \pi DN \quad \textbf{4.2}$$

Where the new variables:

D = outer screw diameter (mm)

N = screw speed (RPM)

Next a relationship between residence time and screw speed is established. This is shown below in Equation 4.3.

$$t = \frac{L}{\pi DN} \quad \textbf{4.3}$$

Where the new variables:

t = residence time

L = length of the screw

Using the geometric similarity theorem, a constant L/D ratio can be assumed between the model and the scaled process. Given that assumption, N is constant for a constant residence time in Equation 4.3. Substitution of a constant N into Equation 4.2 results in a constant shear rate in Equation 4.1. As a result of a constant N, a relationship between channel height and screw diameter is constituted, shown below in Equation 4.4 [4].

$$H \propto D \quad \textbf{4.4}$$

The derivation above explains why the x-axes (screw speed axes) of all the scaled 26-mm grids are identical to the base 18-mm base grids.

4.1.1.1 Shear Stress

Dispersive mixing is grounded in the physics of erosion and rupture of solid agglomerates with internal cohesive force. Screw configurations are designed to achieve some amount of dispersive mixing. Therefore, the calculation of shear stress, which is related to the amount of dispersive mixing achieved, is critical to this research. Shear stress is obtained by Equation 4.5.

$$\tau = \mu\dot{\gamma} = \mu\left(\frac{\pi DN}{60 \cdot H}\right) \quad \textbf{4.5}$$

Where the new variables:

τ = shear stress (Pa)

μ = viscosity (Pa·s)

Knowledge of the screw element geometry for each extruder allows for the determination of the approximate shear stress produced for any arbitrary screw speed. Equation 4.4 established that the channel height will not change for a particular extruder size regardless of the element.

Fluid viscosity is also needed to calculate shear stress. A viscosity profile was obtained using shear history data for HDPE Alathon H6018 provided by DuPont. This is shown below in Figure 4.2.

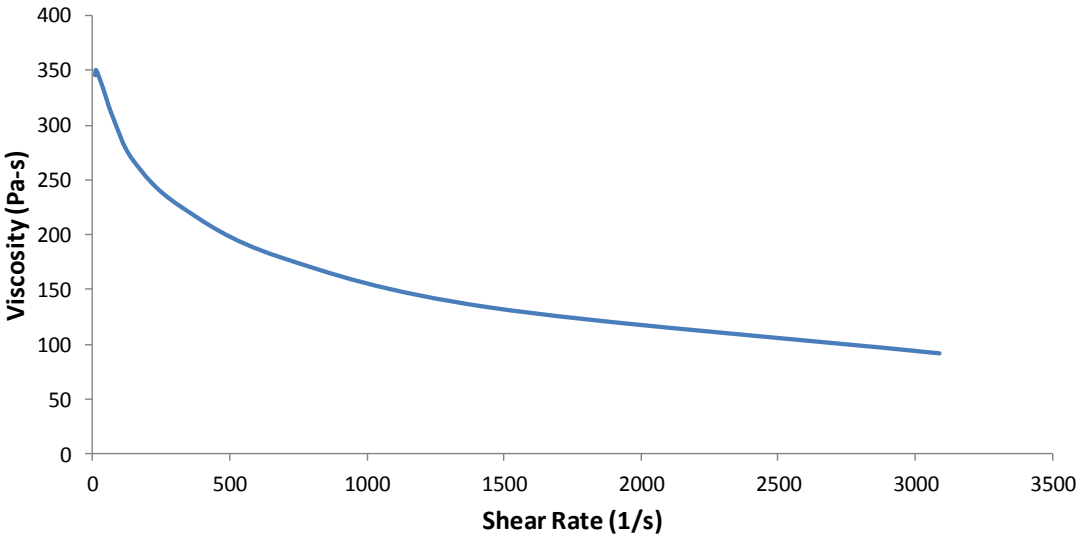

Figure 4.2: Viscosity of HDPE at 200°C for varying shear rates

Table 4.1 displays calculated shear stress values for the five screw speeds used in the stress bead study performed on the 28-mm extruder.

Table 4.1: 28-mm Shear Stress Range

Screw Speed (N) [RPM]	**Shear Rate ($\dot{\gamma}$) [1/s]**	**Viscosity (μ) [Pa·s]**	**Shear Stress (τ) [kPa]**
40	23.5	341.6	9.5
75	44.0	327.5	17.1
110	64.5	312.5	24.0
145	85.0	299.9	30.4
180	105.6	289.0	36.3

The same procedure was followed to for shear stress calculations for each screw speed condition used on the 18-mm and 26-mm extruders. Table 4.2 (below) tabulates the shear stress values for the 18-mm CoTSE. Table 4.3 tabulates the shear stress values for the 26-mm CoTSE.

Table 4.2: 18-mm Shear Stress Range

Screw Speed (N) [RPM]	Shear Rate ($\dot{\gamma}$) [1/s]	Viscosity (μ) [Pa·s]	Shear Stress (τ) [kPa]
100	29.5	337.6	9.9
115	33.9	334.7	11.3
140	41.2	329.5	13.6
190	56.0	318.7	17.8
240	70.7	308.0	21.8
290	85.4	299.7	25.6
340	100.1	291.9	29.2
365	107.5	288.0	31.0
390	114.9	284.1	32.6
415	122.2	280.2	34.2
440	129.6	276.3	35.8

Table 4.3: 26-mm Shear Stress Range

Screw Speed (N) [RPM]	Shear Rate ($\dot{\gamma}$) [1/s]	Viscosity (μ) [Pa·s]	Shear Stress (τ) [kPa]
140	41.9	329.0	13.8
190	56.8	318.1	18.1
240	71.8	307.1	22.1
290	86.8	299.0	25.9
340	101.7	291.1	29.6
365	109.2	287.1	31.4
390	116.7	283.1	33.0
415	124.2	279.2	34.7
440	131.6	275.2	36.2

4.1.2 Specific Throughput Scale-Up

Dispersive mixing is a function of two parameters, screw speed N and specific throughput Q/N. However, in terms of dispersive mixing scale-up, only throughput Q is changing because N remains constant. Nonetheless, specific throughput will be described in this section for greater continuity with the percent drag flow scale-up rule in the following section.

Figure 4.3 below shows the pertinent geometric information for a standard conveying element. This will be used to determine specific throughput.

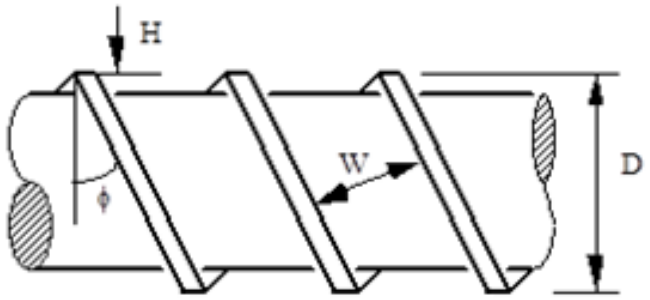

Figure 4.3: Geometrical Characteristics of Screw Element [76]

Where the new variables:

W = channel width (mm)

φ = helical angle (degrees)

A conveying element is used because the following theoretical calculations are based on single screw extrusion (which utilizes only helical screw elements). However, the theory can be extended to TSE kneading block elements because all kneading block elements have a corresponding conveying element.

In order to calculate the net throughput, Q_{Total}, drag flow (Q_{Drag}) and pressure flow ($Q_{Pressure}$) must be calculated. This relationship is shown below in Equation 4.6.

$$Q_{Total} = Q_{Drag} + Q_{Pressure} \quad \textbf{4.6}$$

Q_{Drag} and $Q_{Pressure}$ are determined by Equation 4.7 and Equation 4.8 respectively. These expressions are functions of screw element geometry and operating conditions.

$$Q_{Drag} = \frac{(2\mathrm{n} - 1)}{2} v_{bz} W H F_d \quad \textbf{4.7}$$

$$Q_{Pressure} = \frac{(2n-1)}{12}\frac{WH^3}{\mu}\left(-\frac{\partial P}{\partial z}\right)F_p \quad \textbf{4.8}$$

Where the new variables:

n = number of flights on the element (2 for a bi-lobe and 3 for a tri-lobe)

v_{bz} = down channel component of the barrel velocity (m/s)

μ = polymer viscosity (Pa·s)

($-\partial P/\partial z$) = down channel pressure gradient (Pa/m)

F_d = drag flow shape factor (dimensionless term)

F_p = pressure flow shape factor (dimensionless term)

The term down channel velocity v_{bz} can be expanded further into Equation 4.9.

$$v_{bz} = \pi DN\cos(\varphi) \quad \textbf{4.9}$$

The shape factors, F_d and F_p, are coefficients necessary to correct SSE based assumptions. Each shape factor, related to each throughput term, is assigned a value between zero and one based on *H/W* ratio. Shape factor values must be less than one because the shape factors are correctional coefficients that model the restriction of flow between the infinite plates [6]. SSE elements have a rectangular channel, seen above in the unwound screw diagram in Figure 4.1. However, a TSE does not have rectangular channels. Instead the shape has a certain convexity dependent on its *H/W* ratio. In Figure 4.4, the various down-channel velocity distributions can be seen for varying *H/W* ratios. Where χ = x/W and ξ = y/H. Due to the loss in volume from the parabolic-like shaped channels, throughput potential is lost in comparison to rectangular channels, which dictates the need for the shape factors.

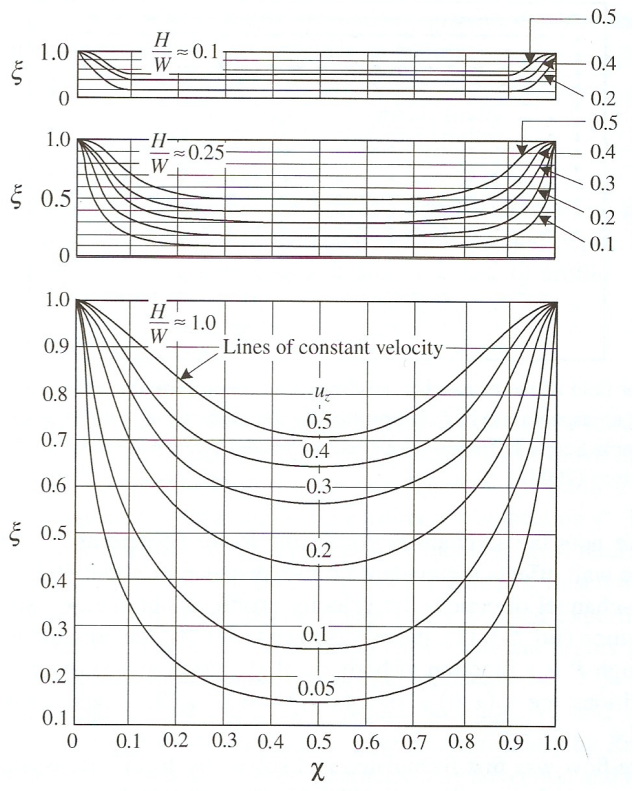

Figure 4.4: Down-Channel Velocity Distribution for Pure Drag Flow for various *H/W* ratios [6]

Figure 4.5 below shows the relationship between *H/W* and the two shape factors. As the *H/W* ratio approaches zero, both the shape factors tend towards unity.

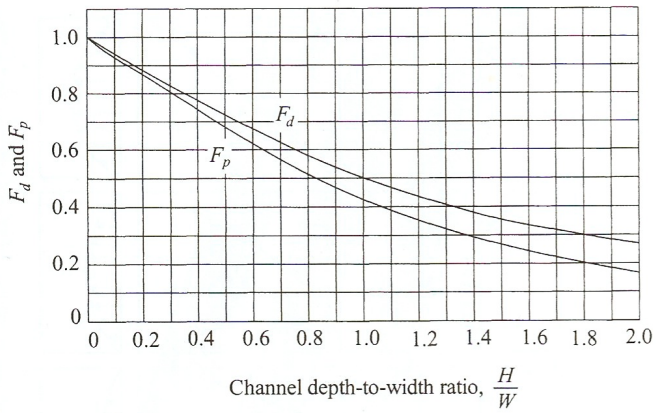

Figure 4.5: Shape Factors vs. *H/W* Ratio[6]

In an extrusion process where either the die zone is removed (creating an open discharge condition), or the screw channels are partially filled, the pressure gradient

term can be neglected. For a twin-screw extrusion process, the throughput reaches an amount that can fully fill the entire screw length. For standard TSE geometries it is common that only the mixing section becomes fully filled, because it is directly upstream from the reverse elements. Subsequently, the $Q_{Pressure}$ term drops because there is no pressure gradient. Substitution of Equation 4.7 and Equation 4.9 into Equation 4.6 produces Equation 4.10 .

$$Q_{total} = Q_{drag} = \frac{(2n-1)}{2}\pi DWHNF_d \cos(\varphi) \quad \textbf{4.10}$$

The definition of total throughput allows for the calculation of 100% specific throughput, $Q/N_{100\%}$. Similar to the principles of drag flow and percent drag flow in Section 2.3, there is a maximum degree of fill that can be actualized by a screw element, which is calculated using Equation 4.11. The 100% specific throughput corresponds to the degree of fill at 100% drag flow.

$$\left(\frac{Q}{N}\right)_{100\%} = \frac{(2n-1)}{2}\pi DWHF_d \cos(\varphi) \quad \textbf{4.11}$$

Equation 4.11 is then used to derive the volumetric scale-up rule. The volumetric approach uses scaled volumetric output as a method for keeping the dispersive mixing equivalent. Therefore, the volumetric scaling factor is equal to the ratio of 100% specific throughput for each extruder. This is shown below in Equation 4.12. Again, by holding screw speed constant, Equation 4.12 can also be seen as the ratio of the throughputs between the two extruders.

$$\frac{\left(\frac{Q}{N}\right)_{100\%\,2}}{\left(\frac{Q}{N}\right)_{100\%\,1}} = \frac{\frac{(2n_2-1)}{2}\pi D_2 W_2 H_2 N F_{d2}\cos(\varphi_2)}{\frac{(2n_1-1)}{2}\pi D_1 W_1 H_1 N F_{d1}\cos(\varphi_1)} = x_{volumetric} \qquad \textbf{4.12}$$

Where the new variables:

$x_{volumetric}$ = volumetric scaling factor

All other variables have been defined earlier without the subscripts 1 and 2 associated with them. The subscript 1 denotes the model sized extruder and the subscript 2 the larger scaled extruder. Specific extruder sizes do not need to be considered yet, because for the volumetric scale-up rule, all but one parameter will cancel. Although shape factors relating SSE theory and TSE theory have already been discussed, it is important to note that this scale-up approach is based on single screw extrusion. Thus, only a square-pitched element is being considered. Both the model and scaled extruder are bi-lobal, which cancels the first term on the left, *n*. Square-pitched elements will have the same helical angle and *H/W* ratio, dropping the φ and F_d terms. Both *N* and π are constant, thus eliminating them from Equation 4.12. The remaining expression after algebraic manipulation is shown below in Equation 4.13.

$$\frac{\left(\frac{Q}{N}\right)_{100\%\,2}}{\left(\frac{Q}{N}\right)_{100\%\,1}} = \frac{D_2 W_2 H_2}{D_1 W_1 H_1} = x_{volumetric} \qquad \textbf{4.13}$$

Further manipulation is possible using the relationship established between the *H* and *D* in Equation 4.4. Additionally, *W* shares the same relationship with *D* as *H* does. The remaining expression is shown below in Equation 4.14.

$$\frac{\left(\frac{Q}{N}\right)_{100\%\ 2}}{\left(\frac{Q}{N}\right)_{100\%\ 1}} = \left(\frac{D_2}{D_1}\right)^3 = x_{volumetric} \quad \textbf{4.14}$$

Now substituting the value for the ratio of the diameters between the 18-mm and 26-mm extruders, the volumetric scaling factor is evaluated in Equation 4.15.

$$\frac{\left(\frac{Q}{N}\right)_{100\%\ 2}}{\left(\frac{Q}{N}\right)_{100\%\ 1}} = 2.8 = x_{volumetric} \quad \textbf{4.15}$$

4.2 Percent Drag Flow Scale-Up Approach

In order to understand the newly proposed percent drag flow scale-up rule, it is critical to know the mathematical definition of percent drag flow. As stated earlier in Section 2.3, every screw element has a maximum pumping potential based on its pitch. Percent drag flow is the fraction of total pumping capacity achieved, which is dependent on the throughput and screw speed at which the extruder is operating at. Along with $Q/N_{100\%}$, the operating specific throughput, $Q/N_{operating}$, is also required to calculate percent drag flow. Operating specific throughput is determined by dividing throughput by the screw speed, at the conditions the extruder is set to. With the two specific throughput terms defined, percent drag flow can be calculated using Equation 4.16 below.

$$\%DF = \frac{\left(\frac{Q}{N}\right)_{operating}}{\left(\frac{Q}{N}\right)_{100\%}} \cdot 100 \quad \textbf{4.16}$$

The volumetric scale-up approach required no knowledge of the operating conditions at which the extruder is performing. Regardless of the *N* and *Q/N*, the volumetric scaling factor for the 18-mm to the 26-mm extruder, will always be 2.8. The percent drag flow rule considers screw element geometry and operating conditions. The derivation of the percent drag flow rule begins with setting the desired percent drag flow of each extruder equal, as shown below in Equation 4.17.

$$\left[\frac{\left(\frac{Q}{N}\right)_{operating}}{\left(\frac{Q}{N}\right)_{100\%}} \cdot 100\right]_{26-mm} = \left[\frac{\left(\frac{Q}{N}\right)_{operating}}{\left(\frac{Q}{N}\right)_{100\%}} \cdot 100\right]_{18-mm} \quad \textbf{4.17}$$

$$= (\%DF)_{desired}$$

The 100% specific throughput is a constant value for a specified element. Thus for each extruder, the $Q/N_{operating}$ can be solved for a desired percent drag flow. The percent drag flow scaling factor is obtained after calculating the necessary $Q/N_{operating}$ values using Equation 4.18.

$$\frac{\left(\frac{Q}{N}\right)_{operating\ 26-mm}}{\left(\frac{Q}{N}\right)_{operating\ 18-mm}} = x_{\%DF} \quad \textbf{4.18}$$

Using the ratio of operating specific throughputs for a specific element ensures the percent drag flow is kept constant between the two processes.

While the volumetric scale-up factor can be exactly determined, the percent drag flow rule is less absolute. Approximations for the drag flow shape factor affect the 100% specific throughput. Though certain elements were repeated in both Phase 1

and Phase 2, the derivation for the shape factor changed, which altered the scaling factor and percent rupture results.

Phase 1 and Phase 2 percent drag flow values are shown in this chapter because they are critical to understanding the flow physics for the base and percent drag flow scaled CCD grids. Percent drag flow values for the bead strength and DOE robustness studies are tabulated in Appendix C.

4.2.1 Percent Drag Flow Phase 1 Scaling Factors

Table 4.4 displays the pertinent element information for scale-up Phase 1. For both the narrow and wide kneading block geometries, the percent drag flow scaling factor was found using a kneading block corresponding to a square-pitched conveying element. For the 18-mm and 26-mm extruders the narrow kneading blocks correspond to the square-pitched conveying elements. Therefore, both geometries produced CCD grids with equivalent y-axes.

Table 4.4: % Drag Flow Scale-Up Approach Phase 1 Data Table

Screw Element	***n***	***D*** **[mm]**	***H*** **[mm]**	***W*** **[mm]**	***φ*** **[°]**	F_d	$(Q/N)_{100\%}$ **[mL/rev]**	***Scaling Factor*** $x_{\%DF}$
18-mm Extruder								
KB45/5/08	2	18.2	3.2	7.7	15.8	0.646	1.32	-
26-mm Extruder								
KB45/5/12	2	25.4	4.55	11.27	16.4	0.52	3.06	2.3

It should be noted that for Phase 1, the shape factor for the 18-mm element was provided by DuPont calculations that could not be disclosed. The 26-mm element shape factor was derived experimentally from prior work [77].

Using the information provided in Table 4.4 the percent drag flow for the operating conditions associated with the base 18-mm and percent drag flow scaled

CCD grids were found. Figure 4.6 and Figure 4.7 show CCD grids already shown in Section 3.6.1, but with percent drag flow axes.

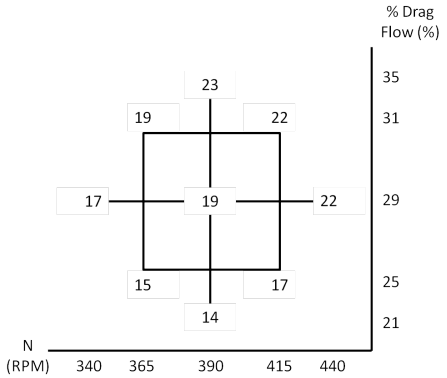

Figure 4.6: Scale-Up Phase 1 18-mm Base Grid with %DF axis

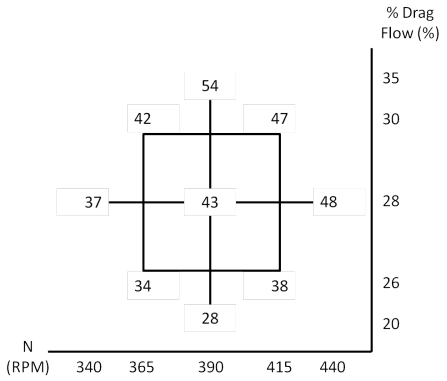

Figure 4.7: Scale-Up Phase 1 26-mm %DF Scaled Grid with %DF axis

Comparison of the percent drag flow axes (y-axes) in the figures above show that the percent drag flow scale-up rule holds constant percent drag flow when moving from the 18-mm extruder to the 26-mm extruder.

4.2.2 Experimental Drag Flow Tests

Phase 2 more precisely derived shape factors introduced earlier using both experimental drag flow data and calculated values. In order to experimentally determine 100% drag flow for a specific element, a unique study must be performed. To measure this drag flow, two pressure probes are placed a short distance apart so

that only the pressure drop across the element type of interest is measured. Unlike standard screw designs used in the RSD experiment, experimental drag flow configurations have no downstream reverse elements. Without those reverse elements, it is possible to fully fill the screw up to the downstream pressure probe, where the section of the measured element ends through increasing flow rate. However, certain elements, for the throughputs required to fill the elements, can induce torque in excess of the extruder's limits. For those elements, experimental drag flow cannot be measured. For narrower-pitched elements, where a lower throughput can fill the screw channels, experimentally measuring the drag flow is feasible.

Once the screw geometry is configured, a constant screw speed is selected and the throughput is incrementally increased. As throughput increases a positive pressure gradient is established. A positive pressure gradient indicates pressure rising in the direction of the polymer flow, or when $Q_{Total} < Q_{Drag}$, since the pressure gradient term from Equation 4.8 has a coefficient equal to negative one. Eventually, the throughput exceeds the feed rate required to fill the screw. At that moment, a negative pressure gradient is generated. A negative pressure gradient exists when $Q_{Total} > Q_{Drag}$. This phenomenon is known as back flow because polymer is being driven against the flow. It should be noted that back flow occurs along z-axis shown earlier in Figure 4.1 in Section 4.1.2, but never in the axial direction, along the screw shaft [6]. For $Q_{Total} > Q_{Drag}$, where $Q_{Pressure}$ is positive and the upstream pressure probe reads greater than the downstream pressure probe, 100% drag flow has been passed. Therefore, 100%

drag flow for a specific element is achieved at the exact moment when the pressure gradient changes from positive to negative.

4.2.2.1 18-mm Experimental Drag Flow Results

Three elements were feasible to study on the 18-mm extruder, the KB45/5/08, 16/16RH, and 12/12RH. All tests performed on the 18-mm had a screw speed of 180 RPM. Table 4.5, Table 4.6, and Table 4.7 display the results for the KB45/5/08, 16/16RH, and 12/12RH elements respectively. The bolded row in each table indicates where 100% drag flow was achieved.

Table 4.5: 18-mm Experimental Drag Flow Test for KB45/5/08 at 180 RPM

Throughput (Q) [lb/hr]	Upstream Pressure [Psi]	Downstream Pressure [Psi]	Torque [%]
15	90	0	~65
14	70	0	~61
13	40	0	~54
12	10-20	0	~47
11	**0-10**	**0**	**~42**
10	10	14.5	~36
9	10	14.5	-

Table 4.6: 18-mm Experimental Drag Flow Test for 16/16RH at 180 RPM

Throughput (Q) [lb/hr]	Upstream Pressure [Psi]	Downstream Pressure [Psi]	Torque [%]
18	0-10	14.5	~69
20	**0-10**	**14.5**	**-**
22	10-20	14.5	-
24	40-50	14.5	Torqued Out

Table 4.7: 18-mm Experimental Drag Flow Test for 12/12RH at 180 RPM

Throughput (Q) [lb/hr]	Upstream Pressure [Psi]	Downstream Pressure [Psi]	Torque [%]
17	50-60	14.5	~66
16	10-20	14.5	~61
15	10	14.5	~58
14	**10**	**14.5**	**~54**
13	0	14.5	~51
12	0	0	~47
10	10	0	~40

4.2.2.2 26-mm Experimental Drag Flow Results

For the 26-mm extruder, two elements were examined the KB45/5/12 and 16/16RH. Table 4.8 and Table 4.9 tabulate the drag flow results for the KB45/5/12 and 16/16RH elements respectively at screw speeds of 90 RPM and 180 RPM respectively. Again, bolded rows indicate 100% drag flow.

Table 4.8: 26-mm Experimental Drag Flow Test for KB45/5/12 at 90 RPM

Throughput (Q) [lb/hr]	Barrel 8 (Upstream) [Psi]	Barrel 9 (Downstream) [Psi]	Torque [%]
27	80	20-30	-
25	40-50	0-10	-
23	10-20	0-10	-
21	**0**	**0**	**-**

Table 4.9: 26-mm Experimental Drag Flow Test for 16/16RH at 180 RPM

Throughput (Q) [lb/hr]	Barrel 8 (Upstream) [Psi]	Barrel 9 (Downstream) [Psi]	Torque [%]
50	10-15	20	-
49	10-13	10	-
48	10	10	-
47	10	0	-
46	9-10	0-10	-
45	**9-10**	**0**	**-**
44	9-10	0	-
41	9-10	0	-

Prior to this study, Chris Polacco of Coperion found the drag flow for a 24/24RH element at 90 RPM to be approximately 36 lb/hr [78].

4.2.2.3 Experimental Drag Flow Analysis

For the 18-mm, the experimental results were compared to calculated values for shape factors provided by DuPont. Comparison showed lower experimental shape factors for experimental 100% specific throughputs. The differences are shown below in Table 4.10.

Table 4.10: 18-mm Shape Factor Comparison

	Experimental Results		DuPont Calculations
Element	**100% Q/N**	**Shape Factor F_d**	**Shape Factor F_d**
KB45/5/08	0.48	0.24	0.65
16/16RH	0.88	0.43	0.59
12/12RH	0.61	0.39	0.52

However, comparison of only the experimental results showed good agreement. While the KB45/5/08 has an analogous pitch to the 16/16RH, the kneading block element had a lower 100% Q/N. This can be explained by throughput losses in kneading block elements resulting from leakage flow through spaces between paddles

and bi-extensional straining. Furthermore, the 12/12RH showed a slightly lower 100% specific throughput when compared to the 16/16RH. This is a result of the narrower pitch.

For the 26-mm extruder, all experimental results aligned well with previously derived experimental shape factors. The drag flow found for the 24/24RH matched the drag flow used based on work performed by Cheng and Bigio [77]. Additionally, the 16/16RH showed a lower drag flow than the wider-pitched 24/24RH.

The experimental drag flow tests dictated the scale-up factors used for scale-up Phase 2. Discussion of Phase 2 is presented in the following section.

4.2.3 Percent Drag Flow Phase 2 Scaling Factors

Experimental results allowed for a more accurate derivation of the various percent drag flow scaling factors needed for Phase 2.

In Phase 1 the square-pitched element percent drag flow rule was used for two different types of mixing sections. Even though the mixing sections were fronted by square-pitched elements, it was critical that in Phase 2 a percent drag flow scale-up rule was calculated specifically for a kneading block element. However, kneading block percent drag flow is more complex, resulting from losses in the flow. Therefore, Phase 2 scaling factors were based off of conveying elements for greater accuracy.

Experimental drag flow results provided a foundation for quantitative measurement and physical explanation of the flow losses related to kneading block design. Leakage flow is heavily dependent on fluid viscoelastic properties, but HDPE is a shear-thinning polymer, which would most likely negate leakage flow losses. To

test the negation of leakage flow, it was hypothesized that, because viscosity remains constant between the two extruders but the physical spaces in the 18-mm kneading block elements are smaller. Therefore, there should be less leakage on the 18-mm than the 26-mm CoTSE. To accept or reject this hypothesis, the percent difference in drag flow between a kneading block element and its corresponding conveying element was calculated on each extruder (based on the experimental data). The results can be seen below in Table 4.11.

Table 4.11: Experimental Leakage Flow Test

Extruder Size [mm]	Element Type	Drag Flow at 180 RPM [lb/hr]	% Drop Relative to Conveying Element
18-mm	KB45/5/08	11	45.0
	16/16RH	20	-
26-mm	KB45/5/12	42	41.7
	24/24RH	72	-

Results show that there is a negligible difference in losses between element pairs for each machine. This rejects the hypothesis that leakage flow was driving the flow losses. Therefore, it was assumed that the flow losses are due to the bi-extensional straining that occurs when the paddles squeeze against the barrel wall and against adjacent paddles.

Phase 2 geometries used only wide kneading block mixing sections. However, the experimental drag flow tests measured narrow kneading blocks and their corresponding conveying elements. Because the losses were quantitatively dominated by the straining motion (which can be seen as a squishing motion), it was assumed that the losses in the wide kneading blocks would, at the minimum, be equal to the losses seen in the narrow kneading blocks. This assumption is geometrically sound

because the ratio of paddle size to kneading block element axial length scales proportionately from the narrow to wide kneading blocks.

The final step prior to calculating all the percent drag flow scaling factors was to select the proper corresponding conveying element for the wide kneading block element. In a kneading block element, if a particle's path line is traced along the channel formed by the staggered paddles the axial length of the element only rotates the particle 180°. For this reason, the pitch can be estimated as double the axial length of a full kneading block element. Matching the pitch between kneading blocks and conveying elements determines likeness. For wide kneading block elements the approximated pitch was so large there was no manufactured conveying element with a similar pitch. To mitigate this issue the *H/W* ratio was linearly extrapolated to create pseudo-conveying elements with pitches equal to the KB45/5/24 on the 18-mm and the KB45/5/36 on the 26-mm. The extrapolation for the 18-mm pseudo-conveying element, 48/48RH, was based on the calculated geometrical aspects and calculated shape factors provided by DuPont. The 26-mm extrapolation was applied to both the experimental drag flow tests and the prior study completed by Cheng and Bigio since both sets of data were equivalent [77].

Table 4.12 below displays the various percent drag flow scaling factors derived for Phase 2 based on the percent drop in drag flow from the extrapolated pseudo-conveying elements, to best model the wide kneading block mixing sections.

Table 4.12: % Drag Flow Scale-Up Approach Phase 2 Data Table

Screw Element	n	D [mm]	H [mm]	W [mm]	φ [°]	F_d	$(Q/N)_{100\%}$ [mL/rev]	$x_{\%DF}$
18-mm Extruder								
12/12RH	2	18.2	3.2	5.87	11.98	0.524	0.825	-
16/16RH	2	18.2	3.2	7.7	15.8	0.593	1.21	-
KB45/5/24	2	18.2	3.2	18.3	40.3	0.49	1.88	-
26-mm Extruder								
16/16RH	2	25.4	4.55	7.77	11.34	0.472	1.96	2.4
24/24RH	2	25.4	4.55	11.27	16.75	0.535	3.14	2.6
KB45/5/36	2	25.4	4.55	26.7	42.07	0.53	5.77	3.0

The scaling factors presented above in Table 4.12 were used to scale the 18-mm base grid according to three different elements. Figure 4.8 shows the 18-mm base grid variations. The three grids all have unique percent drag flow axes corresponding to the (a) narrow-pitched conveying element, (b) square-pitched conveying element, and (c) the wide kneading block element. It is useful to observe the grids from a percent drag flow perspective since they all stemmed from one *Q/N* axis grid.

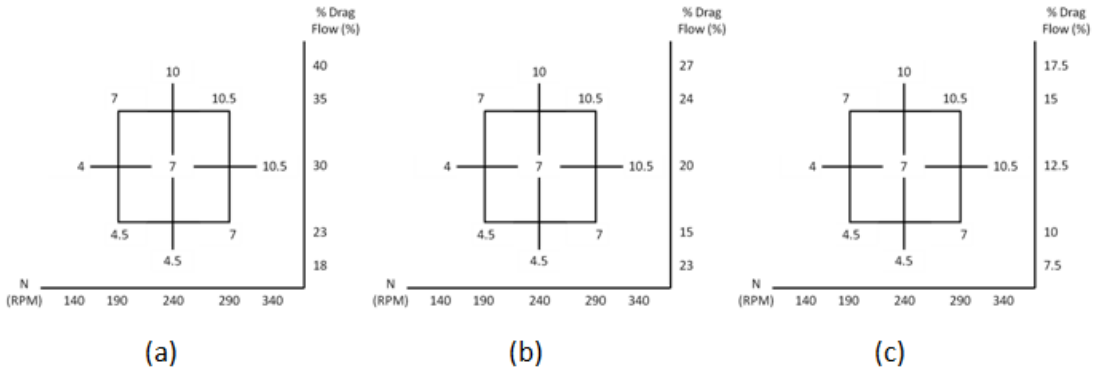

Figure 4.8: Scale-Up Phase 2 18-mm Base Grids with %DF axis corresponding to (a) 12/12RH (b) 16/16RH (c) KB45/5/24

Each 18-mm base grid above was scaled-up with the scaling factors based on geometrically similar 26-mm elements, listed in Table 4.12. Figure 4.9 displays the 26-mm scaled grids with a percent drag flow axis corresponding to (a) narrow-pitched conveying element, (b) square-pitched conveying element, and (c) wide kneading block element.

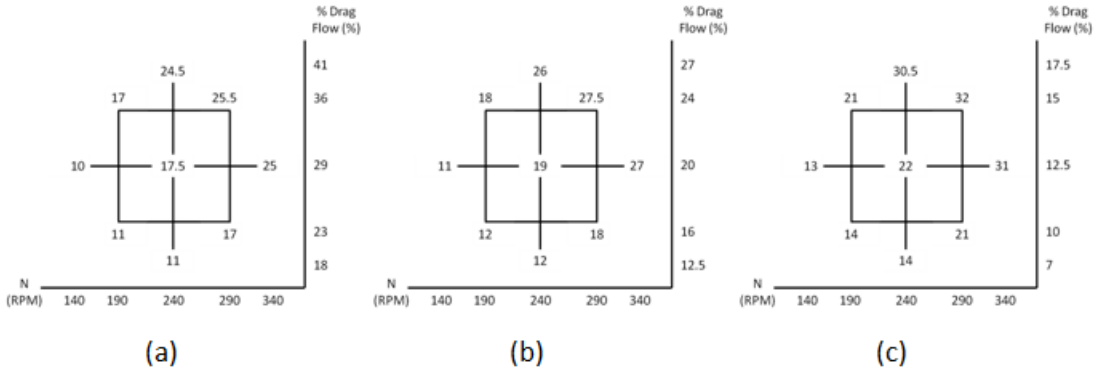

Figure 4.9: Scale-Up Phase 2 18-mm Base Grids with %DF axis corresponding to (a) 16/16RH (b) 24/24RH (c) KB45/5/36

The results in Figure 4.9 display successful percent drag flow scaling factors because the axes are nearly identical to the axes displayed in Figure 4.8.

4.3 CAMES Beads Stress Calculations

In order to relate the percent rupture results found for the various CCD grids to magnitudes of shear stress it is necessary to accurately characterize the failure stress of the beads. The stress associated with each bead was calibrated using a capillary flow rheometer. MACH I Inc. determined percent rupture results for shear stresses at the wall of the tube. However, it is known that the stress and velocity distribution for laminar flow through a pipe is non-uniform. The shear stress will increase as it approaches the boundary condition at the wall. Thus, a new model had to be

formulated to more accurately estimate the stress responsible for breaking a particular bead strength [79].

The model is based on the flow of a highly viscous polymer moving through a small orifice. The flow inside the tube exhibits high viscous forces and low inertial forces producing a low Reynolds number or creeping flow. A diagram of the capillary tube depicting the velocity and stress distribution is shown below in Figure 4.10.

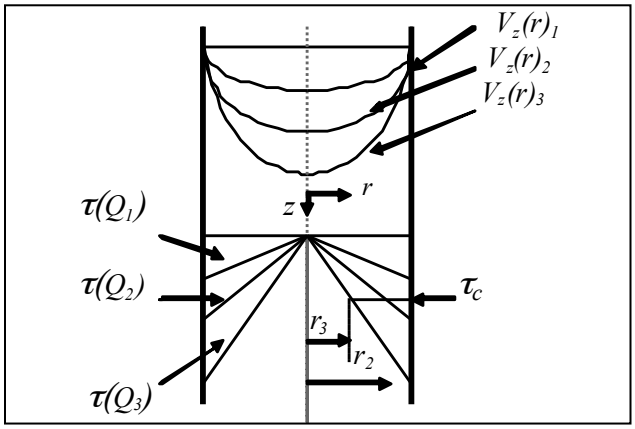

Figure 4.10: Sketch of Flow Field and Stress Distribution [79]

Bead movement in the radial direction was ignored. It was assumed the beads would travel along their vertical streamlines. Additionally, it was assumed that the beads would only rupture for stresses greater than or equal to a critical shear stress, τ_c. Thus, for a given flow rate the percentage of beads that pass through the critical stress regions can be calculated based on the behavior of creeping flow and the Navier-Stokes Equation.

The equation of motion can be described as the z-component of the Navier-Stokes Equation in cylindrical coordinates, shown below in Equation 4.19.

$$\rho\left(\frac{\partial u_z}{\partial t}+u_r\frac{\partial u_z}{\partial r}+\frac{u_\varphi}{r}\frac{\partial u_z}{\partial \varphi}+u_z\frac{\partial u_z}{\partial z}\right)$$
$$=-\frac{\partial P}{\partial z}+\mu\left[\frac{1}{r}\frac{\partial}{\partial r}\left(r\frac{\partial u_z}{\partial r}\right)+\frac{1}{r^2}\frac{\partial^2 u_z}{\partial \varphi^2}+\frac{\partial^2 u_z}{\partial z^2}\right]+\rho g_z \quad \textbf{4.19}$$

For laminar flow Equation 4.19 can be reduced to Equation 4.20.

$$\frac{1}{r}\frac{d}{dr}(r\tau_{zr})+\frac{dP}{dz}=0 \quad \textbf{4.20}$$

Then the stress distribution, described in Equation 4.21, can be found by applying the boundary condition $\tau_{zr}=0$ at $r=0$ to Equation 4.20.

$$\tau_{zr}=\left(\frac{\Delta P}{L}\right)r \quad \textbf{4.21}$$

The visual representation of the stress distribution can be seen above in Figure 4.10 denoted by $\tau(Q_i)$. Inspection of Equation 4.21 shows the stress distribution to be a function of the pressure differential and radial position. Given that the percent rupture is known for a given shear stress at the wall the beads had to break in a region between R-r_c. Therefore, by evaluating cross-sectional areas for regions that experience shear stresses greater than τ_c, the percent break-up of beads can be found as a function of flow rate.

Determination of the flow rate for those specified regions requires defining the velocity distribution for a Newtonian fluid, seen below in Equation 4.22.

$$V_z = \left(\frac{\Delta P R^2}{4\mu L}\right)\left[1 - \left(\frac{r}{R}\right)^2\right] \quad \textbf{4.22}$$

The flow rate is obtained in Equation 4.23, by integrating between the radius of the tube, *R*, and the radial distance where $\tau_{zr} = \tau_c$, r_c. The bounds of integration correspond to the stress regions that experience stresses greater than the critical shear stress.

$$Q_c = \int_0^{2\pi} \int_{r_c}^{R} V_z r dr d\theta \quad \textbf{4.23}$$

To find the fraction of beads broken the flow rate for the high stress regions is divided by the total flow rate. The total flow rate is defined below.

$$Q_T = \int_0^{2\pi} \int_0^{R} V_z r dr d\theta \quad \textbf{4.24}$$

The formal expanded equation for percent break-up of stress beads is displayed in Equation 4.25.

$$Percent\ Break - up = \frac{Q_c}{Q_T} = \left[\left(\frac{r_c}{R}\right)^2 - 1\right]^2 \quad \textbf{4.25}$$

However, the model needs to solve for the critical shear stress, so Equation 4.25 must be reformatted to solve for the radial distance that relates to the critical shear stress. Equation 4.26 shows the resultant rearranged equation that solves for r_c.

$$r_c = R\sqrt{1 + \sqrt{Percent\ Break - up}} \quad \textbf{4.26}$$

Substituting Equation 4.25 into Equation 4.21 creates a relationship between the critical and wall shear stresses, displayed below in Equation 4.27.

$$\sqrt{Percent\ Break-up} = 1 - \left(\frac{\tau_c}{\tau_w}\right)^2 \quad \textbf{4.27}$$

Solving Equation 4.27 for the critical stress produces an equation that is dependent on the two quantities provided by MACH I Inc., as seen in Equation 4.28.

$$\tau_c = \tau_w \sqrt{1 - \sqrt{Percent\ Break-up}} \quad \textbf{4.28}$$

With Equation 4.28 the critical stress can be calculated for the various grades of stress beads. Yet, the percent rupture data determined by MACH I Inc. was only evaluated at 10% and 90% rupture, thus interpolation was required to find the intermediary wall shear stresses. The critical stress level that has been used to name the various bead strengths was determined by the average of each critical stress found from 10% to 90% rupture with a resolution of 10%. Table 4.13 below displays the critical stress for all of the different sized beads.

Table 4.13: Critical Stress Levels for Various Bead Strengths

Bead Diameter [µm]	**Wall Thickness [µm]**	**τ_w for 10% rupture [kPa]**	**τ_w for 90% rupture [kPa]**	**Calculated τ_c [kPa]**
X > 90	0.4	175	290	119
X > 75	1.0	120	250	92
45 < X < 75	1.0	190	450	158
X < 45	0.6	242	408	194
32 < X < 45	1.0	230	489	221

4.4 Elongational Stress Calculations

In addition to shear stresses, elongational stresses are generated in the polymer flow. Elongational (Extensional) stresses are caused by the squeezing that occurs between kneading blocks and the barrel wall and the squeezing between the kneading blocks of one screw and the kneading blocks of the adjacent screw. Observation of the shear stress results shown in Table 4.1, Table 4.2, and Table 4.3 (in Section 4.1.1.1) for the 28-mm, 18-mm, and 26-mm, respectively, shows that the shear stresses are not nearly strong enough to break any of the bead strengths. The maximum shear stress, for each extruder, never exceeds 36 kPa, but the weakest bead strength is 92 kPa. Therefore, there must be another stress dominating the rupture of the stress beads, namely elongational stress. To estimate elongational stress imparted on the polymer, the parallel plate problem was considered shown below Figure 4.1. However, for this approximation the top plate movement occurs in the z-axis, and again the bottom plate is fixed, an illustration is provided below in Figure 4.11.

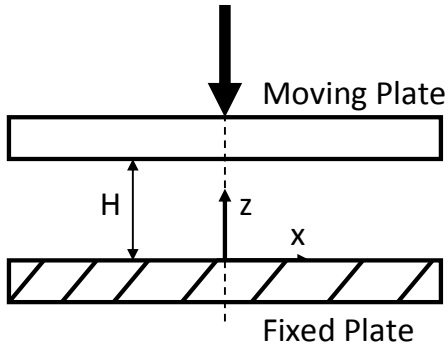

Figure 4.11: Flow Between Two Parallel Squeezing Plates

As the top plate lowers, the polymer experiences a bi-extensional strain, where polymer is forced out in both directions. Derivation of the elongational stress begins with the vorticity equation provided below.

$$\frac{D\vec{\omega}}{Dt} = \left(\vec{\omega}\cdot\vec{\nabla}\right)\vec{\mathrm{V}} - \vec{\omega}\left(\vec{\nabla}\cdot\vec{\mathrm{V}}\right) + \frac{1}{\rho^2}\vec{\nabla}\rho\times\vec{\nabla}\mathrm{P} + \vec{\nabla}\times\left(\frac{\vec{\nabla}\cdot\underline{\underline{\tau}}}{\rho}\right) + \vec{\nabla}\times\vec{\mathrm{B}} \qquad \textbf{4.29}$$

Where:

$\vec{\omega}$ = vorticity

$\vec{\mathrm{V}}$ = velocity vector

ρ = density

P = pressure

$\underline{\underline{\tau}}$ = viscous stress tensor

$\vec{\mathrm{B}}$ = body force term

The vorticity, $\vec{\omega}$, can also be defined by the double gradient, or Laplacian, of the stream function ψ, shown below in Equation 4.30 also known as Poisson's Equation.

$$\nabla^2\psi = -\omega \qquad \textbf{4.30}$$

Substituting Equation 4.30 into Equation 4.29 and solving for the stream function yields Equation 4.31 below. A common solution solved in various fluid mechanics textbooks, which has the following non-dimensional relationship.

$$\psi^* = x\left(\frac{3z^{*2}}{\xi^{*2}} - \frac{2z^{*3}}{\xi^{*3}}\right) \qquad \textbf{4.31}$$

The dimensionless terms (denoted with a superscript asterisk) are defined below.

$$\psi^* = \frac{\psi}{VL} \qquad \textbf{4.32}$$

$$x^* = \frac{x}{L} \tag{4.33}$$

$$z^* = \frac{z}{H_o} \tag{4.34}$$

$$\xi^* = \frac{H}{H_o} \tag{4.35}$$

Where:

V = velocity of the moving plate

L = length of the plate

z = distance between the plates

H_o = initial height between the plates

H = final height between the plates

The stream function is newly defined by Equation 4.36 through the substitution of the dimensionless terms into Equation 4.31.

$$\psi = Vx\left(3\left(\frac{z}{H}\right)^2 - 2\left(\frac{z}{H}\right)^3\right) \tag{4.36}$$

Using Equation 4.36, the horizontal velocity component can be evaluated, and is shown below in Equation 4.37.

$$u = \frac{\partial \psi}{\partial z} = Vx\left(6\frac{z}{H^2} - 6\frac{z^2}{H^3}\right) \tag{4.37}$$

To derive the extensional shear rate $\left(\frac{\partial u}{\partial x}\right)$, an integral component in calculating the elongational stress, the partial derivative with respect to x must be applied to Equation 4.37. The extensional shear rate equation is shown below.

$$\frac{\partial u}{\partial x} = \frac{6V}{H^2}\left(z - \frac{z^2}{H}\right) \quad \textbf{4.38}$$

To properly apply this to a TSE some terms must be added to Equation 4.38. Kneading block sizes vary, which requires the extensional shear rate to be a function of width of the block (*w*). In order to keep the equation dimensionless an additional height is divided to account for the newly added width term. Furthermore, throughput is significant in altering the extensional shear rate. Thus, an additional throughput term (*Q*), has been added to the equation. Through these modifications the updated equation for extensional shear rate is provided below.

$$\frac{\partial u}{\partial x} = \frac{6Vw}{H^3}\int_{z_o}^{z_f}\left(z - \frac{z^2}{H}\right)dz + \frac{Q}{HwL} \quad \textbf{4.39}$$

Similar to shear stress, the elongational stress can be calculated by multiplying the extensional shear rate by the extensional viscosity. The extensional viscosity is shown below in Equation 4.40.

$$\mu_e = 3\mu \quad \textbf{4.40}$$

With the extensional viscosity defined, the elongational shear stress can be determined using Equation 4.41 below.

$$\tau_e = \mu_e \frac{\partial u}{\partial x} \quad \textbf{4.41}$$

Table 4.14 provides the necessary geometrical information from the various kneading block sizes for each extruder. Using the geometrical information provided in Table 4.14 the elongational stress can be calculated.

Table 4.14: Kneading Block Geometry Information

Extruder Size/ Kneading Block (KB) Size	Kneading Block Width (w) [mm]	Length of the Plate (L) [mm]	Initial Height (H_o) [mm]	Final Height (H) [mm]	Initial Distance between Plates (z_o) [mm]	Final Distance between Plates (z_f) [mm]
28-mm Narrow KB	2.5	12.1	4.5	1	4.5	1
28-mm Wide KB	8	12.1	4.5	1	4.5	1
18-mm Narrow KB45/5/08	1.6	9.9	5	1	5	1
18-mm Wide KB45/5/24	4.8	9.9	5	1	5	1
26-mm Narrow KB45/5/12	2.4	14.3	5	1	5	1
26-mm Wide KB45/5/36	7.2	14.3	5	1	5	1

The elongational stress is determined for the CCD operating conditions for the 28-mm in Table 4.15. The elongational stresses for the operating conditions used on the 18-mm and 26-mm extruders are tabulated (by experiment) in Appendix D, due to the large domains studied on the 18-mm and 26-mm.

Table 4.15: Elongational Stress for 28-mm TSE

Operating Condition (Q)/(N) [lb/hr]/[RPM]	28-mm Narrow Kneading Block [kPa]	28-mm Wide Kneading Block [kPa]
1.95/40	27.1	61.6
2.4/75	43.3	109.1
4.8/75	53.6	112.3
1.8/110	53.6	150.5
5.3/110	67.9	154.9
8.8/110	82.1	159.4
4.6/145	76.5	193.1
9.3/145	94.9	198.8
8.7/180	102.8	234.5

Table 4.15 and the extensional stress tables in Appendix D show a greater stress magnitude than the shear stress. Thus, the extensional stress clearly dominates the rupturing of the stress beads.

Chapter 5 Results

The following chapter presents all of the results necessary to make an impactful contribution to the plastic processing industry. The chapter is presented in four parts. The first two parts were purposed to verify the validity of the RSD methodology, and the second two parts present the findings that prove the newly proposed percent drag flow scale-up rule is the most reliable approach to scaling dispersive mixing behavior. The results show that the percent drag flow scale-up rule outperforms the volumetric scale-up rule over the range of operating conditions defined by the CCD grid.

The investigation into dispersive mixing scale-up in twin-screw compounding required an accurate and reliable measurement technique. In order to prove the consistency of the RSD methodology, two studies were pursued. First the effect of the bead strength was studied on the 28-mm extruder. Next, the DOE approach was expanded to explore experimental trends at a deeper level. From that foundation the methodology could then be relied upon to provide valuable insight into the scale-up issue in twin-screw compounding. The scale-up study is broken down into two parts, called Phase 1 and Phase 2, which built on each other to fully develop the dispersive mixing scale-up story.

5.1 The Effect of Bead Strength

There were two goals of the bead strength study. First, show that multiple bead strengths would produce consistent results. Second, discover what new conclusions could be determined by implementing a range of bead strengths on one extruder.

Two different screw geometries were used for this study, Screw 28/Wide/24 and Screw 28/Narrow/24. It was important to have two screw designs to see how the relationship between screw geometry and percent rupture would change. Only one CCD grid was used, seen earlier in Figure 3.29, since the nine operating conditions embedded in the grid would provide a sufficient amount of data points. Three different bead strengths were studied on the tri-lobal 28-mm CoTSE: 92 kPa, 119 kPa, and the 158 kPa CAMES beads. It should be noted that the 92 kPa and 119 kPa bead strength experiments were performed by Pappas, and then extended with the addition of the 158 kPa grade beads in this study [76].

5.1.1 Percent Break-Up CCD Grids

The CCD grids presented below show the percent rupture results for all bead strengths on both geometries. Figure 5.1 shows the results for the weakest bead grade, the 92 kPa beads, for both screw geometries. The left grid corresponds to the distributive mixing screw geometry comprised of narrow kneading block elements, Screw 28/Narrow/24. The right grid corresponds to the more aggressive dispersive mixing screw geometry composed of wide kneading blocks, Screw 28/Wide/24.

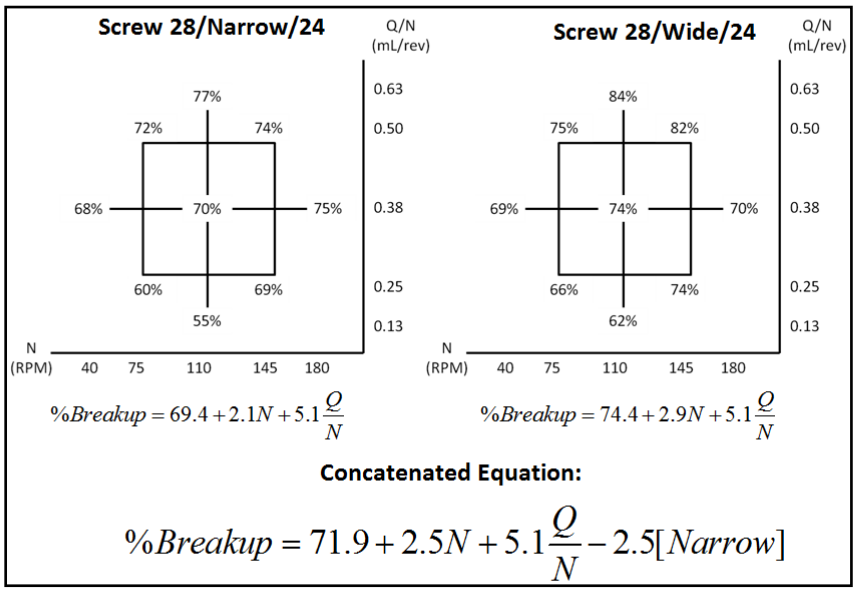

Figure 5.1: 92 kPa Bead Break-Up

Inspection of the 92 kPa bead results shows trends that will reoccur throughout the entire strength bead study. Looking at the percent break-up values in the grids, there is a consistency along the diagonals moving from the upper left to the lower right. Along this diagonal, break-up values are very similar and frequently equal. Furthermore, examination of the predictive equations below shows that only two parameters were significant with respect to percent break-up, screw speed (*N*) and specific throughput (*Q/N*). Visually this is clear because along lines of constant *N* or constant *Q/N* the break-up increases with increasing values of either parameter.

Once the data from both grids are combined and a concatenated equation formed, quantitative analysis of the screw geometries can be performed. The additional significant factor at the end of the concatenated equation "-2.5[Narrow]" symbolizes the significance of the geometry change. The coefficient linked to the geometry parameter denotes a 2.5% lower percent break-up average of the narrow kneading block screw geometry to the overall average. In other words, the wide kneading block

screw geometry broke approximately 5% more stress beads than the narrow kneading block screw geometry, which by inspection of the nodes in both grids holds true.

Examination of the 92 kPa bead geometry specific predictive equations also displayed unique results. First from geometry to geometry the magnitudes of both the *N* and *Q/N* coefficients remain about the same. For both geometries, the *Q/N* coefficient is almost double the *N* coefficient. This signified that the rate of change of percent break-up is greater when moving along the *Q/N* axis compared to the *N* axis. Thus, at this stress level the extrusion process was most sensitive to specific throughput.

The next bead strength tested was the 119 kPa grade. Figure 5.2 presents the percent break-up results for the two studied screw geometries with a set-up that mimics Figure 5.1.

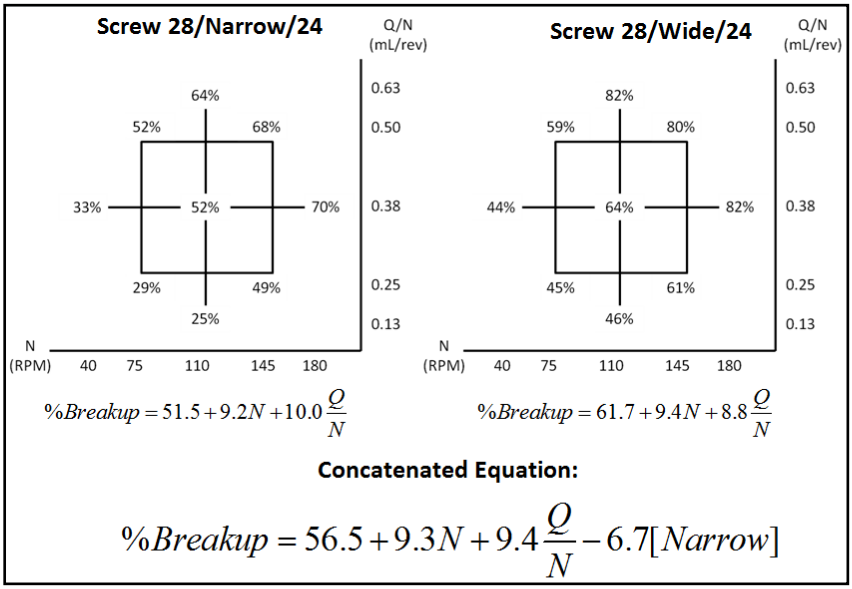

Figure 5.2: 119 kPa Bead Break-Up

The diagonal break-up trend and an exclusion of all significant parameters except *N* and *Q/N* were again observed. The concatenated equation confirms the wide

kneading block geometry broke a greater percentage of stress beads for every operating condition. The difference in the 92 kPa concatenated equation compared to the 119 kPa concatenated equation was that the difference between the average percent break-up of the wide and narrow kneading block configurations. For the 92 kPa bead strength there was a difference of about 5%, but the 119 kPa concatenate equation shows a difference of almost 14%.

For many points, CCD grid results were similar for both bead strengths. However, there was one significant change when moving from the 92 kPa to 119 kPa, the magnitude of coefficients for *N* and *Q/N*. The magnitudes for the 119 kPa predictive equations were far greater than that of the 92 kPa predictive equations, and the magnitudes were equal for both the *N* and *Q/N* coefficient. For the 92 kPa bead results the *Q/N* coefficient was much greater than the *N* coefficient. The large spike in magnitudes shows that the 119 kPa bead was a "sweet spot", where the operating conditions respond much more sensitively than what was seen for the 92 kPa results, or the 158 kPa results.

The strongest bead strength, the 158 kPa bead results are presented below in Figure 5.3. Again, the only significant parameters were *N* and *Q/N*. The break-ups along the downward left to right diagonals were about equal. The concatenated equation shows a decrease in the differential between the wide and narrow kneading block geometries, which augments the theory that the 119 kPa bead exhibited a peak with respect to the effects operating conditions had on percent rupture.

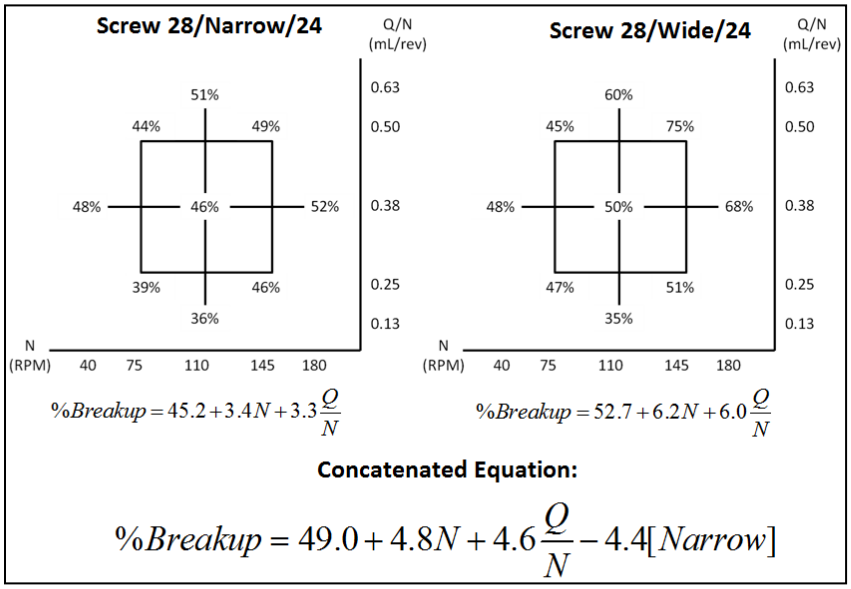

Figure 5.3: 158 kPa Bead Break-Up

In both the previous stress bead experiments, the 92 kPa and 119 kPa, the magnitudes of the *N* and *Q/N* coefficient were approximately the same between screw geometries. Yet, when moving from the Screw 28/Narrow/24 predictive equation to the Screw 28/Wide/24 predictive equation there is almost a doubling of the magnitudes of both parameter coefficients. Therefore, the strongest bead, the 158 kPa grade, was the most responsive to the screw configuration change. This is most likely due to the fact that the wider paddles of the wide kneading block geometry more easily generated an apex stress that exceeded 158 kPa.

5.1.2 Superimposed RSD Curves

The final insight of the bead strength study was found by examining all bead strengths' RSD curves simultaneously for a single operating condition. The RTD did not change because the operating condition remains constant among the three strength bead experiments. This allowed for the superposition of each stress bead curve. The operating condition used was a mass flow rate of 2.4 lb/hr and a screw speed of 75

RPM. The blue curve represents the RTD, the red, green, and magenta curves represent the RSDs for the 92 kPa, 119 kPa, and 158 kPa stress beads respectively.

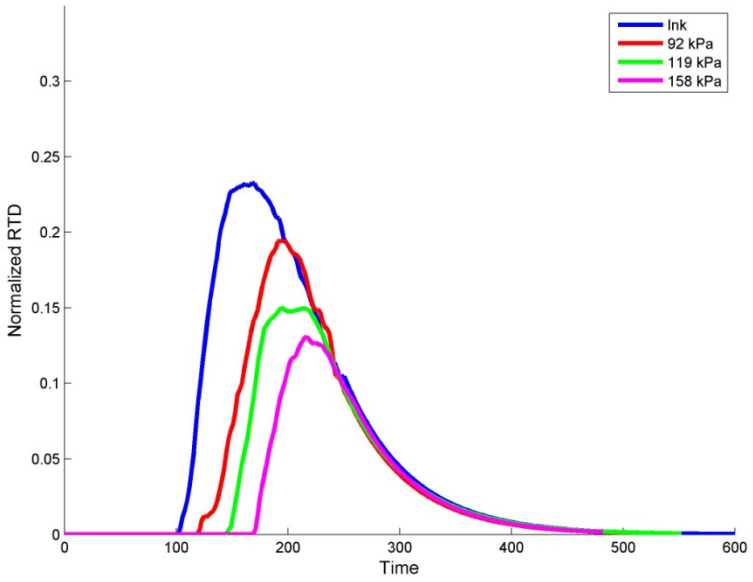

Figure 5.4: Superimposed Three Strength Bead Curves

In Figure 5.4 above, it is seen that there is a linear relationship between the three stress bead RSD curves. As the bead strength increases the amplitude and base width of the RSD curve decrease, which was expected. Another insight produced from the superimposed plots was difference in the delay time of the three RSD curves. There was again a linear relationship between delay time, the time from injection to detection by the optical probe, and the bead strength. As the bead strength increased, delay time increased. Table 5.1 below shows the values for the delay time with respect to bead strength.

Table 5.1: Bead Strength vs. Delay Time

Bead Strength [kPa]	Delay Time [sec]
92	124.0
119	155.8
158	174.0

A physical understanding of the flow, assumes the flow in the channel to be that of the flow through a pipe. Along the centerline in the pipe, seen below in Figure 5.5, the velocity gradient is zero, which translates to zero shear stress. Thus, beads traveling down the center of the channel experience little to no stress. It is also known that beads traveling through the middle of the channel will be seen first. Therefore, the phenomenon seen in Figure 5.4 (i.e. the linear relationship between the delay times of the RSD curves) can be attributed to the fact that the strongest beads will break closer to the wall where the velocity is slowest, which effectively increases delay time. This follows because the weaker beads will more easily release the encapsulated dye closer to the center of the channel and trigger the optical light probe sooner.

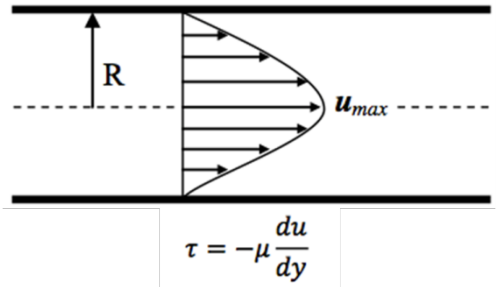

Figure 5.5: Flow through a Pipe Diagram

5.1.3 Effect of Bead Strength Conclusions

A real-time method for measuring the RSD in a TSE has been developed through the use of polymeric stress sensitive beads. The methodology has been able to quantify differences between screw geometries and operating conditions. In order to test the consistency of the percent rupture results multiple bead strengths were examined on a 28-mm extruder. For all bead strengths certain results repeated for every CCD grid. All stress bead grades found screw speed and specific throughput as

the only significant parameters. Screw speed has always been correlated to percent break-up because it is directly related to shear rate. However, specific throughput, a measure of fill, has not been linked to stress and dispersive mixing. From the results above, along lines of constant *N* the increase in percent break-up with increasing *Q/N* is definitive. The phenomenon can be related back to study performed by Gao et al. that related specific throughput to flow path. In addition, the wide kneading block geometry always broke a greater percentage of stress beads than the narrow kneading block geometry. A result that has been shown before, but through the CCD analysis a quantitative difference between performance could be measured. Finally, the trend of similar break-up along the diagonals of constant throughput was seen for all three stress beads.

However, the predictive equations associated with each bead strength produced unique characteristics. Table 5.2 shows the intercept and coefficient values for every predictive equation generated for this study.

Table 5.2: Predictive Equations Table

Kneading Block Size	Bead Strength [kPa]	Intercept (C)	*N* Coefficient (A)	*Q/N* Coefficient (B)	Configuration Difference -[Narrow]
Narrow	92	69.4	2.1	5.1	-
Narrow	119	51.5	9.2	10.0	-
Narrow	158	45.2	3.4	3.3	-
Wide	92	74.4	2.9	5.1	-
Wide	119	61.7	9.4	8.8	-
Wide	158	52.7	6.2	6.0	-
Concatenated	92	71.9	2.5	5.1	-2.5
Concatenated	119	56.6	9.3	9.4	-6.7
Concatenated	158	49.0	4.8	4.6	-4.4

The 92 kPa bead equations, for either screw geometry, showed a greater sensitivity to the specific throughput parameter. The other two bead grades had similar magnitudes for both the screw speed and specific throughput coefficients. The 119 kPa bead had much higher coefficients in comparison to the other two stress beads, which signified that the 119 kPa beads were most sensitive to the operating conditions. For manufacturers, the greater sensitivity to operating conditions allows for greater control of the stress imparted on the material. The strongest bead, the 158 kPa bead, had the only significant difference in coefficients between screw configuration changes, which indicated that the 158 kPa was most sensitive to variations in screw geometry.

Each bead strength used on the 28-mm extruder provided different insight. With a more systematic approach to testing various grades of stress beads, every process can find the stress level most sensitive to screw speed, specific throughput, and screw geometries. This can help find ideal operating condition spaces to achieve certain degrees of dispersive mixing and stress generation.

5.2 Robust Design of Experiment Approach

After the bead strength study, the next step was to examine the DOE approach. The original nine point CCD grid, implemented in the effect of bead strength study, allowed for the analysis of the relationship between percent rupture and a relatively small operating space. Thus, for the robust DOE approach study the domain of both operating conditions were broadened.

The experiments performed in this study were done at the DuPont Experimental Station and run on a bi-lobal 18-mm CoTSE. Two screw configurations with different mixing sections were used. The first screw configuration, Screw 18/Wide/16, used only wide kneading block elements in its mixing section. The second configuration, Screw 18/Narrow/16, used only narrow kneading block elements. This study also used only one stress bead. The strongest bead grade, 158 kPa, was selected, because higher shear rates and fills.

5.2.1 Percent Break-Up CCD Grids and Additional Statistical Analysis

As mentioned earlier, the starting operating space for this study was chosen due to successful results seen in prior work. The first grids seen below in Figure 5.6 will be known as the original CCD grids. The design of Figure 5.6 follows the structure of all previous CCD grids. The results in Figure 5.6 show that even with the change in extruder, the patterns observed on the 28-mm machine remain true. Percent break-up values along the diagonals moving in the lower right direction are about equal. The significant factors were consistent with the exception that the wide kneading block geometry did not find *Q/N* as a significant parameter but with a slightly more relaxed confidence interval it would have appeared, and this was seen as an anomaly. Furthermore, for every operating condition the wide kneading block geometry broke a greater percentage of beads than the narrow kneading block geometry.

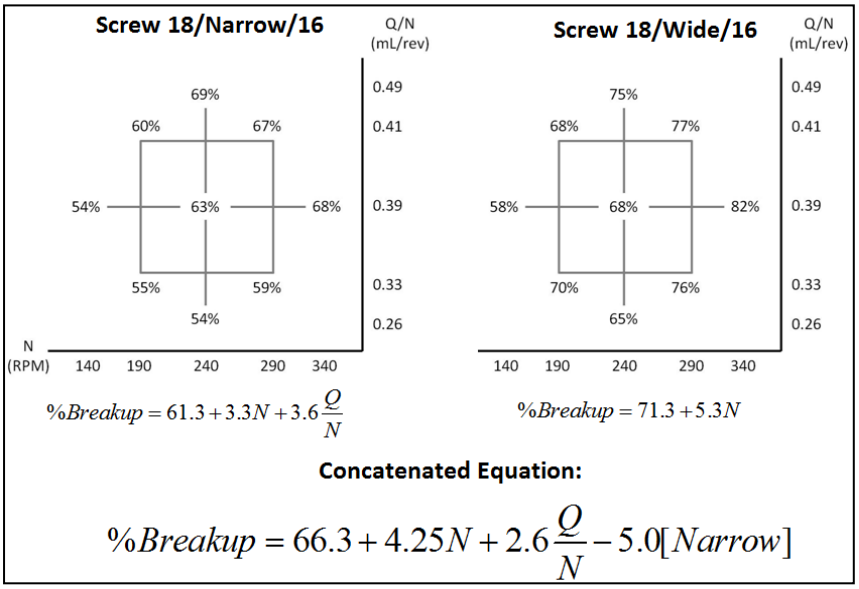

Figure 5.6: Original CCD Grid Break-Up Results

The first modification to the original CCD grids was a translational shift along the x-axis into a higher shear rate domain or increase in screw speed. The increased screw speed grid results can be seen below in Figure 5.7. The x-axis now ranges from 340-440 RPM. Increased screw speeds were investigated to better reflect industry processing conditions. Thus, determining if low shear rate trends hold at high shear rates proved to be valuable. Even though the percent rupture exceeded 80%, the results remained consistent with trends seen in the original CCD grid results. Additionally, for this set of grids the *N* and *Q/N* significant parameters appeared. Also, for the narrow kneading block geometry the magnitude of the coefficients remained the same, thus the sensitivity to operating conditions remained the same, and the increase in break-up was only evident in the offset or intercept.

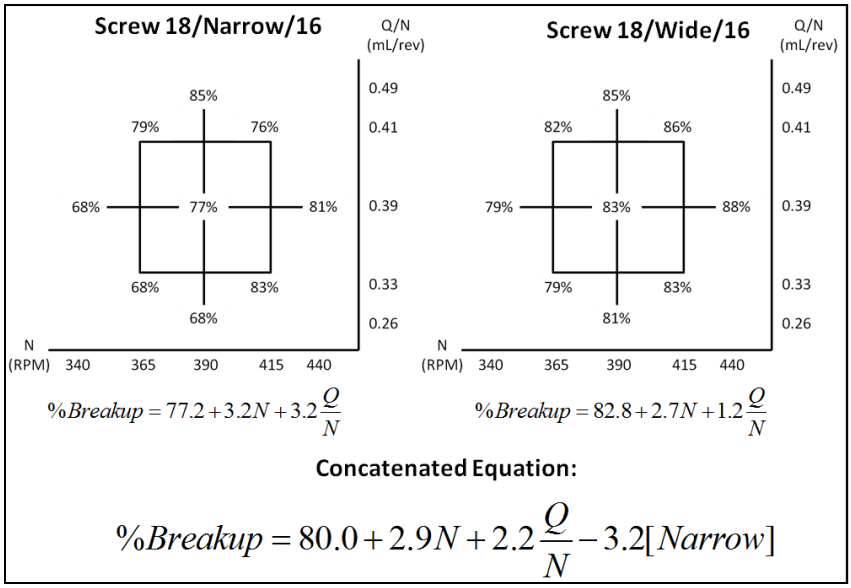

Figure 5.7: Increased Screw Speed CCD Grid Break-Up Results

Figure 5.8 shows the CCD grids connected at their common point to explore the relationship between the original grid domain and the increased screw speed space. The grey grid represents the original CCD grid. The black grid the increased screw speed grid. The concatenated equation now does not compare the percent break-ups by screw geometry, as seen before in the strength bead study, but by position on the *N*-axis. The modified grid shift proved to be a significant change because an additional parameter, symbolized by the "-7.6[Original]". The shift parameter states that the original grid on average, broke about 15% less beads than the increased screw speed grid.

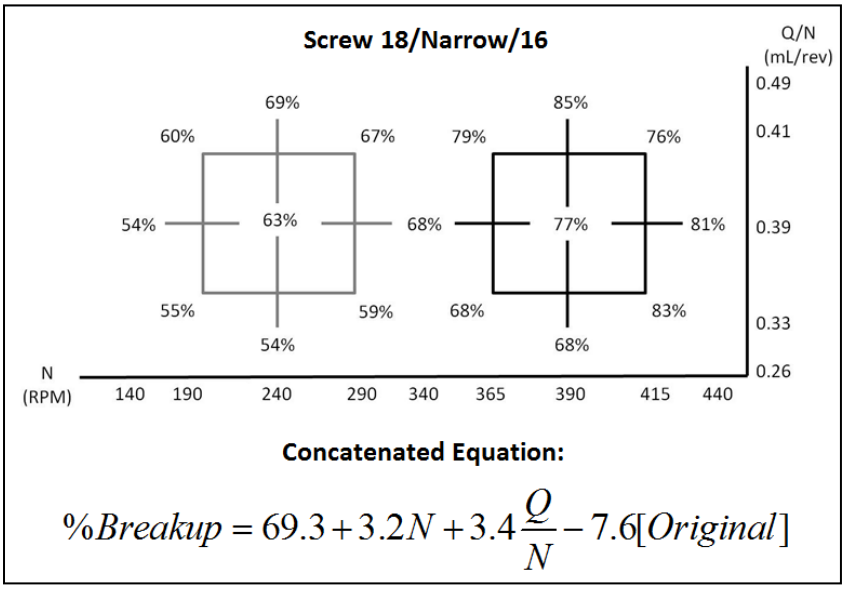

Figure 5.8: Combined Original and Increased Screw Speed Illustration, Narrow Geometry

A similar effect was found for the wide kneading block geometry concatenation, seen visually in Figure 5.9. The difference between the two CCD grids of the aggressive geometry was found about 11%.

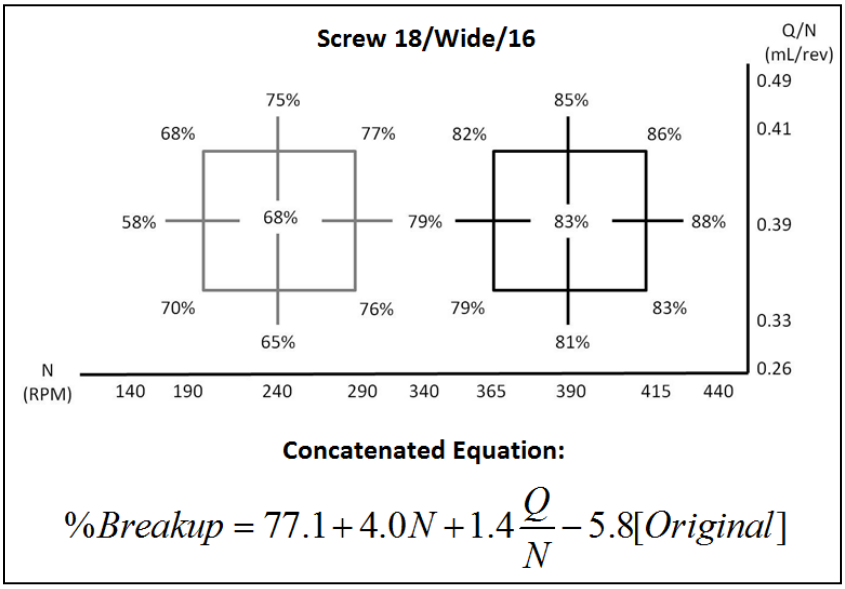

Figure 5.9: Original and Increased Screw Speed CCD Grid Illustration, Wide Kneading Block Geometry

The results above establish a quantitative relationship between lower and increased shear rate domains. Using these equations, manufacturers can choose to experiment and test certain processes at lower energy conserving screw speeds and be able to predict percent break-up in a higher shear rate environment.

The second modification dealt with an expansion in both the *N* and *Q/N* axis. Torque and machine limitations dictated the extent of the expansion. The original CCD grid had a β level of 2. The expanded cross CCD grids, seen below in Figure 5.10, have a β level of 3 along the central cross.

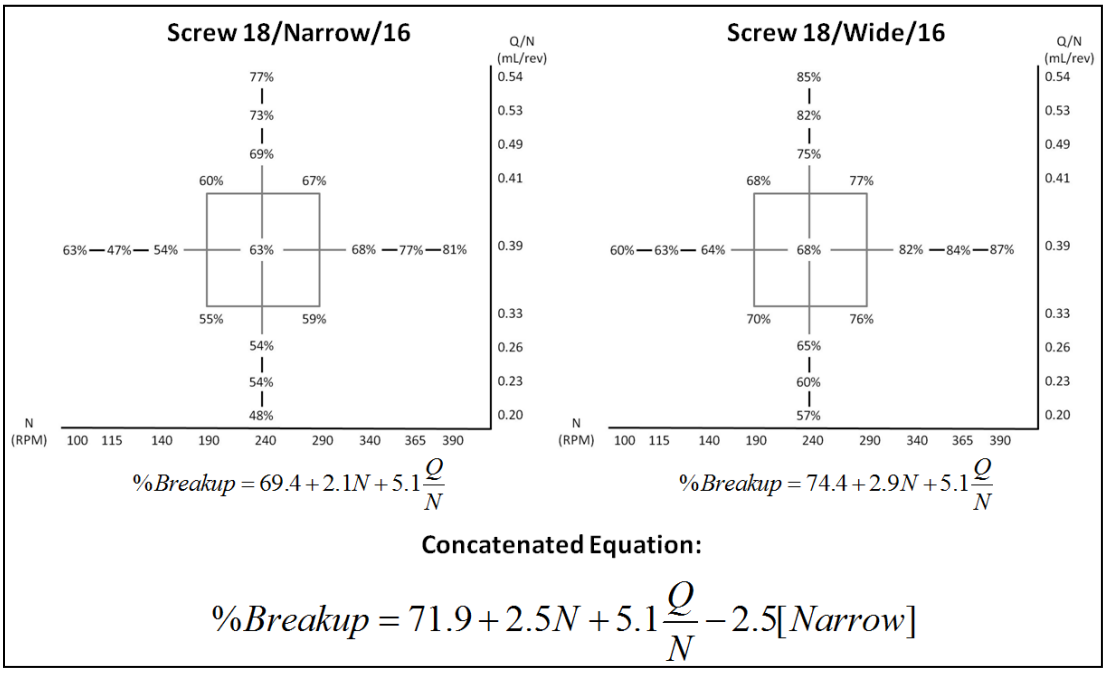

Figure 5.10: Expanded Cross CCD Grid Break-Up Results

The results in Figure 5.10 mirror many of the results previously observed in CCD grids. The parameters *N* and *Q/N* were significant even for broader ranges of fill and screw speed. However, a deeper level of analysis was provided by the use of interaction and surface profiles. The profiles and surfaces are shown below for the

narrow kneading block geometry, in Figure 5.11, and for the wide kneading block geometry in Figure 5.12. Interaction profiles hold one parameter constant and compare the effects of the other parameter on the percent break-up. In both Figure 5.11 and Figure 5.12 the top row holds *N* constant, showing the effect of *Q/N* on break-up. The bottom row holds *Q/N* constant to display the effects of *N* on percent break-up. The y-axis shows the range of break-ups for that particular CCD grid. The x-axis shows the coordinates that correspond to the CCD grid. The red and blue lines in each quadrant of the interaction profile represent the interaction between *N* and *Q/N*. If the two lines are parallel there is no direct relationship between the two independent variables. Below the interaction profiles are the response surfaces, which display the interaction profiles in a 3-D space to show the interaction between independent and dependent variables through response surfaces.

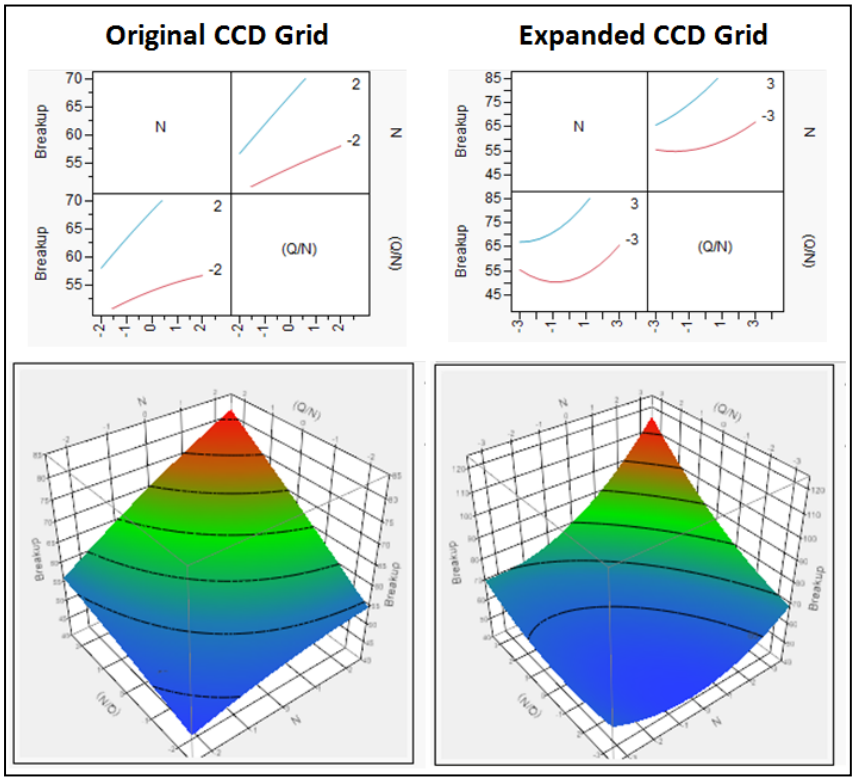

Figure 5.11: Interaction and Surface Profiles for Original and Expanded CCD Grids, Narrow Kneading Block Geometry

Differences between profiles were significant for the grids performed on the narrow kneading block geometry. For the original CCD grid there was a linear trend for both the effects of *N* and *Q/N*. Yet, when compared to the expanded CCD grid the linearity was far less pronounced. Instead the expanded grid interaction profile exhibits a convex property, with the greatest slope at the edges. Results showed that as screw speed and the specific throughput move away from the center of the CCD grid the effects the operating conditions have on percent break-up become increasingly non-linear. The non-linear trend can be attributed to percent drag flow. A study presented earlier by Cheng et al. confirmed the relationship percent drag flow had on kneading block performance [46]. It was also found that 30% drag flow was a "turning point" as far as the behavior of many performance parameters such as residence time and fill length. For the narrow kneading block the geometries, the additional levels added to the expanded cross grid break the 30% drag flow threshold value. Thus, these non-linear trends can be attributed to the physical changes occurring in the screw channels.

Figure 5.12 shows the interaction profiles and response surfaces for the wide kneading block geometry. The wide kneading block geometry also shows a non-linear trend in the expanded domain. However, it is not as exaggerated as the trend found in the narrow kneading block geometry. This could be due to the nature of the wide kneading block elements and that with such high percent ruptures an asymptotic limit was being approached. In addition, the less-pronounced non-linear behavior can be connected to the percent drag flow. Since the wide kneading blocks have a greater

maximum specific throughput, for the same operating condition it will have a lower percent drag flow than the narrow kneading block screw elements. Thus, since the outer limits of the wide kneading block geometry CCD grid do not reach 30% drag flow, the non-linear effects are not highlighted.

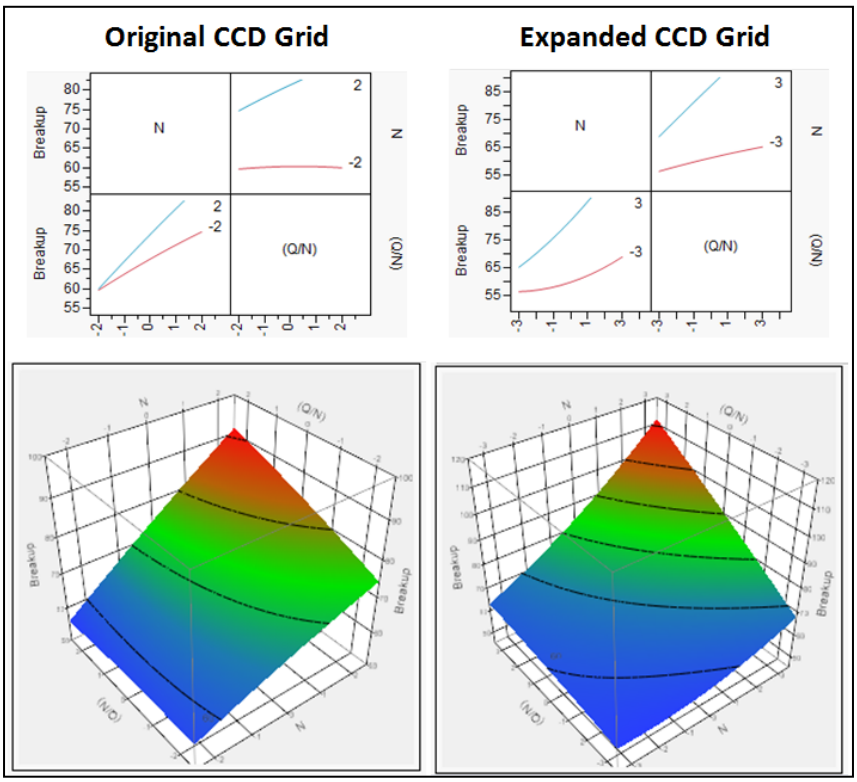

Figure 5.12: Interaction and Surface Profiles for Original and Expanded CCD Grids, Wide Kneading Block Geometry

5.2.2 Robust Design of Experiment Approach Conclusions

A DOE approach was taken to properly analyze the variation in the stress bead rupture results. Previous work used a CCD grid with nine coordinates to characterize screw geometries, extruder sizes, and operating conditions. To investigate larger domains of operating conditions, the classic CCD grid was modified in two distinct ways. The first alteration translated the grid along the x-axis to examine higher screw speeds, which was focused on testing shear rates that better reflect industry standards.

The increased screw speed grid provided a numerical value for the grid shift, which led to a better understanding of percent rupture at higher shear rates. The next adaptation to the original grid was an elongation along the central cross. The interaction profile for the expanded cross grid showed a non-linear relationship between percent break-up and both the significant parameters at the outer limits of the expanded cross grid. The greatest non-linear behavior was seen on the narrow kneading block. This was due to the percent drag flow on the ends of the CCD grid being near 30%. This has been shown by Cheng et al. to be an important turning point for percent drag flow [46]. The interaction profiles for the original grid exhibited far more linear trends. Both alterations added a level of depth to the DOE analysis. Additionally, it was confirmed that the RSD methodology results remain consistent even for a larger domain of operating conditions.

5.3 Scale-Up Phase 1 Results

The previous experiments verified the robustness of the real time RSD characterization methodology. Studies by Gasner et al. and Cheng et al. proved that percent drag flow was a critical parameter to mixing and kneading block performance [45][46]. With the increasing popularity of the polymer composites field, good dispersive mixing was made paramount in order to achieve desired property enhancement. As shown in Chapter 4, a new dispersive mixing scale-up rule was proposed that focused on percent drag flow as opposed to volumetric output, which is considered the industry standard.

The volumetric scale-up rule was based on single screw extrusion theory and was determined off of square-pitched elements and rectangular channels. With a reliable

method for quantitatively measuring the stress history an experiment was set up to compare the volumetric scale-up rule with the newly proposed percent drag flow rule. For Phase 1, the percent drag flow rule was based on the geometrical aspects of the narrow kneading blocks for the 18-mm and 26-mm CoTSEs. The narrow kneading block elements were chosen to base the percent drag flow scaling factor because they corresponded to each CoTSE's square-pitched conveying elements.

The 18-mm and 26-mm bi-lobal CoTSEs were selected as the extruders used throughout the scale-up study because of their geometric similarity. Two mixing sections were examined, one comprised of wide kneading blocks and one of narrow kneading blocks, Screw 18/Narrow/16 and Screw 26/Narrow/24 respectively. The 18-mm screw was a copy of a screw design previously used in the DOE robustness study. For Phase 1, the bead grade used was the 158 kPa beads. Determined by the calculations shown in Chapter 4, the two scaling factors for volumetric and percent drag flow scale-up were 2.8 and 2.3 respectively for *Q/N*. Shear rate remained constant because *L/D* was held constant. Although both rules were derived from square-pitched elements they are different because the volumetric rule's calculation is based on the ratio of outer screw diameters cubed while the percent drag flow approach takes into account a specified element along with the operating conditions.

5.3.1 Phase 1 CCD Grids and Additional Statistical Analysis

The first set of CCD grids shown below in Figure 5.13 compares the percent drag flow scaled grid performed on the 26-mm versus the 18-mm base grid. It should be noted that the 18-mm base grid was taken from Figure 3.31 and was previously used for the DOE robustness research.

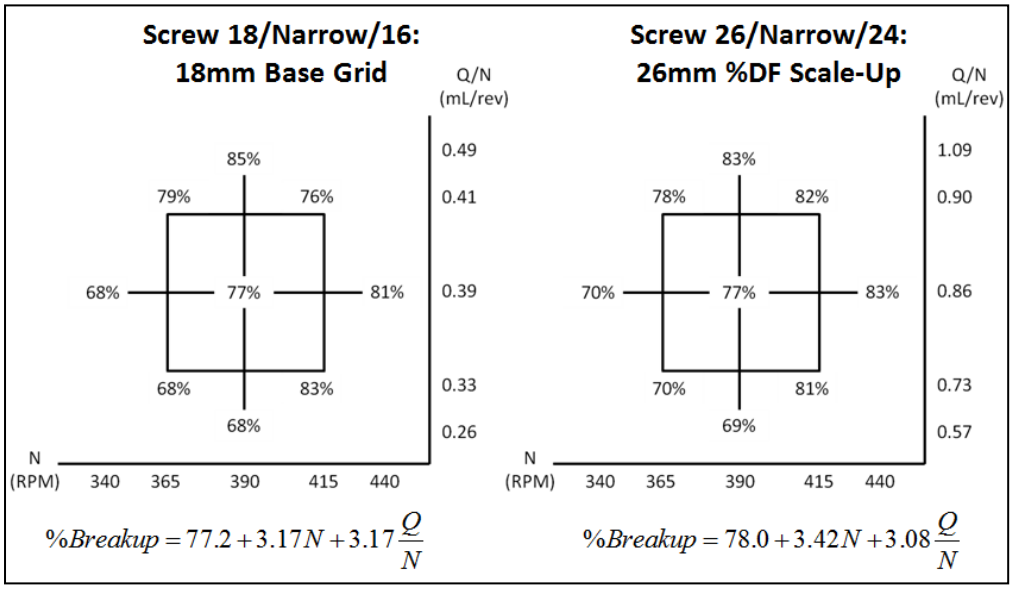

Figure 5.13: Scale-Up Phase 1 Narrow Kneading Block Geometry, 18-mm Base Grid vs. 26-mm %DF Scale-Up Results

When comparing predictive equations in Figure 5.13, there was a similarity between the base grid and percent drag flow grid. The average percent break-up was almost identical and the variation in coefficient magnitude for the two significant performance parameters, *N* and *Q/N*, were only fractions off.

This is unlike the results shown for the comparison between the base grid and volumetric grid shown below in Figure 5.14.

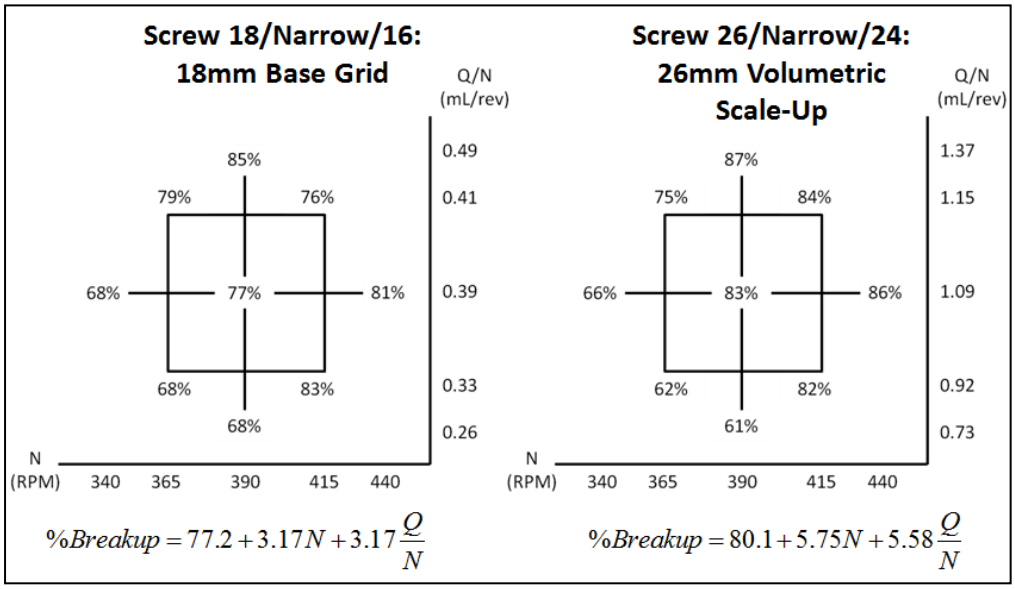

Figure 5.14: Scale-Up Phase 1 Narrow Kneading Block Geometry, 18-mm Base Grid vs. 26-mm Volumetric Scale-Up Results

The volumetric predictive equation had significantly larger magnitudes for the *N* and *Q/N* coefficients compared to the 18-mm base grid predictive equation.

Comparison of the predictive equations, although insightful, is not enough to properly evaluate the two scale-up approaches. The Fit Y by X and Distribution techniques were implemented to provide an extra level of comparison between scaling factors, results seen below in Figure 5.15.

The Oneway Analysis, generated by the Fit Y by X, provides the best visual of the most important statistical information, the means and standard deviations. In Figure 5.15 it can be seen that the green diamonds (means) are all about on the same line, and not significantly different because they were all assigned the same letter in the Connecting Letters Report. Additionally, the data was fit continuously to a normal distribution to extract additional statistical information. Inspection of the black percent break-up dots and the values for standard deviation in the table below indicate that the percent drag flow scale-up approach better mirrored the stress history seen on

the CCD grid of the model sized 18-mm. The standard deviation for the volumetric approach was nearly double that of the 18-mm base grid. Also, the spread of the black percent break-up dots for the volumetric approach begins and extends much farther apart than seen in the two other CCD grids.

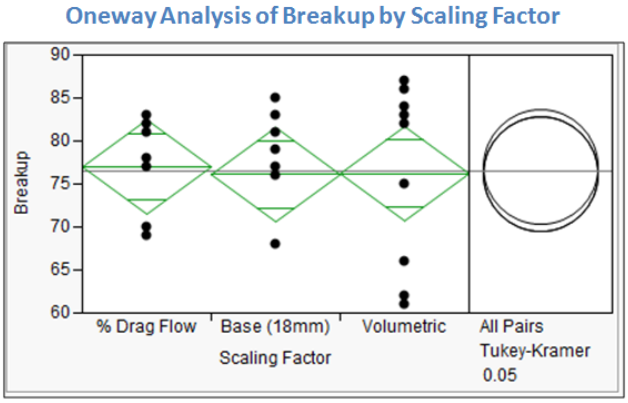

Connecting Letters Report

Level		Mean
% Drag Flow	A	77.000000
Volumetric	A	76.222222
Base (18mm)	A	76.111111

Levels not connected by same letter are significantly different.

Narrow KB Configuration Scale-Up Phase 1

Scaling Factor	μ	σ	Min.	Q1	Median	Q3	Max.
Base (18 mm)	76.1	6.68	68	68	77	82	85
% Drag Flow	77	5.87	69	70	78	82.5	83
Volumetric	76.2	10.56	61	64	82	85	87

Figure 5.15: Scale-Up Phase 1 Narrow Kneading Block Geometry, Scaling Factor Statistical Analysis

For the wide kneading block geometry, results for the percent drag flow scale-up rule compared to the base grid are presented in Figure 5.16. Again the results showed a strong correlation between the two grids and predictive equations. Although the magnitude of the *N* coefficient saw the greatest differential between coefficient magnitudes for any percent drag flow results, the intercept and specific throughput related information strongly preferred the percent drag flow rule to the volumetric rule. Volumetric scale-up approach results for the wide kneading block geometry can be seen in Figure 5.17.

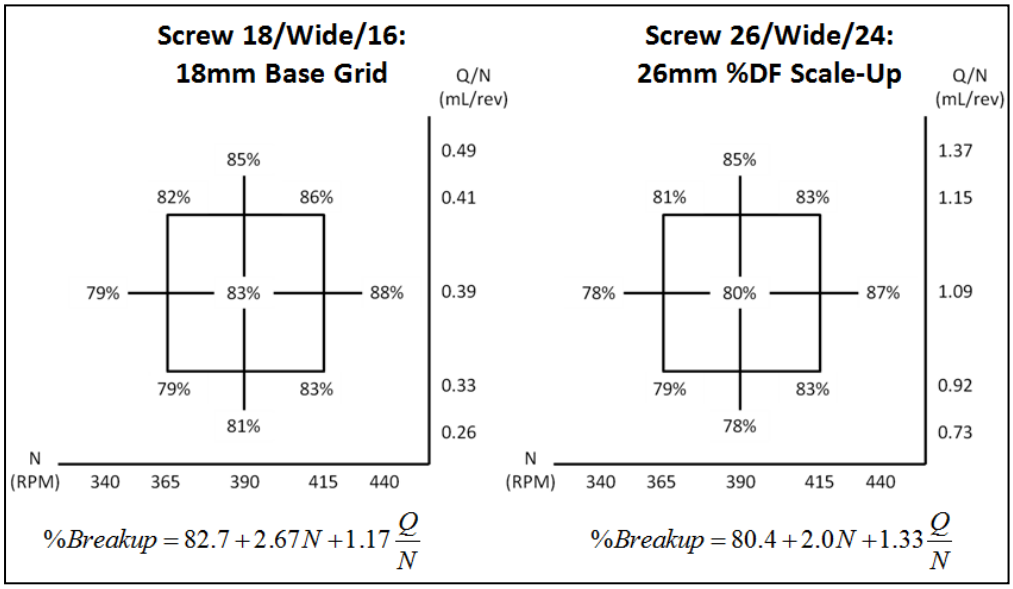

Figure 5.16: Scale-Up Phase 1 Wide Kneading Block Geometry, 18-mm Base Grid vs. 26-mm %DF Scale-Up Results

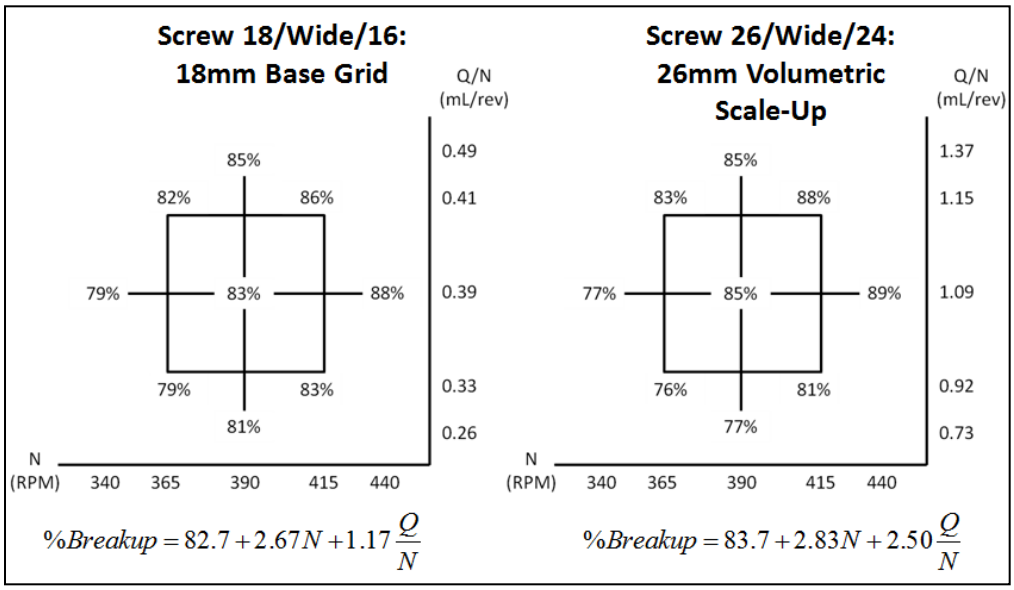

Figure 5.17: Scale-Up Phase 1 Wide Kneading Block Geometry, 18-mm Base Grid vs. 26-mm Volumetric Scale-Up Results

The comparison between the volumetric grid and base grid for wide kneading block geometry was more similar than the narrow kneading block geometry. However, the magnitude of the specific throughput coefficient almost doubled from the volumetric predictive equation to the 18-mm base predictive equation.

Continued analysis found all three means to be statistically the same, but the spread or standard deviation of the percent break-up values still showed preference toward the percent drag flow approach.

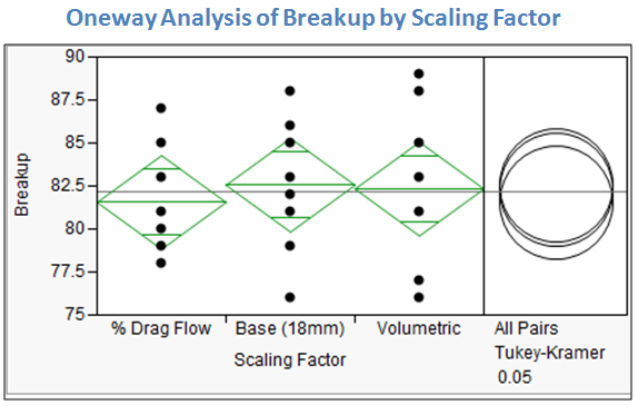

Connecting Letters Report

Level		Mean
Base (18mm)	A	82.555556
Volumetric	A	82.333333
% Drag Flow	A	81.555556

Levels not connected by same letter are significantly different.

Wide KB Configuration Scale-Up Phase 1							
Scaling Factor	**μ**	**σ**	**Min**	**Q1**	**median**	**Q3**	**max**
Base (18 mm)	82.5	3.64	76	80	83	85.5	88
% Drag Flow	81.5	3.16	78	78.5	81	84	87
Volumetric	82.3	4.87	61	76	77	83	89

Figure 5.18: Scale-Up Phase 1 Wide Kneading Block Geometry, Scaling Factor Statistical Analysis

5.3.2 Phase 1 Conclusions

The results of Phase 1 showed that the percent drag flow approach led to a more consistent stress behavior when modeling conditions from a smaller sized machine. However, the results for the wide kneading block geometry shows a greater similarity between the volumetric scale-up and percent drag flow approaches compared to the narrow kneading block geometry. Each kneading block element has a corresponding screw bushing, with the differences including the shape of the element but also the losses in the flow from the straining motion of the paddles squeezing against the barrel walls and the leakage in the spaces between the paddles. The corresponding

kneading block element to the square-pitched screw bushings on both the 18-mm and 26-mm extruder are the narrow kneading blocks. Due to this fact the wide kneading block percent drag flow scaling factor was not the best customized model for that geometry's percent drag flow scale-up rule, which led to the similarity between the results of the two approaches. In addition, the break-up results approached 90%, a territory that is far more complex to analyze. Thus, a Phase 2 was necessary to re-design a more suitable experiment.

Along with the aforementioned discontinuities, a question was raised following the results of Phase 1: what effect, if any, do the conveying elements that pump the material into the mixing section have on the rupture of the stress beads? Thus, Phase 2 was purposed not only to correct percent drag flow derivations and break-up range, but also to study the effect of the conveying element pitch used to front the mixing section.

5.4 Scale-Up Phase 2 Results

In Phase 1, although two screw configurations were examined, only one type of kneading block was used to formulate a percent drag flow scaling factor. The two screw configurations both had a mixing section comprised of wide kneading blocks, with the conveying element fronting (directly upstream) the mixing section varying in pitch. Improvement of the percent drag flow scale-up rule made sure that the percent drag flow scaling factor based on the mixing section was derived off the geometrical aspects of the wide kneading block. Since these conveying elements were responsible for pumping the material into the mixing section, it was hypothesized that they would play a role in the stress the material experienced. Two screw geometries for each

CoTSE were investigated. On the 18-mm CoTSE, the wide kneading block mixing section of both Screw 18/Wide/12 and Screw 18/Wide/16 were fronted by a narrow-pitched conveying element (12/12RH) and a square-pitched conveying element (16/16RH), respectively. The different pitched conveying elements are labeled in each screw design (denoted by the last number of the screw name). To maintain geometric similarity between the screw configurations the same conveying element and kneading block element sizes were used on the 26-mm CoTSE. The two screw configurations used were Screw 26/Wide/16 and Screw 26/Wide/24. On the 26-mm CoTSE the 16/16RH is the narrow-pitched conveying element. Due to inventory issues at MACH I Inc. the bead strength used was 221 kPa. The range of operating conditions studied for Phase 2 lowered the shear rates used in Phase 1. The percent rupture values presented in Phase 1 reached as high as 88%. Although high percent break-up values can be achieved, the analysis of a break-up range is most sensitive from 30-70% range. In addition to the shear rates the specific throughput (degree of fill) was also lowered.

The volumetric scale-up approach scaling factor remained 2.8 since the diameter of the screws did not change between Phase 1 and Phase 2. In Phase 2, there were three scaling factors associated with the percent drag flow approach. One for the wide kneading blocks in the mixing section, and two based on the conveying elements, one for each different pitch. Determining which percent drag flow scaling factor best maintained the percent break-up results observed in the 18-mm CoTSE would verify which element and percent drag flow controlled the scale-up. Although kneading block elements dominate the rupturing of the beads the conveying elements comprise

a greater portion of the screw length. The wide kneading block scaling factor was 3.0, the narrow-pitched conveying element scaling factor was 2.4, and the square-pitched conveying element scaling factor was 2.6.

5.5.1 Phase 2 CCD Grids and Additional Statistical Analysis

Figure 5.19 shown below compares the 18-mm base grid with the volumetric scale-up approach for the mixing section fronted by the narrow-pitched conveying elements. There is an approximately 6% difference in the intercept (average) values and a difference of nearly 1% in the magnitudes for the screw speed coefficient. The greatest similarity between the grids is seen between the magnitudes of the specific throughput coefficient, which still has a difference of 0.59.

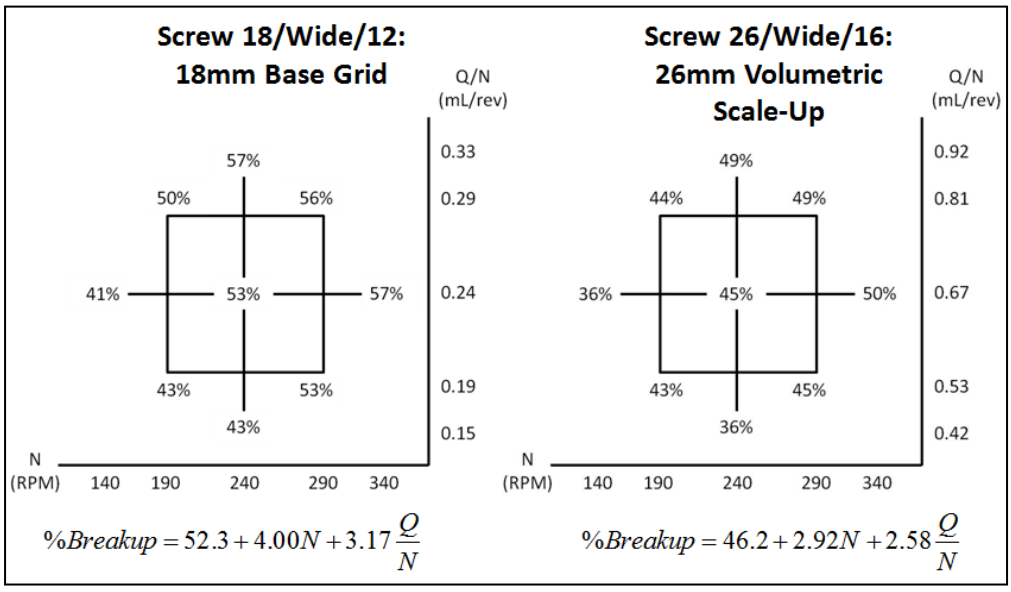

Figure 5.19: Scale-Up Phase 2 Wide Kneading Block and Narrow Conveying Element Geometry, 18-mm Base Grid vs. 26-mm Volumetric Scale-Up Results

Although the difference in means between the 18-mm base grid and volumetric approach are not significantly different, there are discrepancies between the sensitivity of the significant parameters. The first pair of screw geometries being compared is Screw 18/Wide/12 and Screw 26/Wide/16, the configurations with the

narrow-pitched conveying elements fronting the mixing section. Figure 5.20 compares the 18-mm base grid with the percent drag flow scaling factor based on the narrow-pitched conveying elements. This means that the two grids have the same percent drag flow in their respective conveying elements upstream of the mixing section. The difference for the percent break-up average is approximately 10%. The 10% difference is significant, which is shown in the Connecting Letters Report in Figure 5.22. The predictive equations also lack similarity when comparing the magnitudes of the coefficients for screw speed and specific throughput.

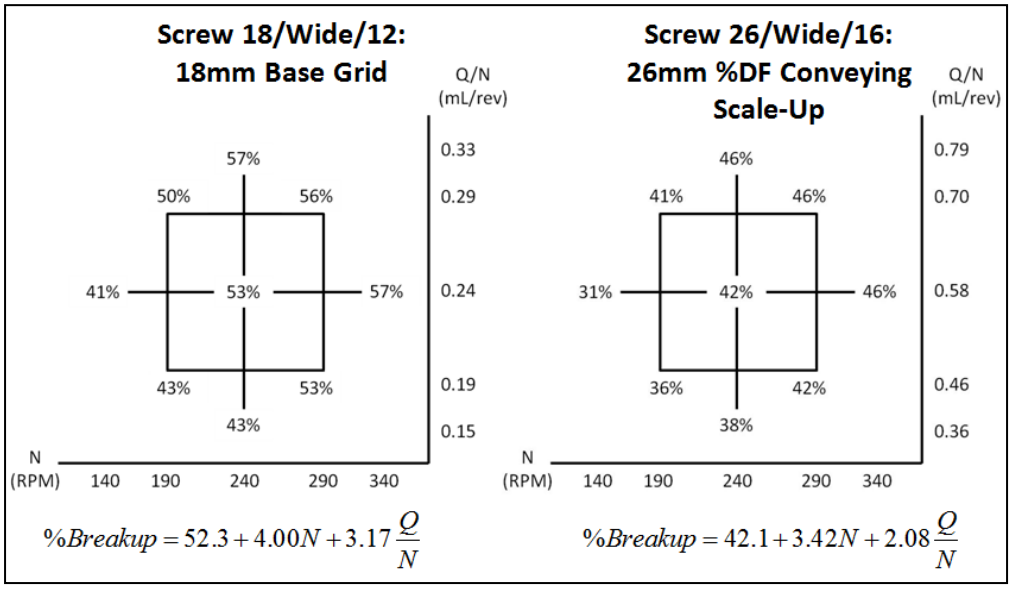

Figure 5.20: Scale-Up Phase 2 Wide Kneading Block and Narrow Conveying Element Geometry, 18-mm Base Grid vs. 26-mm %DF Narrow-Pitched Conveying Scale-Up Results

Figure 5.20 above shows that scaling with respect to the narrow-pitched conveying elements was a poor scale-up rule for percent break-up using these screw configurations. Figure 5.21 displays the results for the next percent drag flow scaling factor based on the wide kneading block elements. Inspection of the two predictive equations below shows the best consistency relative to all previously presented Phase

2 results. There is only a difference of 2% between the average values, the specific throughput coefficient is equal, and the screw speed coefficient only differs by 0.33.

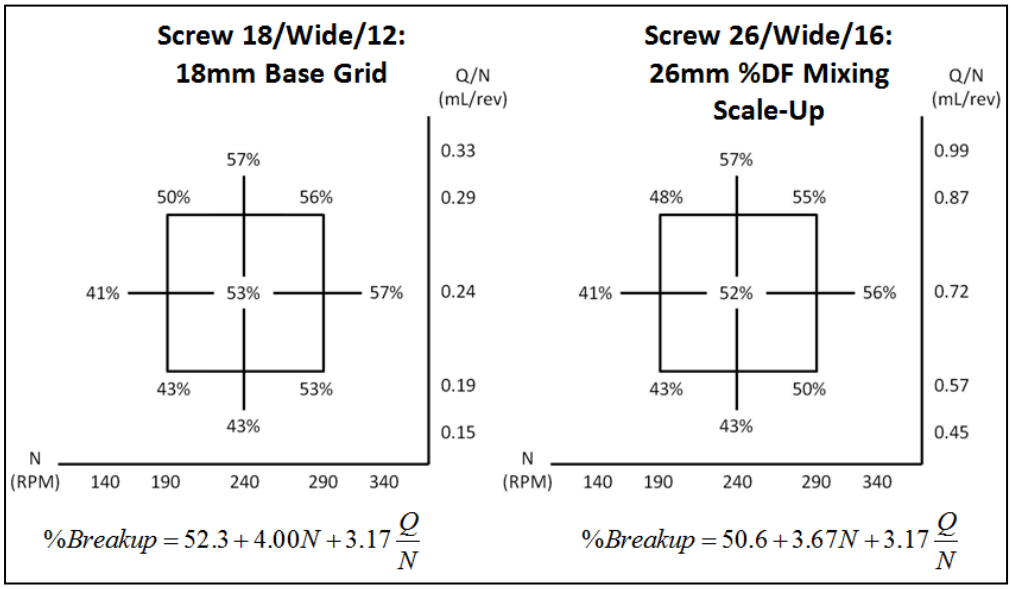

Figure 5.21: Scale-Up Phase 2 Wide Kneading Block and Narrow Conveying Element Geometry, 18-mm Base Grid vs. 26-mm %DF Mixing Scale-Up Results

The Oneway Analysis and distribution results are presented below in Figure 5.22. The additional statistical analysis confirms the most consistent scaling factor to be the percent drag flow scaling factor based on the wide kneading blocks (%DF Mixing in Figure 5.22). The 18-mm base green diamond is on line with the percent drag flow wide kneading block scaling factor, and the distribution of the percent break-up values (black dots) are very similar. Furthermore, the Connecting Letters Report only highlights the percent drag flow scaling factor based on the narrow-pitched conveying element as significantly different, and therefore rules it out as a viable option. The table below the Oneway Analysis also shows that the distribution of the 18-mm base grid best resembles the percent drag flow mixing section scaling factor grid by the standard deviation value difference of only 0.42.

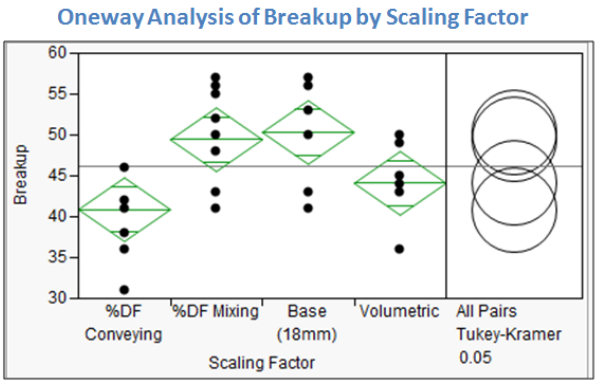

Connecting Letters Report

Level		Mean
Base (18mm)	A	50.333333
%DF Mixing	A	49.444444
Volumetric	A B	44.111111
%DF Conveying	B	40.888889

Levels not connected by same letter are significantly different.

Scale-Up Phase 3: Screw 18/Wide/12 to Screw 26/Wide/16							
Scaling Factor	**μ**	**σ**	**Min.**	**Q1**	**Median**	**Q3**	**Max.**
Base (18 mm)	50.3	6.42	41	43	53	56.5	57
%DF Mixing	49.4	6.06	41	43	50	55.5	57
%DF Conveying	40.8	5.13	31	37	42	46	46
Volumetric	44.1	5.20	36	39.5	45	49	50

Figure 5.22: Scale-Up Phase 2 Wide Kneading Block and Narrow Conveying Element Geometry, Scaling Factor Statistical Analysis

Although the percent drag flow scaling factor based on the wide kneading blocks was overwhelmingly the most consistent scale-up rule for the first pair of screw geometries, it is important to see if this effect remains for the second pair of screw configurations.

The second set of geometries uses the square-pitched conveying element to front the mixing section. The mixing section was again comprised of wide kneading blocks to isolate the effect, if any, of the conveying element pitch on percent rupture. Figure 5.23 compares the volumetric scale-up approach to the 18-mm base grid. Similar to the results for the narrow-pitched conveying element geometries, the difference between the intercepts was approximately 5%. For this set of screw geometries the volumetric scale-up approach had the largest difference in the magnitude of the specific throughput coefficients. Overall the volumetric approach continued to present

a scaled CCD grid that was not a precise method in maintaining the percent break-up values found on the model sized extruder for a range of operating conditions.

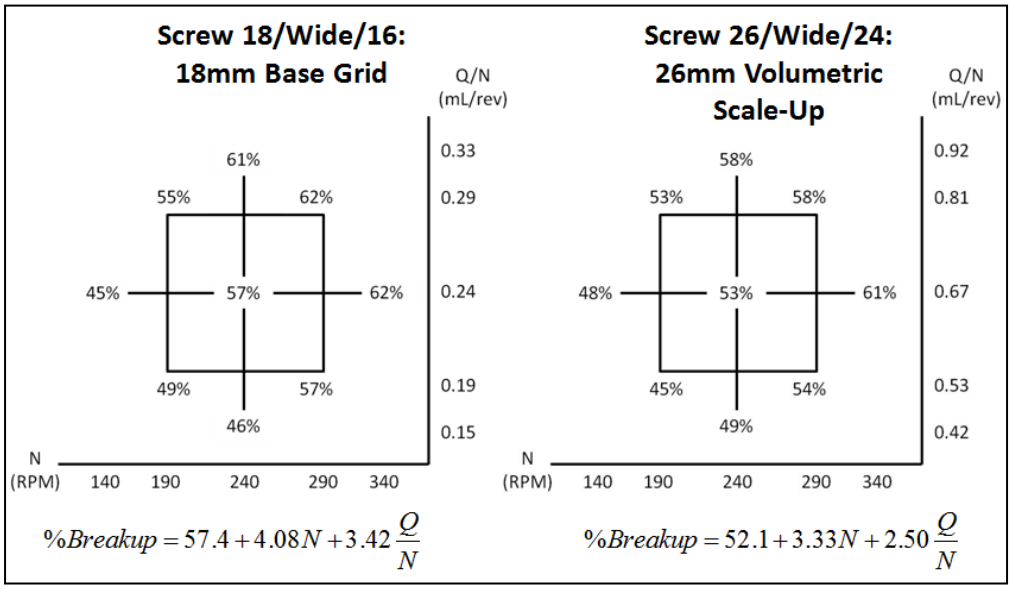

Figure 5.23: Scale-Up Phase 2 Wide Kneading Block and Square-Pitched Conveying Element Geometry, 18-mm Base Grid vs. 26-mm Volumetric Scale-Up Results

Next, Figure 5.24 presents the results for the percent drag flow scaling factor based on the square-pitched conveying elements. Comparable to the results seen in the previous set of screw configurations, the largest difference in percent break-up average was found for the conveying element scaling factor. Identical to the narrow-pitched conveying element scaling factor, the square-pitched conveying element scaling factor had an intercept difference of 10%.

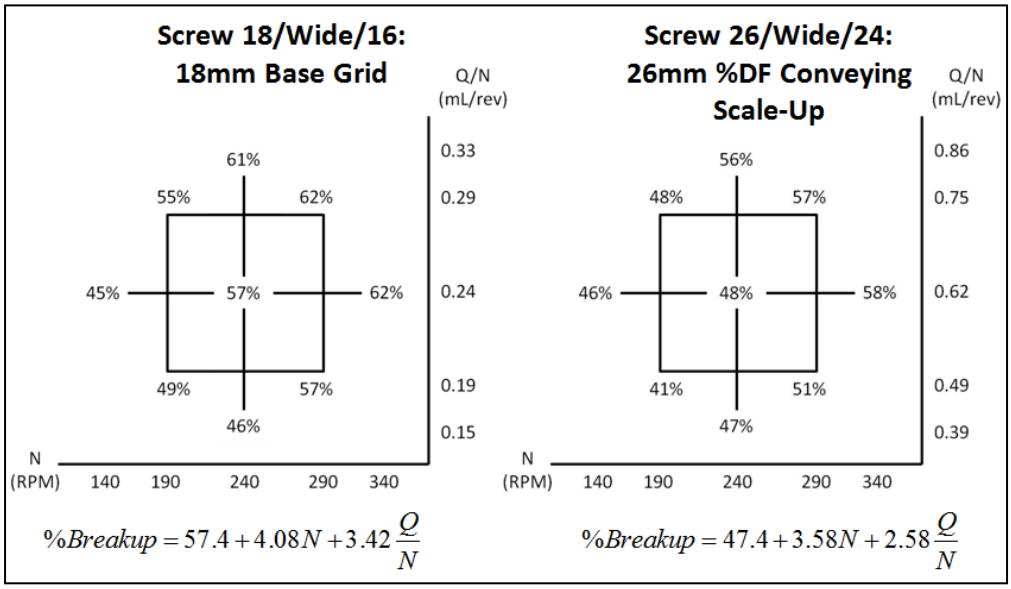

Figure 5.24: Scale-Up Phase 2 Wide Kneading Block and Square Conveying Element Geometry, 18-mm Base Grid vs. 26-mm %DF Square-Pitched Conveying Scale-Up Results

However, the importance of the square-pitched conveying element results was the difference in break-up when the conveying element was changed. For the two 18-mm base grids found, when the pitch of the fronting conveying element increased there was a significant percent break-up increase, approximately 5%. For the two 26-mm scaled grids, a similar trend was found with a percent break-up difference of approximately 9%. Table 5.3 below tabulates the concatenated equations for both CoTSEs presenting the results mentioned above.

Table 5.3: Conveying Element Pitch Change Results

Extruder Size [mm]	Conveying Element Change	Intercept (C)	*N* Coefficient (A)	*Q/N* Coefficient (B)	Configuration Difference -[Narrow-Pitched]
18-mm	12/12RH to 16/16RH	54.9	4.04	3.29	-2.3
26-mm	16/16RH to 24/24RH	44.8	3.5	2.33	-4.67

The final scaling factor examined was the percent drag flow scaling factor based on the wide kneading block elements that comprised the mixing section. For the square-pitched geometry the wide kneading block based scaling factor still proved to be the most consistent approach for dispersive mixing scale-up. There was about a 1% difference in average values, for this set of screws the screw speed coefficient was equal, whereas for the narrow-pitched conveying element geometries the specific throughput coefficient was equal. Additionally, there was only a 0.5 difference in the magnitude for the specific throughput coefficient.

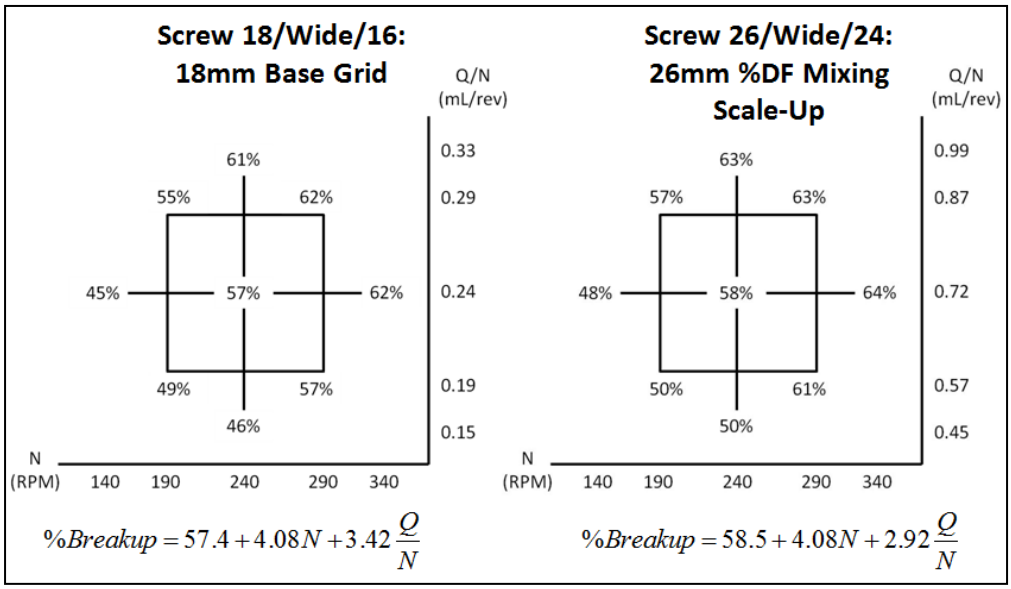

Figure 5.25: Scale-Up Phase 2 Wide Kneading Block and Square-Pitched Conveying Element Geometry, 18-mm Base Grid vs. 26-mm %DF Mixing Scale-Up Results

Figure 5.26 presents the additional statistical analysis for comparing the various scaling factors. Unlike the narrow-pitched conveying element screw geometries, the scaling factor based on the conveying elements was not ruled out by the Connecting Letters Report, but it did display the greatest difference in percent break-up. Although the spread of the percent break-up values between the 18-mm base grid and the percent drag flow scaling factor based on the mixing section were not as similar as

seen for the narrow-pitched conveying element geometry, the standard deviation values were just as close. The differential for the standard deviation value for both geometries was approximately 0.4. Inspection of the table below the Oneway Analysis also shows the significant difference in distribution between the volumetric scaled CCD grid and the 18-mm base grid, equal to 1.45.

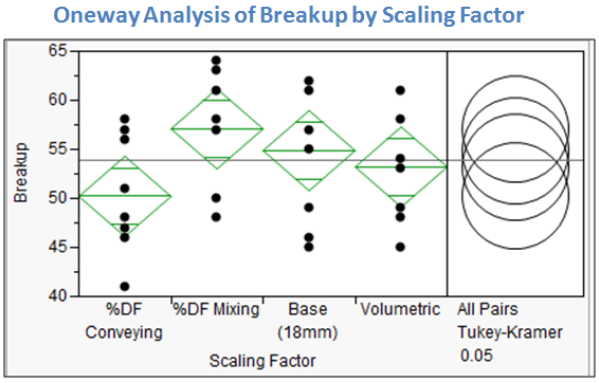

Connecting Letters Report

Level		Mean
%DF Mixing	A	57.111111
Base (18mm)	A	54.888889
Volumetric	A	53.222222
%DF Conveying	A	50.222222

Levels not connected by same letter are significantly different.

Scale-Up Phase 3: Screw 18/Wide/16 to Screw 26/Wide/24							
Scaling Factor	**μ**	**σ**	**Min.**	**Q1**	**Median**	**Q3**	**Max.**
Base (18 mm)	54.9	6.69	45	47.5	57	61.5	62
%DF Mixing	57.1	6.29	48	50	58	63	64
%DF Conveying	50.2	5.74	41	46.5	48	56.5	58
Volumetric	53.2	5.24	45	48.5	53	58	61

Figure 5.26: Scale-Up Phase 2 Wide Kneading Block and Square-Pitched Conveying Element Geometry, Scaling Factor Statistical Analysis

For the second set of screw geometries studied for Phase 2, using the square-pitched conveying element fronting the mixing section the most consistent scale-up rule was again the percent drag flow scale-up approach based on the percent drag flow of the wide kneading blocks in the mixing section.

5.5.2 Phase 2 Conclusions

Phase 2 showed again that the RSD methodology and DOE approach was a valid technique for evaluating scale-up with respect to dispersive mixing. Observation of all the results presented in Phase 2 concludes, overwhelmingly, that the most precise dispersive mixing scale-up rule was the percent drag flow scale-up approach based on the mixing section kneading block elements. For both geometries, which were different by the conveying element that fronted the mixing section, the percent drag flow scale-up rule based on the wide kneading blocks showed the closest percent break-up average, standard deviation, and magnitudes of significant parameter coefficients. Along with the quantitative similarities there was also a visual likeness between the 18-mm base grid and percent drag flow mixing section scale-up rule results shown in the two Oneway Analysis diagrams.

In addition to results comparing the scaling factors, there was a significant percent break-up difference found between geometries with different pitched conveying elements fronting the mixing section for both the 18-mm and 26-mm CoTSEs. These results prove that the pitch of the conveying elements affect the amount of stress imparted on the material in the mixing section. Although the narrow-pitched conveying elements exhibited higher percent drag flow, shown in Chapter 4, the square-pitched conveying elements broke a greater percentage of beads. The reasoning for the increase in break-up, despite the loss in percent drag flow, are due to the larger screw crests (widths) of the square-pitched elements. The larger screw crests translates to greater 100% specific throughputs. Thus, even though the percent drag flow is less the degree of fill or volume per revolution is equal or even larger.

The larger screw crests also better model the squeezing that the kneading blocks generate, although it is considerably less than a kneading block.

Finally, the results in Phase 2 and Phase 1 show that the industry standard, the volumetric scale-up approach, does not most accurately scale-up dispersive mixing between extrusion processes. A scaling factor that is calculated by a constant dimension, such as the ratio of diameters cubed could not maintain the percent break-up of stress sensitive beads across a space of operating conditions; even though, the average percent break-up may not be significantly different. Instead, the most reliable rule to scale-up stress sensitive processes is through percent drag flow, where operating conditions are considered in the calculation of the scaling factors.

Chapter 6 Conclusions

A methodology has been developed using stress sensitive polymeric beads and a DOE approach to effectively characterize, in real-time, the RSD. The analysis of the percent break-up results relates stress history with operating conditions and various screw geometries.

The purpose of this study was to propose a new dispersive mixing scale-up approach based on percent drag flow. The percent drag flow scale-up rule was compared to the industry standard (volumetric approach). The approaches were evaluated using a methodology that measures the RSD within a twin-screw extruder. Through the RSD methodology it was shown that the percent drag flow scale-up rule was a more accurate and effective approach to modeling the stress history between a laboratory sized extruder to a larger industrial grade extruder for a range of operating conditions.

Additionally, the study also had sub-objectives. Experiments were completed as an extension to work performed by W. Pappas to prove the robustness of the RSD methodology.

6.1 Effect of Bead Strength Findings

In order to verify the RSD methodology as an effective industrial technique, experiments were performed on a 28-mm CoTSE using three different stress bead strengths. Results of each bead strength provided unique findings about the screw configurations and operating conditions used.

Several trends were found to occur for all three bead strengths. Percent rupture of the stress beads was only a function of two operating parameters: (1) screw speed (*N*), and (2) specific throughput (*Q/N*). For every operating condition, the wide kneading block screw configuration broke a greater percentage of stress beads than the narrow kneading block configuration. Along the decreasing diagonals from left to right, the percent rupture was approximately equal. Finally, two relationships were found for increasing bead strength: as bead strength increased (1) percent rupture linearly decreased, and (2) delay time of the RSD curves linearly increased.

In addition to the results found for all three bead strengths, each bead strength presented its own unique findings. The weakest bead strength, 92 kPa, had the only set (for both wide and narrow kneading block geometries) of predictive percent break-up equations that showed a significantly higher *Q/N* coefficient than *N*. The high *Q/N* coefficient indicated that flow path (degree of fill) dominated percent rupture of the 92 kPa beads. For the 119 kPa predictive equations, the magnitude of the coefficients for both significant parameters was much greater than the other two bead strength equations. Therefore, sensitivity to operating conditions was greatest at an average stress level of 119 kPa. Finally, only the 158 kPa bead predictive equations showed a significant change in magnitude of *Q/N* and *N* coefficients when changing screw geometry. The highest stress level was most sensitive to the change in mixing section.

The significance of all these results proved that certain trends repeat, regardless of bead strength. Furthermore, determination of percent break-up is purely a function of *Q/N* and *N*, all other operating parameters are statistically insignificant on a 95%

confidence interval. Additionally, performing the RSD experiment on an extruder using multiple bead strengths can indicate heightened sensitivity of certain parameters for specific stress levels, which can be invaluable to manufacturers who troubleshoot stress sensitive processes.

6.2 Robust Design of Experiment Approach Findings

In addition, the RSD methodology was studied by modifying the CCD grids used to interpret the percent break-up data. CCD grids related percent break-up results to both operating conditions and screw configurations. Using a bi-lobal 18-mm CoTSE, higher screw speeds and an expanded CCD grid were investigated. These grid alterations led to greater insight on percent break-up relationships, as well as verifying the robustness of the DOE approach.

It was important to translate the CCD grid into higher shear rate regimes to better reflect industry standards. Results of the increased screw speed grids showed that *Q/N* and *N* were still the only significant operating conditions with respect to percent break-up. Furthermore, having both the results of the original and increased screw speed grids provided an extra significant parameter that quantitatively measured the difference in average percent rupture between the two grids. The value of the shift parameter can be used to predict stress histories at higher screw speeds, without having to run at those energy and resource consuming conditions.

Increasing the β level to three or extending the central cross, broadened the CCD analysis in both specific throughput and screw speed. Again, for these expanded cross CCD grids the only significant operating conditions with respect to percent break-up were *Q/N* and *N.* The pertinent finding of the expanded cross grids was the non-linear

relationship percent break-up has with both operating conditions when approaching the end points of the modified grid.

Both modified CCD grids were able to characterize a broadened range of operating conditions. Characterization of larger domains of operating conditions shows the robustness of the CCD and DOE approach, and strengthens the understanding of the relationships percent break-up has with the extrusion process.

6.3 Scale-Up Phase 1 & 2 Findings

The results found in Section 6.1 and 6.2 were necessary to confidently apply the RSD methodology to the dispersive mixing scale-up issue. Direct correlation between percent break-up and stress within the extruder provides a measure for dispersive mixing in twin-screw compounding. Using a bi-lobal 18-mm CoTSE as a model-sized extruder and a bi-lobal 26-mm CoTSE as a scaled extruder, the RSD methodology compared the dispersive mixing effectiveness of an industry standard (volumetric) scale-up rule to a newly proposed scale-up rule based on percent drag flow.

Phase 1 studied two screw configurations with different mixing sections, one comprised of wide kneading blocks the other narrow kneading blocks. Between the 18-mm base grid and the scaled 26-mm grids the range of screw speeds used was kept constant. The volumetric approach, based on single screw extrusion theory, scaled the specific throughput by a factor of 2.8. For Phase 1, only one percent drag flow scaling factor, based on the percent drag flow of narrow kneading blocks (for each extruder), was used for both screw configurations. The percent drag flow scaling factor scaled specific throughput by a factor of 2.3. Results found the percent break-up means to be equivalent for both scale-up approaches. However, the percent drag flow scale-up

rule more precisely maintained the distribution of percent break-up values across the CCD grid coordinates, which was seen most notably in the narrow kneading block screw configuration.

Phase 2 expanded on the results found in Phase 1 by using two percent drag flow scaling factors: based on (1) the kneading blocks in the mixing section, and (2) the conveying elements fronting the mixing section. The two screw geometries studied kept a constant mixing section of wide kneading blocks, but changed the pitch of the conveying elements fronting the mixing section. One configuration used narrow-pitched conveying elements, and the other used square-pitched conveying elements. Derivation of the percent drag flow scaling factors was changed to reflect experimental drag flow results. The percent drag flow scaling factor based on the wide kneading blocks scaled specific throughput by a factor of 3.0. The percent drag flow scaling factor based on the narrow- and square-pitched conveying elements scaled specific throughput by a factor of 2.4 and 2.6 respectively. The volumetric scaling factor remained at 2.8.

Similar to the results in Phase 1, the percent drag flow scaling factor based on the wide kneading blocks best maintained the mean and standard deviation of the percent break-up results observed on the 18-mm extruder. For both geometries the percent drag flow scale-up rule based on the wide kneading blocks overwhelmingly out-performed the volumetric scale-up rule. Additionally, although the percent drag flow scaling factor based on the conveying elements was unsuccessful in maintaining the percent break-up average, a significant result was found between the two screw configurations. Changing the pitch of the conveying element significantly affected the

percentage of ruptured stress beads. The larger screw crests of the square-pitched conveying elements led to a greater percent rupture of stress beads for every operating condition.

6.4 Intellectual Contributions

Overall, the RSD methodology proved to be a valid technique for evaluating dispersive mixing scale-up rules. The contribution of this study was using this RSD methodology to show that the newly proposed percent drag flow scale-up rule was a more consistent and reliable approach to modeling dispersive mixing scale-up than the industry standard volumetric scale-up approach. The scale-up study showed that the constant volumetric scaling factor based only on the screw diameters was not sufficient in maintaining the stress history across a range of operating conditions. Because the volumetric approach was only a function of the screw diameters, over a range of operating conditions it performed poorly compared to the percent drag flow approach, which actually took into account the operating conditions. For the screw geometries investigated it was shown that the percent drag flow scale-up rule based on the kneading blocks in the mixing section was shown to best reflect the results found on the model sized 18-mm extruder. The percent drag flow rule was more precise because it was based on the operating conditions and specific screw element geometry. Application of the more dynamic percent drag flow scale-up rule will augment the ability of manufacturers to take the screw configuration and operating conditions on a laboratory sized compounding process and scale-up to an industrial grade process.

6.5 Future Work

Based on the contributions found during this study, future work could be developed in the following ways:

- The scale-up between an 18-mm and 26-mm CoTSE is not a large enough transformation. The percent drag flow scale-up rule needs to be evaluated for larger extruders, where heat transfer effects become increasingly important.
- The screw configurations studied never investigated changes in effective length (in either the mixing or conveying sections). The scale-up study can be performed on screw geometries that reduce and stretch the mixing and conveying sections. This will provide insights into how the scale-up rule changes with fill length.
- The RSD methodology has now been applied, using various strength beads, to ranges of operating conditions, different screw geometries, and different sized extruders. However, a relatively unstudied realm is relating the RSD to material properties and product quality. Connecting the RSD to the final product could be directed in several ways:
  - Studying high weight percentages of HDPE filled with TiO_2 and relating the percent break-up results with measures of dispersion within the final product.
  - Studying polymers filled with carbon microfibers and nanotubes and relating the percent break-up results with properties such as: thermal, mechanical, and electrical properties.

- Applying the RSD methodology to the pharmaceutical industry, where active pharmaceutical ingredients are dispersed in a polymer based system. The percent break-up results can be related to various performance indicators such as: degree of crystallinity, temperature degradation, and drug effectiveness.

Appendix A

18-mm Screw Geometry Details:

Screw 18/Narrow/16:

Position	Element Name	Pitch [mm]	Axial Length [mm]
1	12/12RH	12	12
2	16/16RH	16	16
3	36/18SK	36	18
4	36/18SK	36	18
5	36/18SK	36	18
6	24/12SK-N	24	12
7	24/24RH	24	24
8	16/16RH	16	16
9	KB45/5/24	48	24
10	KB90/5/16	16	16
11	KB90/5/16	16	16
12	16/08LH	16	8
13	16/08LH	16	8
14	24/24RH	24	24
15	24/24SK	24	24
16	24/24SK	24	24
17	24/12SK-N	24	12
18	24/24RH	24	24
19	24/24RH	24	24
20	24/24RH	24	24
21	24/24RH	24	24
22	24/24RH	24	24
23	24/24RH	24	24
24	24/24RH	24	24
25	24/24SK	24	24
26	24/24SK	24	24
27	24/12SK-N	24	12
28	24/24RH	24	24
29	24/24RH	24	24
30	16/16RH	16	16
31	KB45/5/08	16	8
32	KB45/5/08	16	8
33	KB45/5/08	16	8
34	KB45/5/08	16	8
35	KB45/5/08	16	8
36	KB45/5/08	16	8
37	16/08LH	16	8
38	16/08LH	16	8
39	24/24RH	24	24
40	24/24RH	24	24
41	24/12RH	24	12
42	16/16RH	16	16
43	TIP	0	13.6

Screw 18/Wide/16:

Position	Element Name	Pitch [mm]	Axial Length [mm]
1	12/12RH	12	12
2	16/16RH	16	16
3	36/18SK	36	18
4	36/18SK	36	18
5	36/18SK	36	18
6	24/12SK-N	24	12
7	24/24RH	24	24
8	16/16RH	16	16
9	KB45/5/24	48	24
10	KB90/5/16	16	16
11	KB90/5/16	16	16
12	16/08LH	16	8
13	16/08LH	16	8
14	24/24RH	24	24
15	24/24SK	24	24
16	24/24SK	24	24
17	24/12SK-N	24	12
18	24/24RH	24	24
19	24/24RH	24	24
20	24/24RH	24	24
21	24/24RH	24	24
22	24/24RH	24	24
23	24/24RH	24	24
24	24/24RH	24	24
25	24/24SK	24	24
26	24/24SK	24	24
27	24/12SK-N	24	12
28	24/24RH	24	24
29	24/24RH	24	24
30	16/16RH	16	16
31	KB45/5/24	48	24
32	KB45/5/24	48	24
33	16/08LH	16	8
34	16/08LH	16	8
35	24/24RH	24	24
36	24/24RH	24	24
37	24/12RH	24	12
38	16/16RH	16	16
39	TIP	0	13.6

Screw 18/(KB45/5/08):

Position	Element Name	Pitch [mm]	Axial Length [mm]
1	12/12RH	12	12
2	16/16RH	16	16
3	36/18SK	36	18
4	36/18SK	36	18
5	36/18SK	36	18
6	24/12SK-N	24	12
7	24/24RH	24	24
8	16/16RH	16	16
9	KB45/5/24	48	24
10	KB90/5/16	16	16
11	KB90/5/16	16	16
12	16/08LH	16	8
13	16/08LH	16	8
14	24/24RH	24	24
15	24/24SK	24	24
16	24/24SK	24	24
17	24/12SK-N	24	12
18	16/16RH	16	16
19	24/24RH	24	24
20	24/24RH	24	24
21	24/24RH	24	24
22	24/24RH	24	24
23	24/24RH	24	24
24	24/24RH	24	24
25	24/24RH	24	24
25	24/12RH	24	12
26	KB45/5/08	16	8
27	KB45/5/08	16	8
28	KB45/5/08	16	8
29	KB45/5/08	16	8
30	KB45/5/08	16	8
31	KB45/5/08	16	8
32	KB45/5/08	16	8
33	KB45/5/08	16	8
34	KB45/5/08	16	8
35	KB45/5/08	16	8
36	KB45/5/08	16	8
37	KB45/5/08	16	8
38	KB45/5/08	16	8
39	KB45/5/08	16	8
40	KB45/5/08	16	8
41	KB45/5/08	16	8
42	KB45/5/08	16	8
43	KB45/5/08	16	8
44	KB45/5/08	16	8
45	24/24RH	24	24
46	24/24RH	24	24
47	24/24RH	24	24
48	16/16RH	16	16

Screw 18/(16/16RH):

Position	Element Name	Pitch [mm]	Axial Length [mm]
1	12/12RH	12	12
2	16/16RH	16	16
3	36/18SK	36	18
4	36/18SK	36	18
5	36/18SK	36	18
6	24/12SK-N	24	12
7	24/24RH	24	24
8	16/16RH	16	16
9	KB45/5/24	48	24
10	KB90/5/16	16	16
11	KB90/5/16	16	16
12	16/08LH	16	8
13	16/08LH	16	8
14	24/24RH	24	24
15	24/24SK	24	24
16	24/24SK	24	24
17	24/12SK-N	24	12
18	16/16RH	16	16
19	24/24RH	24	24
20	24/24RH	24	24
21	24/24RH	24	24
22	24/24RH	24	24
23	24/24RH	24	24
24	24/24RH	24	24
25	24/24RH	24	24
25	24/12RH	24	12
26	16/16RH	16	16
27	16/16RH	16	16
28	16/16RH	16	16
29	16/16RH	16	16
30	16/16RH	16	16
31	16/16RH	16	16
32	16/16RH	16	16
33	16/16RH	16	16
34	16/16RH	16	16
35	16/16RH	16	16
36	16/08RH	16	8
37	24/24RH	24	24
38	24/24RH	24	24
39	24/24RH	24	24
40	TIP	0	13.6

Screw 18/(12/12RH):

Position	Element Name	Pitch [mm]	Axial Length [mm]
1	12/12RH	12	12
2	16/16RH	16	16
3	36/18SK	36	18
4	36/18SK	36	18
5	36/18SK	36	18
6	24/12SK-N	24	12
7	24/24RH	24	24
8	16/16RH	16	16
9	KB45/5/24	48	24
10	KB90/5/16	16	16
11	KB90/5/16	16	16
12	16/08LH	16	8
13	16/08LH	16	8
14	24/24RH	24	24
15	24/24SK	24	24
16	24/24SK	24	24
17	24/12SK-N	24	12
18	16/16RH	16	16
19	24/24RH	24	24
20	24/24RH	24	24
21	24/24RH	24	24
22	24/24RH	24	24
23	24/24RH	24	24
24	24/24RH	24	24
25	24/24RH	24	24
25	24/12RH	24	12
26	12/12RH	12	12
27	12/12RH	12	12
28	12/12RH	12	12
29	12/12RH	12	12
30	12/12RH	12	12
31	12/12RH	12	12
32	12/12RH	12	12
33	12/12RH	12	12
34	12/12RH	12	12
35	12/12RH	12	12
36	12/12RH	12	12
37	12/12RH	12	12
38	12/12RH	12	12
39	16/08RH	16	8
40	24/24RH	24	24
41	24/24RH	24	24
42	16/16RH	24	24
43	TIP	0	13.6

Screw 18/Wide/12:

Position	Element Name	Pitch [mm]	Axial Length [mm]
1	12/12RH	12	12
2	16/16RH	16	16
3	36/18SK	36	18
4	36/18SK	36	18
5	36/18SK	36	18
6	24/12SK-N	24	12
7	24/24RH	24	24
8	16/16RH	16	16
9	KB45/5/24	48	24
10	KB90/5/16	16	16
11	KB90/5/16	16	16
12	16/08LH	16	8
13	16/08LH	16	8
14	24/24RH	24	24
15	24/24SK	24	24
16	24/24SK	24	24
17	24/12SK-N	24	12
18	16/16RH	16	16
19	24/24RH	24	24
20	24/24RH	24	24
21	24/24RH	24	24
22	24/24RH	24	24
23	24/24RH	24	24
24	24/24RH	24	24
25	24/24RH	24	24
25	24/24SK	24	24
26	24/24SK	24	24
27	12/12RH	12	12
28	12/12RH	12	12
29	12/12RH	12	12
30	12/12RH	12	12
31	12/12RH	12	12
32	KB45/5/24	24	24
33	KB45/5/24	24	24
34	16/08LH	16	8
35	16/08LH	16	8
36	24/24RH	24	24
37	24/24RH	24	24
38	16/16RH	16	16
39	12/12RH	12	12
40	TIP	0	13.6

Screw 18/Wide/16 (2):

Position	Element Name	Pitch [mm]	Axial Length [mm]
1	12/12RH	12	12
2	16/16RH	16	16
3	36/18SK	36	18
4	36/18SK	36	18
5	36/18SK	36	18
6	24/12SK-N	24	12
7	24/24RH	24	24
8	16/16RH	16	16
9	KB45/5/24	48	24
10	KB90/5/16	16	16
11	KB90/5/16	16	16
12	16/08LH	16	8
13	16/08LH	16	8
14	24/24RH	24	24
15	24/24SK	24	24
16	24/24SK	24	24
17	24/12SK-N	24	12
18	16/16RH	16	16
19	24/24RH	24	24
20	24/24RH	24	24
21	24/24RH	24	24
22	24/24RH	24	24
23	24/24RH	24	24
24	24/24RH	24	24
25	24/24RH	24	24
25	24/24SK	24	24
26	24/24SK	24	24
27	24/12SK-N	24	12
28	16/16RH	16	16
29	16/16RH	16	16
30	16/16RH	16	16
31	KB45/5/24	24	24
32	KB45/5/24	24	24
33	16/08LH	16	8
34	16/08LH	16	8
35	24/24RH	24	24
36	24/24RH	24	24
37	16/16RH	16	16
38	12/12RH	12	12
39	TIP	0	13.6

26-mm Screw Geometry Details:

Screw 26/Narrow/24:

Position	Element Name	Pitch [mm]	Axial Length [mm]
1	16/16RH	16	16
2	48/24SK	48	24
3	48/24SK	48	24
4	48/24SK	48	24
5	48/24SK	48	24
6	36/18SK-N	36	18
7	36/36RH	36	36
8	24/24RH	24	24
9	KB45/5/36	72	36
10	KB90/5/24	24	24
11	KB90/5/24	24	24
12	24/12LH	24	12
13	24/12LH	24	12
14	24/24RH	24	24
15	24/24RH	24	24
16	36/36RH	36	36
17	36/36RH	36	36
18	36/36RH	36	36
19	36/36RH	36	36
20	36/36RH	36	36
21	36/36RH	36	36
22	36/36RH	36	36
23	36/36SK	36	36
24	36/36SK	36	36
25	36/18SK-N	36	18
26	36/36RH	36	36
27	24/24RH	24	24
28	KB45/5/12	24	12
29	KB45/5/12	24	12
30	KB45/5/12	24	12
31	KB45/5/12	24	12
32	KB45/5/12	24	12
33	KB45/5/12	24	12
34	24/12LH	24	12
35	24/12LH	24	12
36	36/18	36	36
37	36/18	36	18
38	24/24	24	24

Screw 26/Wide/24:

Position	Element Name	Pitch [mm]	Axial Length [mm]
1	16/16RH	16	16
2	48/24SK	48	24
3	48/24SK	48	24
4	48/24SK	48	24
5	48/24SK	48	24
6	36/18SK-N	36	18
7	36/36RH	36	36
8	24/24RH	24	24
9	KB45/5/36	72	36
10	KB90/5/24	24	24
11	KB90/5/24	24	24
12	24/12LH	24	12
13	24/12LH	24	12
14	24/24RH	24	24
15	24/24RH	24	24
16	36/36RH	36	36
17	36/36RH	36	36
18	36/36RH	36	36
19	36/36RH	36	36
20	36/36RH	36	36
21	36/36RH	36	36
22	36/36RH	36	36
23	36/36SK	36	36
24	36/36SK	36	36
25	36/18SK-N	36	18
26	36/36RH	36	36
27	24/24RH	24	24
28	KB45/5/36	72	36
28	KB45/5/36	72	36
30	24/12LH	24	12
31	24/12LH	24	12
32	36/36RH	36	36
33	36/18RH	36	36
34	36/18RH	36	18
35	24/24RH	24	24

Screw 26/(KB45/5/12):

Position	Element Name	Pitch [mm]	Axial Length [mm]
1	16/16RH	16	16
2	48/24SK	48	24
3	48/24SK	48	24
4	48/24SK	48	24
5	48/24SK	48	24
6	36/18SK-N	36	18
7	36/36RH	36	36
8	24/24RH	24	24
9	KB45/5/36	72	36
10	KB90/5/24	24	24
11	KB90/5/24	24	24
12	24/12LH	24	12
13	24/12LH	24	12
14	24/24RH	24	24
15	24/24RH	24	24
16	36/36RH	36	36
17	36/36RH	36	36
18	36/36RH	36	36
19	36/36RH	36	36
20	36/36RH	36	36
21	36/36RH	36	36
22	36/36RH	36	36
23	36/36SK	36	36
24	36/36SK	36	36
25	36/18SK-N	36	18
26	36/36RH	36	36
27	36/18RH	36	18
28	KB45/5/12	24	12
29	KB45/5/12	24	12
30	KB45/5/12	24	12
31	KB45/5/12	24	12
32	KB45/5/12	24	12
33	KB45/5/12	24	12
34	KB45/5/12	24	12
35	KB45/5/12	24	12
36	KB45/5/12	24	12
37	36/36RH	36	36
38	36/18RH	36	18
39	24/12RH	24	12
40	Spacer/1		
41	24/24RH	24	24

Screw 26/(16/16RH):

Position	Element Name	Pitch [mm]	Axial Length [mm]
1	16/16RH	16	16
2	48/24SK	48	24
3	48/24SK	48	24
4	48/24SK	48	24
5	48/24SK	48	24
6	36/18SK-N	36	18
7	36/36RH	36	36
8	24/24RH	24	24
9	KB45/5/36	72	36
10	KB90/5/24	24	24
11	KB90/5/24	24	24
12	24/12LH	24	12
13	24/12LH	24	12
14	24/24RH	24	24
15	24/24RH	24	24
16	36/36RH	36	36
17	36/36RH	36	36
18	36/36RH	36	36
19	36/36RH	36	36
20	36/36RH	36	36
21	36/36RH	36	36
22	36/36RH	36	36
23	36/36SK	36	36
24	36/36SK	36	36
25	36/36RH	36	36
26	24/24RH	24	24
27	16/16RH	16	16
28	16/16RH	16	16
29	16/16RH	16	16
30	16/16RH	16	16
31	16/16RH	16	16
32	16/16RH	16	16
33	36/36RH	36	36
34	36/18RH	36	18
35	36/18RH	36	18
36	24/24RH	24	24

Screw 26/Wide/16:

Position	Element Name	Pitch [mm]	Axial Length [mm]
1	16/16RH	16	16
2	48/24SK	48	24
3	48/24SK	48	24
4	48/24SK	48	24
5	48/24SK	48	24
6	36/18SK-N	36	18
7	36/36RH	36	36
8	24/24RH	24	24
9	KB45/5/36	72	36
10	KB90/5/24	24	24
11	KB90/5/24	24	24
12	24/12LH	24	12
13	24/12LH	24	12
14	24/24RH	24	24
15	24/24RH	24	24
16	36/36RH	36	36
17	36/36RH	36	36
18	36/36RH	36	36
19	36/36RH	36	36
20	36/36RH	36	36
21	36/36RH	36	36
22	36/36RH	36	36
23	36/36SK	36	36
24	36/36SK	36	36
25	36/18SK-N	36	18
26	16/16	16	16
27	16/16	16	16
28	16/16	16	16
29	16/16	16	16
30	16/16	16	16
31	KB45/5/36	72	36
32	KB45/5/36	72	36
33	24/12LH	24	12
34	24/12LH	24	12
35	36/36	36	36
36	36/18	36	18
37	24/24	24	24

Screw 26/Wide/24 (2):

Position	Element Name	Pitch [mm]	Axial Length [mm]
1	16/16RH	16	16
2	48/24SK	48	24
3	48/24SK	48	24
4	48/24SK	48	24
5	48/24SK	48	24
6	36/18SK-N	36	18
7	36/36RH	36	36
8	24/24RH	24	24
9	KB45/5/36	72	36
10	KB90/5/24	24	24
11	KB90/5/24	24	24
12	24/12LH	24	12
13	24/12LH	24	12
14	24/24RH	24	24
15	24/24RH	24	24
16	36/36RH	36	36
17	36/36RH	36	36
18	36/36RH	36	36
19	36/36RH	36	36
20	36/36RH	36	36
21	36/36RH	36	36
22	36/36RH	36	36
23	36/36SK	36	36
24	36/36SK	36	36
25	36/18SK-N	36	18
26	24/24	24	24
27	24/24	24	24
28	24/24	24	24
29	24/12	24	12
30	KB45/5/36	72	36
31	KB45/5/36	72	36
32	24/12LH	24	12
33	24/12LH	24	12
34	Spacer/1	-	1
35	Spacer/1	-	1
36	36/36	36	36
37	24/12	24	12
38	24/24	24	24

Appendix B

In House Analysis MATLAB Code:

```
function [CamesArea,Time_orig,RTD_orig,Time_final,RTD_final,BlV] =
camesanalysis2(filename,startcell,ST1,ST2,tail_time,BlCT)
%Joseph Martin, Jason Nixon, and Graeme Fukuda
% Function Inputs:
%       1) file name
%       2) start index                      norm = 264 or 400
%       3) tail time 1                      norm = 5
%       4) tail time 2                      norm = 25
%       5) tail length (seconds)            norm = 200
%       6) baseline cut time                user selected           BlCT
% camesanalysis('7_140_ink1.xlsx',264,5,25,200,120)
% Notes:
    %tail time 2 > tail time 1
    %ST2 needs to be the greater than ST1:  these control the time before
    %the minmum that you are sampling for your slope estimate for the tail
    %in natural log space
    %tail time:  length of time the tail goes for (not the time that it
    %stops, but the time from the beggining of the tail to the end of the
    %tail
%% Inputting Data
    xTime = xlsread(filename,'A:A');
    L = length(xTime)+ 23;
    Voltage = xlsread(filename,num2str(L,'B24:B%d'));
%% Low-Pass filter for data
    fs = 44100; % Sampling frequency [Hz]
    order = 2;  % Order of filter.
    fc = 200;   % Cut-off frequency [Hz]
    [num den] = butter(order, fc/(fs/2)); %Butterworth Filter
    VoltageInterp = filter(num, den, Voltage); %Filtered Data
%% Scaling/ Curve Creation
    %Scale Unfiltered data for plotting
        startcell = startcell-23; %Account for beginning cells.
    %Scale filtered data for plotting
        xTime2_1 = xTime(startcell:end);
        VoltageInterp = VoltageInterp(startcell:end);
    %RTD Curve
        maxV = max(VoltageInterp);
        RTD_V_1 = -1*(VoltageInterp - maxV);
    %stores orgienal values before edits
        RTD_V_orig=RTD_V_1;
        xTime2_orig=xTime2_1;
%% Truncates baseline data
    % calculates the index associated with the baseline cut time
        indx1=BlCT*1200+1;
    %defines the baseline y value
        BlV=RTD_V_1(indx1)-0.01;
    % truncates data before the baseline cut time
        RTD_V_1(1:indx1)=BlV;
%% Extrapolating tail
    % inital cutoff point (truncates any final curls in the data
        cutoff_node=15*1200;
    % stores new data array without the last 15 seconds worth of data
        x_data = xTime2_1(end-cutoff_node+1:end);
        y_data = RTD_V_1(end-cutoff_node+1:end);
    % looks for the minimum voltage in the last X seconds
        val1=interp1(y_data,x_data,min(min(y_data)));
    % finds the nodal value of the minimum voltage in the last X seconds
   val2=interp1(xTime2_1,linspace(1,size(xTime2_1,1),size(xTime2_1,1)),val1);
    % cuts off the time & voltage after the time minimum point
        xTime2_2=xTime2_1(1:val2);

        for j=1:numel(RTD_V_1)
```

```
            if RTD_V_1(j)<BlV
                RTD_V_1(j)=BlV;
            end
        end

        RTD_V_2_log=log(RTD_V_1(1:val2)-BlV+0.000000001);
    % number of nodes of the voltage matrix
        end_P=size(RTD_V_2_log,1);
    % half of the range of the averaging for the slope calcuation
        CS=1;
    % mean of the first slope area of interest
        point1=mean(RTD_V_2_log(end_P-(ST1+CS)*1200:end_P-(ST1-CS)*1200));
    % mean of the second slope area of interest
        point2=mean(RTD_V_2_log(end_P-(ST2+CS)*1200:end_P-(ST2-CS)*1200));
    % time at which the original data is cut and the tail is attached
        tail_t2=xTime2_2(end-ST2*1200);
    % calcuates slope (in LOG)
        m=(point1-point2)/(-ST1+ST2);
    % calcuates the Y intercept of the tail (in LOG)
        b=RTD_V_2_log(end-ST2*1200)-m*tail_t2;

    % stores the cut off set of time
        xTime2_3=xTime2_2(1:end-ST2*1200);
    % truncates the tail data
        RTD_V_3=RTD_V_2_log(1:end-ST2*1200);
    % generates time values for tail nodes
xTime2_tail=linspace(xTime2_3(end)+1,xTime2_3(end)+tail_time+1,tail_time+1);

        RTD_V_tail=m*xTime2_tail+b;

        RTD_V=exp([ RTD_V_3 ; RTD_V_tail' ])+BlV;

        xTime2=[ xTime2_3 ; xTime2_tail' ];

%% Calculating Area Under Curve
    % calculates area using trapezoidal rule (the BlS subtractor is there
    % to adjust for the baseline
        CamesArea1 = trapz(xTime2,RTD_V-BlV);
        CamesArea = CamesArea1;
    % stores origenal data set for export
        RTD_orig=RTD_V_orig;
        Time_orig=xTime2_orig-xTime2_orig(1);
    % stores modified data set for export
        Time_final(1:length(xTime2)) = xTime2-xTime2(1);
        RTD_final(1:length(RTD_V)) = RTD_V;

end
```

MATLAB Code for Published Results:

The following code presented is for an example operating condition of 20.5 lb/hr and 240 RPM. The condition was performed on the 26-mm CoTSE, but the extruder size does not affect the code.

```
clc;
clear;
close all

% [I1,T1_orig,V1_orig,T1,V1,B1V1]=
camesanalysis2('20.5_240_ink1.xlsx',264,10,15,100,20);
% disp(['Ink 1 = ',num2str(I1)])

[I2,T2_orig,V2_orig,T2,V2,B2V2]=
camesanalysis2('20.5_240_ink2.xlsx',264,8,10,100,26.13);
```

```
disp(['Ink 2 = ',num2str(I2)])


% [C1,T5_orig,V5_orig,T5,V5,B5V5]=
camesanalysis2('20.5_240_cames1.xlsx',264,12,15,100,26.75);
% disp(['Cames 1 = ',num2str(C1)])

[C2,T6_orig,V6_orig,T6,V6,B6V6]=
camesanalysis2('20.5_240_cames2.xlsx',264,17,20,100,23.4);
disp(['Cames 2 = ',num2str(C2)])

[C3,T7_orig,V7_orig,T7,V7,B7V7]=camesanalysis2('20.5_240_cames3.xlsx',264,24,26,100,29
.85);
disp(['Cames 3 = ',num2str(C3)])

%
[C4,T8_orig,V8_orig,T8,V8,B8V8]=camesanalysis2('20.5_240_cames4.xlsx',264,30,35,100,26
.3);
% disp(['Cames 4 = ',num2str(C4)])

ink1_shift= 0;
ink2_shift= 0;
cames1_shift= 0;
cames2_shift= 11;
cames3_shift= 4;
cames4_shift= 0;

disp('  ')
% disp(['PercentBreakup11 = ',num2str(C1/I1)])
% disp(['PercentBreakup12 = ',num2str(C2/I1)])
% disp(['PercentBreakup13 = ',num2str(C3/I1)])
% % disp(['PercentBreakup14 = ',num2str(C4/I1)])

% disp(['PercentBreakup12 = ',num2str(C1/I2)])
disp(['PercentBreakup22 = ',num2str(C2/I2)])
disp(['PercentBreakup32 = ',num2str(C3/I2)])
% disp(['PercentBreakup42 = ',num2str(C4/I2)])

h=figure(1);
hold on
% plot(T1+ink1_shift,V1-B1V1,'b')
plot(T2+ink2_shift,V2-B2V2,'b')
% plot(T5+cames1_shift,V5-B5V5,'g')
plot(T6+cames2_shift,V6-B6V6,'g')
plot(T7+cames3_shift,V7-B7V7,'m')
% plot(T8+cames4_shift,V8-B8V8,'m')


key = legend('Ink 1','Cames 1 = 52%','Cames 2 = 53%');
hold off
filename='ewide';
print(h,'-djpeg','-r300',filename)
figure(2)
% subplot(3,3,1); plot(T1_orig,V1_orig,'r'); hold on; plot(T1,V1); hold off
% title('Ink 1')
subplot(3,3,2); plot(T2_orig,V2_orig,'r'); hold on; plot(T2,V2); hold off
title('Ink 2')
% subplot(3,3,5); plot(T5_orig,V5_orig,'r'); hold on; plot(T5,V5); hold off
% title('Cames 1')
subplot(3,3,6); plot(T6_orig,V6_orig,'r'); hold on; plot(T6,V6); hold off
title('Cames 2')
subplot(3,3,7); plot(T7_orig,V7_orig,'r'); hold on; plot(T7,V7); hold off
title('Cames 3')
% subplot(3,3,8); plot(T8_orig,V8_orig,'r'); hold on; plot(T8,V8); hold off
% title('Cames 4')
```

Appendix C

Effect of Bead Strength Percent Drag Flow

All percent drag flow values are for the operating conditions used for the Effect of Bead Strength Study on the 28-mm CoTSE.

Operating Condition ***(Q)/(N)*** **[lb/hr]/[RPM]**	**Percent Drag Flow [%] in 28-mm Narrow Kneading Block**	**Percent Drag Flow [%] in 28-mm Wide Kneading Block**
1.95/40	36.3	10.4
2.4/75	23.8	6.8
4.8/75	47.7	13.6
1.8/110	12.2	3.4
5.3/110	35.9	10.3
8.8/110	59.6	17.0
4.6/145	23.6	6.8
9.3/145	47.8	13.6
8.7/180	36.0	10.3

Robust Design of Experiment Approach Percent Drag Flow

All percent drag flow values are for the operating conditions used for the Robust Design of Experiment Approach Study on 18-mm CoTSE.

Operating Condition ***(Q)/(N)*** **[lb/hr]/[RPM]**	**Percent Drag Flow [%] in 18-mm Narrow Kneading Block**	**Percent Drag Flow [%] in 18-mm Wide Kneading Block**
5/100	54.4	20.9
5.75/115	54.4	20.9
7/140	54.4	20.9
8/190	45.8	17.6
10/190	52.7	22.0
6/240	27.2	10.5
7/240	31.7	12.2
8/240	36.3	14.0
12/240	54.4	20.9
15/240	68.0	26.2
16/240	72.5	27.9
16.5/240	74.8	28.8
12/290	45.0	17.3
15/290	56.3	21.6
17/340	54.4	20.9
15/365	44.7	17.2
18/365	53.6	20.6
19/365	56.6	21.8
14/390	39.1	15.0
19/390	53.0	20.4
23/390	64.2	24.7
17/415	44.6	17.1
22/415	57.7	22.2
22/440	54.4	20.9

Appendix D

18-mm Extensional Stress Values

Robust DOE Study, Original CCD Grid:

Operating Condition ***(Q)/(N)*** **[lb/hr]/[RPM]**	**18-mm Narrow Kneading Block [kPa]**	**18-mm Wide Kneading Block [kPa]**
7/140	94.1	129.3
8/190	111.7	165.8
10/190	127.5	171.1
8/240	120.2	197.0
12/240	150.8	207.2
15/240	173.8	214.9
12/290	158.7	237.4
15/290	181.1	244.9
17/340	202.5	278.2

Robust DOE Study, Increased Screw Speed CCD Grid
(and Scale-Up Phase 1, 18-mm Base CCD Grid):

Operating Condition ***(Q)/(N)*** **[lb/hr]/[RPM]**	**18-mm Narrow Kneading Block [kPa]**	**18-mm Wide Kneading Block [kPa]**
17/340	129.9	254.0
15/365	141.0	270.2
19/365	155.4	275.0
14/390	144.8	283.5
19/390	173.0	292.9
23/390	194.2	300.0
17/415	176.2	305.6
22/415	197.2	312.6
22/440	213.7	329.3

Robust DOE Study, Expanded Cross CCD Grid:

Operating Condition ***(Q)/(N)*** **[lb/hr]/[RPM]**	**18-mm Narrow Kneading Block [kPa]**	**18-mm Wide Kneading Block [kPa]**
5/100	68.9	94.6
5.75/115	78.5	107.9
6/240	104.8	191.9
7/240	112.5	194.5
16/240	181.5	217.4
16.5/240	185.3	218.7
18/365	212.7	294.1
19/390	222.5	309.4

Scale-Up Phase 2, 18-mm Base CCD Grid:

Operating Condition ***(Q)/(N)*** **[lb/hr]/[RPM]**	**18-mm Narrow Kneading Block [kPa]**	**18-mm Wide Kneading Block [kPa]**
4.5/140	73.6	122.5
4.5/190	83.8	156.5
7/190	103.7	163.1
4.5/240	93.3	188.1
7/240	112.5	194.4
10/240	135.5	202.1
7/290	121.4	225.0
10.5/290	147.5	233.7
10.5/340	155.3	262.5

26-mm Extensional Stress Values

Scale-Up Phase 1, Volumetric CCD Grid:

Operating Condition ***(Q)/(N)*** **[lb/hr]/[RPM]**	**26-mm Narrow Kneading Block [kPa]**	**26-mm Wide Kneading Block [kPa]**
47/340	327.8	564.6
43/365	322.5	589.58
53/365	355.5	600.6
36/390	307.5	610.4
54/390	366.0	629.9
68/390	411.5	645.1
49/415	356.9	652.0
61/415	395.5	664.9
61/440	401.7	690.9

Scale-Up Phase 1, Percent Drag Flow CCD Grid:

Operating Condition ***(Q)/(N)*** **[lb/hr]/[RPM]**	**26-mm Narrow Kneading Block [kPa]**	**26-mm Wide Kneading Block [kPa]**
37/340	294.4	553.5
34/365	292.9	579.7
42/365	319.2	588.5
28/390	281.5	601.7
43/390	330.3	618.0
54/390	366.0	629.9
38/415	321.7	640.3
47/415	350.6	649.9
48/440	360.6	677.2

Scale-Up Phase 2, Volumetric CCD Grid:

Operating Condition ***(Q)/(N)*** **[lb/hr]/[RPM]**	**26-mm Narrow Kneading Block [kPa]**	**26-mm Wide Kneading Block [kPa]**
12/140	124.8	253.5
13/190	151.8	328.6
19.5/190	175.5	336.5
12.5/240	171.2	396.1
20.5/240	199.4	405.5
28/240	225.9	414.4
19.5/290	216.5	471.1
30/290	252.6	483.1
29/340	267.7	544.5

Scale-Up Phase 2, Percent Drag Flow Mixing CCD Grid:

Operating Condition ***(Q)/(N)*** **[lb/hr]/[RPM]**	**26-mm Narrow Kneading Block [kPa]**	**26-mm Wide Kneading Block [kPa]**
13/140	128.6	254.7
14/190	155.4	329.8
21/190	181.0	338.4
14/240	176.5	397.9
22/240	204.7	407.3
30.5/240	234.7	417.3
21/290	221.7	472.8
32/290	259.5	485.4
31/340	274.4	546.8

Scale-Up Phase 2, Percent Drag Flow Narrow-Pitched Conveying Elements:

Operating Condition ***(Q)/(N)*** **[lb/hr]/[RPM]**	**26-mm Narrow Kneading Block [kPa]**	**26-mm Wide Kneading Block [kPa]**
10/140	117.2	251.0
11/190	144.4	326.2
17/190	166.4	333.5
11/240	165.9	394.4
17.5/240	188.9	402.0
24.5/240	213.5	410.2
17/290	208.0	468.2
25.5/290	237.1	477.9
25/340	254.3	540.1

Scale-Up Phase 2, Percent Drag Flow Square-Pitched Conveying Elements:

Operating Condition ***(Q)/(N)*** **[lb/hr]/[RPM]**	**26-mm Narrow Kneading Block [kPa]**	**26-mm Wide Kneading Block [kPa]**
11/140	121.0	252.2
12/190	148.1	327.4
18/190	170.0	334.7
12/240	169.5	395.5
19/240	194.1	403.8
26/240	218.8	412.0
18/290	211.4	469.4
27.5/290	244.0	480.2
27/340	261.0	542.3

Bibliography

[1] L. P. B. M. Janssen, *Twin Screw Extrusion*, 1st ed. Elsevier Science Ltd, 1978.

[2] S. Kalpakjian and S. R. Schmid, *Manufacturing Processes For Engineering Materials*, 5th ed. Pearson Education Inc., 2008.

[3] K. Kohlgrüber and M. Bierdel, *Co-rotating twin-screw extruders: fundamentals, technology, and applications*. Hanser Verlag, 2008.

[4] C. Rauwendaal, *Polymer Extrusion*. Munich Vienna New York: Hanser Publishers, 1986.

[5] D. V. Rosato, *Extruding Plastics: Practical Processing Handbook*. Springer, 1998.

[6] Z. Tadmor and C. G. Gogos, *Principles of Polymer Processing*, 2nd ed. Wiley-Interscience, 2006.

[7] C. Rauwendaal, *Mixing In Polymer Processing*. New York, New York: Marcel Dekker, Inc., 1991.

[8] N. P. Cheremisinoff, *Polymer Mixing and Extrusion Technology*, vol. 16. CRC, 1987.

[9] J. Curry and A. Kiani, "Experimental Identification of the Distribution of Fluid Stresses in Continuous Melt Compounders - Part 2," in *SPE-ANTEC Tech Papers*, 1991, vol. 37, pp. 114–118.

[10] C. Martin, "Twin Screw Extrusion Theory," presented at the 2013 Leistritz Pharmaceutical Extrusion Workshop, New Jersey, 10-Jun-2013.

[11] J. L. White and H. Potente, *Screw Extrusion*. Cinc: Han, 2002.

[12] B. Thiele, "Twin Screw Extrusion Screw Design, Processing, and Scale-Up," presented at the 2013 Leistritz Pharmaceutical Extrusion Workshop, New Jersey, 10-Jun-2013.

[13] L. J. Fuller, "Material Treating Apparatus," US2615199 A.

[14] J. L. White, *Twin Screw Extrusion Technology and Principles*. Cinc: Hans, 1990.

[15] A. Shah and M. Gupta, "Comparison of the Flow in Co-Rotating and Counter-Rotating Twin-Screw Extruders," *Annu. Tech. Conf. Soc. Plast. Eng.*, pp. 443–447, 2004.

[16] I. Manas-Zloczower, *Mixing and compounding of polymers: theory and practice*. Hanser Verlag, 2009.

[17] J. Gao, G. C. Walsh, D. I. Bigio, R. M. Briber, and M. D. Wetzel, "Mean Residence Time Analysis for Twin Screw Extruders," *Polym. Eng. Sci.*, vol. 40, no. 1, pp. 227–237, Jan. 2000.

[18] J. Gao, G. C. Walsh, D. Bigio, R. M. Briber, and M. D. Wetzel, "Residence‐Time Distribution Model for Twin‐Screw Extruders," *AIChE J.*, vol. 45, no. 12, pp. 2541–2549, Dec. 1999.

[19] R. S. Spencer and R. M. Wiley, "The Mixing of Very Viscous Liquids," *J. Colloid Sci.*, vol. 6, no. 2, pp. 133–145, 1951.

[20] A. Brothman, G. N. Wollan, and S. M. Feldman, "New Analysis Provides Formula to Solve Mixing Problems," *Chem. Met. Eng.*, vol. 52, pp. 102–106, 1945.

[21] L. Erwin, “Theory of Laminar Mixing,” *Polym. Eng. Sci.*, vol. 18, no. 13, pp. 1044–1048, 1978.
[22] H. Aref, “Stirring by Chaotic Advection,” *J. Fluid Mech.*, vol. 143, pp. 1–21, 1984.
[23] J. M. Ottino, W. E. Ranz, and C. W. Macosko, “A Framework for Description of Mechanical Mixing of Fluids,” *AlChE J.*, vol. 27, no. 4, pp. 565–577, 1981.
[24] D. I. Bigio, J. D. Boyd, L. Erwin, and D. W. Gailus, “Mixing Studies in the Single Screw Extruder,” *Polym. Eng. Sci.*, vol. 25, no. 5, pp. 305–310, 1985.
[25] P. V. Danckwerts, “The Definition and Measurement of Some Characteristics of Mixtures,” *Appl. Sci. Res. Sect.*, vol. 3, no. 4, pp. 279–296, 1952.
[26] D. I. Bigio and W. Stry, “Measures of Mixing in Laminar Flow,” *Polym. Eng. Sci.*, vol. 30, no. 3, pp. 153–161, 1990.
[27] G. Lidor and Z. Tadmor, “Theoretical Analysis of Residence Time Distribution Functions and Strain Distribution Function in Plasticating Screw Extruders,” *Polym. Eng. Sci.*, vol. 16, no. 6, pp. 450–462, 1976.
[28] B. Luo, Z. Long, and S. Sun, “Study on the Mixing Ability of DIfferent Mixing Elements in Co-Rotating Twin Screw Extruder,” in *ANTEC 2007*, 2007, pp. 380–384.
[29] A. Lawal and D. Kalyon, “Mechanisms of Mixing in Single and Co-Rotating Twin Screw Extruders,” *Polym. Eng. Sci.*, vol. 35, no. 17, pp. 1325–1338, 1995.
[30] A. Lawal and D. M. Kalyon, “Simulation of Intensity of Segregation Distributions Using Three-Dimensional FEM Analysis: Application to Corotating Twin Screw Extrusion Processing,” *J. Appl. Polym. Sci.*, vol. 58, no. 9, pp. 1501–1507, Nov. 1995.
[31] D. M. Kalyon and M. Malik, “An Integrated Approach for Numerical Analysis of Coupled Flow and Heat Transfer in Co-rotating Twin Screw Extruders,” *Int. Polym. Process.*, vol. 22, no. 3, pp. 293–302, 2007.
[32] M. Malik, D. M. Kalyon, and J. Golba, “Simulation of Co-Rotating Twin Screw Extrusion Process Subject to Pressure-Dependent Wall Slip at Barrel and Screw Surfaces: 3D FEM Analysis for Combinations of Forward- and Reverse-Conveying Screw Elements,” *Int. Poly*, vol. 29, no. 1, pp. 51–62, 2014.
[33] P. A. Hartley and G. D. Parfitt, “Dispersion of Powders in Liquids. 1. The Contribution of the Van Der Waals Force to the Cohesiveness of Carbon Black Powders,” *Langmuir*, vol. 1, pp. 651–657, 1985.
[34] J. M. Ottino and P. DeRousell, “Mixing and Dispersion of Viscous Liquids and Powdered Solids,” *Adv. Chem. Eng.*, vol. 25, pp. 105–204, 2000.
[35] A. Scurati, D. L. Feke, and I. Manas-Zloczower, “Analysis of the Kinetics of Agglomerate Erosion in Simple Shear Flows,” *Chem. Eng. Sci.*, vol. 60, no. 23, pp. 6564–6573, 2005.
[36] F. Bohin, I. Manas‐Zloczower, and D. L. Feke, “Kinetics of Dispersion for Sparse Agglomerates in Simple Shear Flows: Application to Silica Agglomerates in Silicone Polymers,” *Chem. Eng. Sci.*, vol. 51, no. 23, pp. 5193–5204, 1996.
[37] W. Wang, I. Manas-Zloczower, and M. Kaufman, “Characterization of Distributive mixing in Polymer Processing Equipment using Renyi Entropies,” *AlChE J.*, vol. 49, no. 7, pp. 1637–1644, 2003.

[38] L. Cong and M. Gupta, “Simulation of Distributive and Dispersive Mixing in a Co-Rotating Twin-Screw Extruder,” in *ANTEC 2008*, 2008, pp. 300–304.
[39] J. Arrizón, R. E. Salazar, and M. Arellano, “Dispersive Mixing of Surfactant-Modified Titanium Dioxide Agglomerates into High Density Polyethylene,” presented at the Antec, 1998, vol. 3.
[40] S. V. Kao and S. G. Mason, “Dispersion of Particles by Shear,” *Nature*, vol. 253, pp. 577–594.
[41] E. Hammel, X. Tang, M. Trampert, T. Schmitt, K. Mauthner, A. Eder, and P. Potschke, “Carbon Nanofibers for Composite Applications,” *Carbon*, vol. 42, pp. 1153–1158, 2004.
[42] C. Guthy, F. Du, S. Brand, K. I. Winey, and J. E. Fischer, “Thermal Conductivity of Single-Walled Carbon Nanotube/PMMA Nanocomposites,” *J. Heat Transf.*, vol. 129, no. 8, pp. 1096–1099, 2007.
[43] J. Sandler, P. Werner, M. S. P. Shaffer, V. Demchuk, V. Altstadt, and A. H. Windle, “Carbon-Nanofibre-Reinforced Poly(ether ether ketone) Composites,” *Compos. Part Appl. Sci. Manuf.*, vol. 33, no. 8, pp. 1033–1039, 2002.
[44] C. D. Denson and B. K. Hwang Jr., “The influence of the axial pressure gradient on flow rate for Newtonian liquids in a self wiping, co‐rotating twin screw extruder,” *Polym. Eng. Sci.*, vol. 20, no. 14, pp. 965–971, Sep. 1980.
[45] G. E. Gasner, D. Bigio, C. Marks, F. Magnus, and C. Kiehl, “A New Approach to Analyzing Residence Time and Mixing in a Co‐Rotating Twin Screw Extruder,” *Polym. Eng. Sci.*, vol. 39, no. 2, pp. 286–298, Feb. 1999.
[46] J. Cheng, Y. Xie, and D. Bigio, “Characterization of Kneading Block Performance in Co-Rotating Twin Screw Extruders,” in *SPE-ANTEC Tech. Papers*, 1998, pp. 198–202.
[47] T. Brouwer, D. B. Todd, and L. P. B. M. Janssen, “Flow Patterns in Special Twin Screw Mixing Elements,” *ANTEC 1999*, 1999.
[48] O. Wunsch, R. Kuhn, and P. Heidermeyer, “Simulation of the Fluid Flow of Deeper Screw Flights for Co-Rotating Twin Screw Extruders,” *ANTEC 2003*, 2003.
[49] A. Kiani, J. Curry, and P. G. Andersen, “Flow Analysis of Twin Screw Extruders Pressure and Drag Capability of Various Twin Screw Elements,” *ANTEC 1998*, pp. 48–54, 1998.
[50] D. Bigg and S. Middleman, “Mixing in a Screw Extruder. A Model for Residence Time Distribution and Strain,” *Ind Eng Chem Fund*, vol. 13, no. 1, pp. 66–71, 1974.
[51] D. M. Bigg, “On Mixing in Polymer Flow Systems,” *Polym. Eng. Sci.*, vol. 15, no. 9, pp. 684–689, 1975.
[52] A. Kumar, G. M. Ganjyal, D. D. Jones, and M. A. Hanna, “Digital image processing for measurement of residence time distribution in a laboratory extruder,” *J. Food Eng.*, vol. 75, no. 2, pp. 237–244, 2006.
[53] G. Shearer and C. Tzoganakis, “Distributive mixing profiles for co‐rotating twin‐screw extruders,” *Adv. Polym. Technol.*, vol. 20, no. 3, pp. 169–190, Sep. 2001.
[54] Z. Sun, C. ‐K Jen, C. ‐K Shih, and D. A. Denelsbeck, “Application of ultrasound in the determination of fundamental extrusion performance: Residence

time distribution measurement," *Polym. Eng. Sci.*, vol. 43, no. 1, pp. 102–111, Jan. 2003.
[55] T. Chen, W. I. Patterson, and J. M. Dealy, "On-Line Measurement Residence Time Distribution in a Twin-Screw Extruder," *Int. Polym. Process.*, vol. 10, no. 1, pp. 3–9, 1995.
[56] J. . Puaux, G. Bozga, and A. Ainser, "Residence time distribution in a corotating twin-screw extruder," *Chem. Eng. Sci.*, vol. 55, no. 9, pp. 1641–1651, May 2000.
[57] D. B. Todd, "Residence Time Distribution in Twin‐Screw Extruders," *Polym. Eng. Sci.*, vol. 15, no. 6, pp. 437–443, 1975.
[58] G. Pinto and Z. Tadmor, "Mixing and residence time distribution in melt screw extruders," *Polym. Eng. Sci.*, vol. 10, no. 5, pp. 279–288, Sep. 1970.
[59] G. Shearer and C. Tzoganakis, "MIXING PERFORMANCE OF TWIN SCREW EXTRUDERS DURING MELT-MELT BLENDING," *Polym. Eng. Sci.*, vol. 39, no. 9, pp. 1584–1597, 1999.
[60] G. Shearer and C. Tzoganakis, "The effects of kneading block design and operating conditions on distributive mixing in twin screw extruders," *Polym. Eng. Sci.*, vol. 40, no. 5, pp. 1095–1106, May 2000.
[61] S. V. Kao and G. R. Allison, "Residence Time Distribution in a Twin-Screw Extruder," *Polym. Eng. Sci.*, vol. 24, no. 9, pp. 645–651, Jun. 1984.
[62] P. J. Kim and J. L. White, "Flow Visualization and Residence Time Distributions in a Modular Co-Rotating Twin Screw Extruder," *Int. Polym. Process.*, vol. 9, no. 2, pp. 108–118, 1994.
[63] A. Kiani and P. Heidermeyer, "Study of Flow and RTD in a ZSK Twin Screw Extruder," *ANTEC 1997*, vol. 1, pp. 94–99, Apr. 1997.
[64] L. Chen, Z. Pan, and G. Hu, "Residence Time Distribution in Screw Extruder," *AIChE J.*, vol. 39, no. 9, pp. 1455–1464, Sep. 1993.
[65] J. Gao, D. Bigio, R. M. Briber, and M. D. Wetzel, "Residence Distribution Models for Twin Screw Extruder," *ANTEC 2000*, 2000.
[66] J. Curry and A. Kiani, "Measurement of Stress Level in Continuous Melt Compounders," in *SPE-ANTEC Tech. Papers*, 1990, vol. 36, pp. 1599–1602.
[67] D. Bigio, W. Pappas, H. Brown II, B. Debebe, and W. Dunham, "Residence Stress Distributions in Twin Screw Extruders," in *SPE ANTEC Proceedings*, 2011.
[68] W. L. Pappas, H. Brown II, G. Fukuda, R. Adnew, and D. Bigio, "Variable Strength Stress Bead Analysis in a Twin Screw Extruder," presented at the SPE ANTEC, 2012.
[69] J. F. Carley and J. M. McKelvey, "Extruder Scale-up Theory and Experiments," *Ind. Eng. Chem.*, vol. 45, pp. 989–992, 1953.
[70] A. Gaspar-Cunha and J. A. Covas, "A scaling-up methodology for co-rotating twin-screw extruder," *Polym. Process. Soc.*, May 2011.
[71] J. A. Colbert, "The Inter-Related Aspects of Scaling Up a Complete Tube Extrusion Line," *ANTEC 1998*, pp. 242–246, 1998.
[72] L. Zhu and K. S. Hyun, "Scale-Up Consideration for Polymerization in a Twin-Screw Extruder Using 3-D Numerical Simulation," *ANTEC 2004*, 2004.
[73] "Material Safety Data Sheet: HDPE H6018." Lyondellbasell, 11-Jul-2010.

[74] C. J. Meyers, “Stress Spheres Characterization,” Micron Inc. Analytical Services, Wilmington, DE, #41234, Nov. 2013.
[75] “Material Safety Data Sheet.” DuPont Titanium Technologies, 30-Mar-2009.
[76] W. L. Pappas, “Characterization And Comparison Of Stress History In Various Sized Twin-Screw Extruders Using Residence-Stress Distributions,” Masters, University of Maryland, College Park, 2011.
[77] J. Cheng and D. I. Bigio, “Internal Report.”
[78] C. Polacco, “Coperion Corporation Department of Process Technology,” Coperion Corporation, Test No.: 11-8024, Jun. 2011.
[79] D. Bigio, R. Briber, J. Cheng, and Y. Xie, “Model Development to Caclulate the Critical Stress for CAMES.” 1996.